Reduction of Ultrafine Particle Emissions in Wood Fired Cook-stove by using a Turbulent Agglomerator

Ivan Ban

Master of Science Thesis

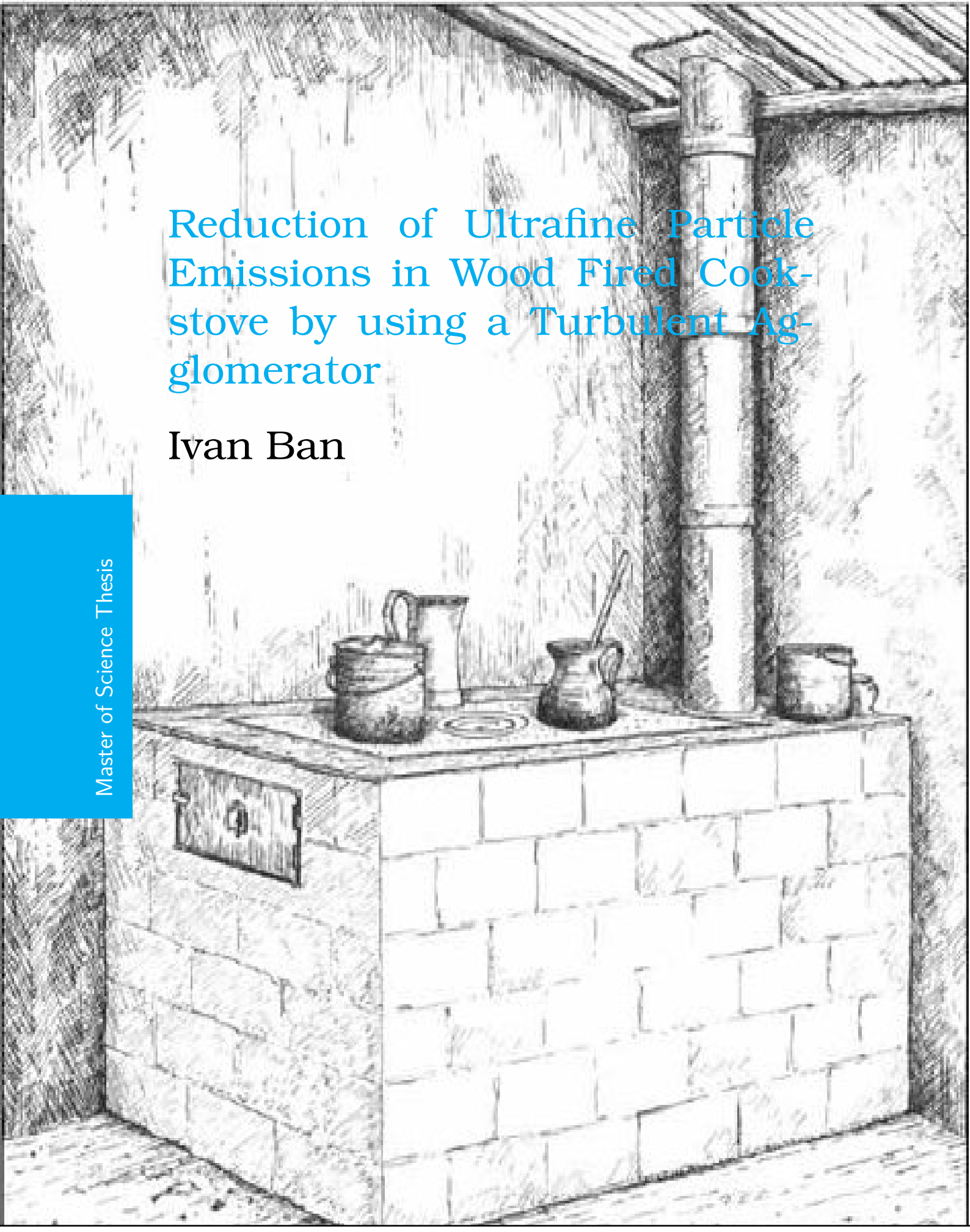

TU Delft Delft University of Technology

Process and Energy Department

Reduction of Ultrafine Particle Emissions in Wood Fired Cookstove by using a Turbulent Agglomerator

by

Ivan Ban

to obtain the degree of
Master of Science in Mechanical Engineering
at the Delft University of Technology,
to be defended publicly on Thursday November 30, 2021 at 12:30 AM

Student Number:	5162181	
Thesis Committee:	Prof.Dr. Dirk Roekaerts	TU Delft, Supervisor
	Dr. ir. Wim-Paul Breugem (chairman)	TU Delft
	Dr. Lorenzo Botto	TU Delft
	Ir. Diego Quan Reyes (TU Eindhoven)	TU Delft

Faculty of Mechanical, Maritime and Materials Engineering (3mE) · Delft University of Technology

Abstract

Emission of fine and ultrafine particles from wood fired cook stoves are a major concern worldwide especially in the many countries where biomass cookstove are used on daily basis. Due to their small size these particles can reach deep within the lungs and cause various health issues. The effect of insertion of a turbulent agglomerator in the cookstove chimney on the number of small particles emitted has been investigated. This device consists of a number of properly designed obstacles in the flow increasing the turbulence level and enhancing collisions and agglomeration of particles. The device is suitable because it requires little extra investment and does not require an external energy source.

First an analytical model of the flow through a Plancha type cookstove was made in MATLAB, in order to obtain estimates for the flow properties at the chimney inlet. Next, CFD simulations were performed using Ansys Fluent R3 and the grid generator program CFMesh+ software. Eulerian-Lagrangian (EL) simulations of dispersed multiphase flow were made to determine the particle dynamics within the flow domain. Particle agglomeration was studied using Eulerian-Eulerian (EE) simulations in combination with the population balance equation (PBE) for particle size. Appropriate agglomeration kernels were implemented via user-defined functions. A key feature taken into account is that agglomeration of particles for particles smaller than the Kolmogorov scale is determined by Brownian motion whereas turbulence takes over as driver for agglomeration for particles larger than the Kolmogorov scale. The turbulence properties were obtained using the standard k-ϵ model with standard wall functions.

To check the operation of the CFD model, a first application of the EE approach was made to a turbulent agglomerator with extra air injection via a jet in the side wall. This was studied in a simplified 2D geometry. In the investigated case it was observed that the turbulence caused by the jet has larger effect than the turbulence of the obstacles.

Next, the EL and EE CFD models were applied to a agglomerator type for which experimental data are available. These simulations concern a 3D domain representing chimney with obstacles creating turbulence. To be relevant for the cookstove chimney case operation at a lower flow rate than the experiment had to be studied. Wakes behind obstacles play an important role. Large particles have higher probability to bypass the wakes. The wakes provide

zones with larger mean residence time where the agglomeration process can have more effect. The simulations using the PBE provided quantitative results for the evolution of the volume fraction of different size classes of particles. It was found that for the considered chimney (lower velocity, hence lower turbulence level) the turbulent agglomeration effect is too weak to obtain a sufficient removal efficiency of submicron particles (under 1%). In case of higher particle load higher removal efficiency can be achieved.

Table of Contents

List of Figures

List of Tables

Acknowledgements

First and foremost, I would like to thank my supervisors prof.dr.Dirk Roekaerts and ir. Diego Quan Reyes for giving me the opportunity to explore this interesting topic. It was a real pleasure working with them, as they have provided a constant support throughout the thesis. Additionally, I would like to thank Dr. ir. Wim-Paul Breugem and Dr. Lorenzo Botto for their time and effort examining this master thesis.

Furthermore, I would like to thank my friends Fulin Yang, Cristopher Moral Ubal and Neel Kumar for their help throughout my studies, and a wonderful time spent at TU Delft. Lastly, special thanks to my parents mr. Andrija Ban and mr. Slavica Ban and my brother mr. Luka Ban, for their love and support.

Delft, University of Technology
November 30, 2021

Ivan Ban

Chapter 1

Introduction

1.1 Motivation

Nowadays, exposure to particulate matter less than 2.5 micrometers in size ($PM_{2.5}$) is the leading environmental and human health problem which causes 4.1 million premature deaths annually worldwide [11]. Furthermore, over half of deaths comes from particles produced from fossil fuel combustion or the industrial, energy and residential sector, and in Figure 1-1 we can see their influence [11]. Moreover, Figure 1-1 - 1-2 represents the map of the $PM_{2.5}$ concentration, where China, India and Africa are the most polluted countries.
However, the focus of these thesis will be lowering particulate emissions in the residential sector, which according to Figure 1-1 has a huge responsibility for such high death rates. In households of both developing and modern countries people use wood fired cookstoves for preparing food, which due to the bad ventilation results in high indoor air pollution of $PM_{2.5}$ [31]. Through trial and error people have succeed in optimizing the cookstove design, which resulted in an increased efficiency and in the reduction of $PM_{2.5}$ emission [34] [31]. Still, particles below the 0.1 μm, which are in the ultrafine range, cannot be reduced due to their small size, which makes them the most dangerous.
Therefore, the primary goal of this thesis is to review the possible solutions proposed in the literature, and to investigate the chance of implementing it into the cookstove design in order to decrease ultrafine particle emissions.

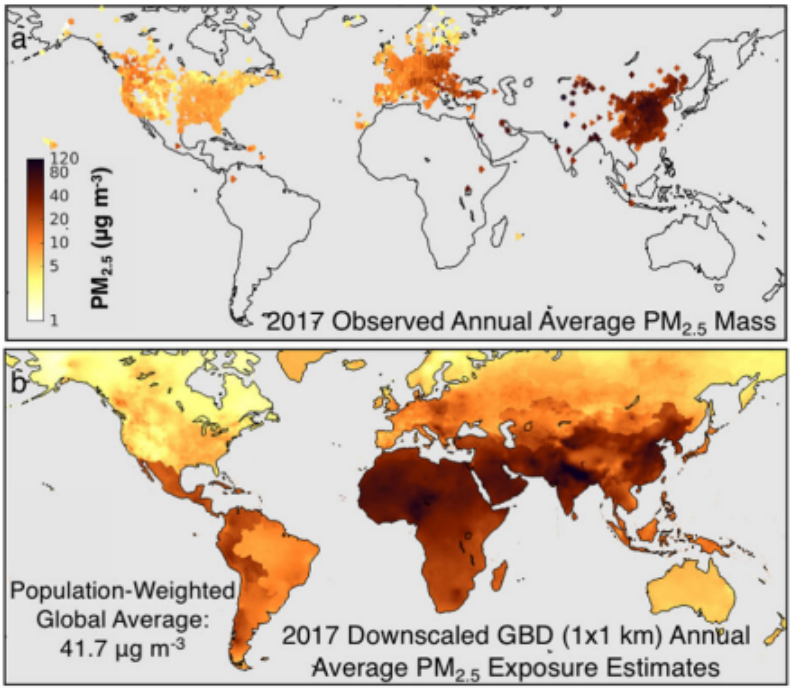

Figure 1-1: Worldwide evaluation of $\mathrm{PM}_{2.5}$ exposure, expressed in $\mu_{\mathrm{g}}\ \mathrm{m}^{-3}$ [11].

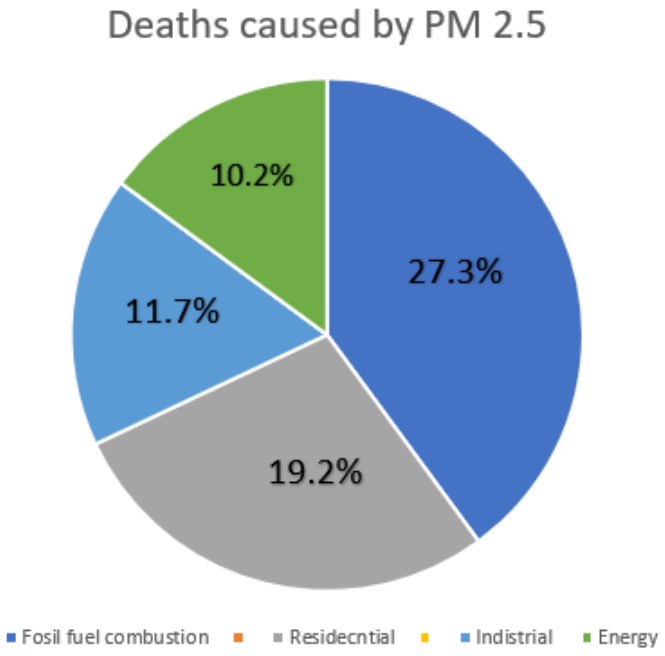

Figure 1-2: The percentage of $\mathrm{PM}_{2.5}$ death cases per sector [11].

1.2 Research Questions

The reduction of fine particle emissions has been analyzed with the help of the following research questions:

1. What is the state of the art technology for fine particle removal?
2. Which particle removal device is the most efficient, and compatible in size and shape, so it can be implemented within the cookstove?
3. What is the best modeling approach for the selected technology?
   (a) What can be done through the analytical approach, and what by using Computational Fluid Dynamics (CFD)?
   (b) Within the framework of CFD, what are the multiphase model methods that can be used?
4. What are the results of relevant simulations for cookstove applications?

1.3 Thesis Outline

Excluding the Introduction, the second chapter explains the state of the art particle removal technology used in the industry. moreover, after an analysis the most optimal solution is chosen and the reasons are elaborated. The third chapter explains the structure of the analytical model used to make preliminary estimates. Next, in the fourth chapter the theory used for the performed simulation is explained. Furthermore, the fifth and sixth chapter analyze the results of the 2D and 3D particle removal simulation, respectively. Finally, the seventh chapter includes conclusions for this thesis and recommendations for future work.

Chapter 2

Particle emission characteristics and possible removal technologies

This chapter gives a brief summary of the problem of particle emissions by woodfired cookstove and then continues with an overview of methods to modify the particle emissions. Special attention is paid to reduction of ultrafine particle emissions by design of air injection in the cook stove and by a turbulent agglomerator implemented in the chimney.

2.1 Particulate matter (PM) emissions

Particle emissions certainly is not only a problem of woodfired cookstoves. The increased usage of fossil fuels for various large scale industrial appliances has triggered an enormous emission of fine particles. For instance, coal is used worldwide in power plants for generating large amounts of electricity. Even though it is an efficient way of producing power it has a huge impact on the environment. The huge concentration of emitted particles will create fogs and hazes [17], which will pollute the ecosystem. Furthermore, after the emission the particles can further react with heavy metals and oxides from the atmosphere and create toxic compounds which a human inhales can cause severe illnesses [17]. Because it is a so widespread problem, methods used elsewhere could be useful for handle the problem in the case of cookstoves.

Particulate matter from wood fired cook stoves poses a large health threat for people living in the developing countries where stoves are most widely used. Due to the insufficient design of the cook stove PM emissions are emitted at high rates and increase the level of indoor air pollution. Furthermore, the size of emitted particles varies greatly, thus the smallest ones are the most dangerous as they can reach deep within the lungs and cause pulmonary and cardiovascular health issues. Thus, people have made various design modifications on the cook stove in hope of reducing emissions, however the results often were not satisfactory for the emitted particles in the fine range. As a solution to this problem certain techniques have been developed to reduce fine particle emission, and they will be elaborated in this chapter. But first we briefly review the particle formation.

2.1.1 Formation

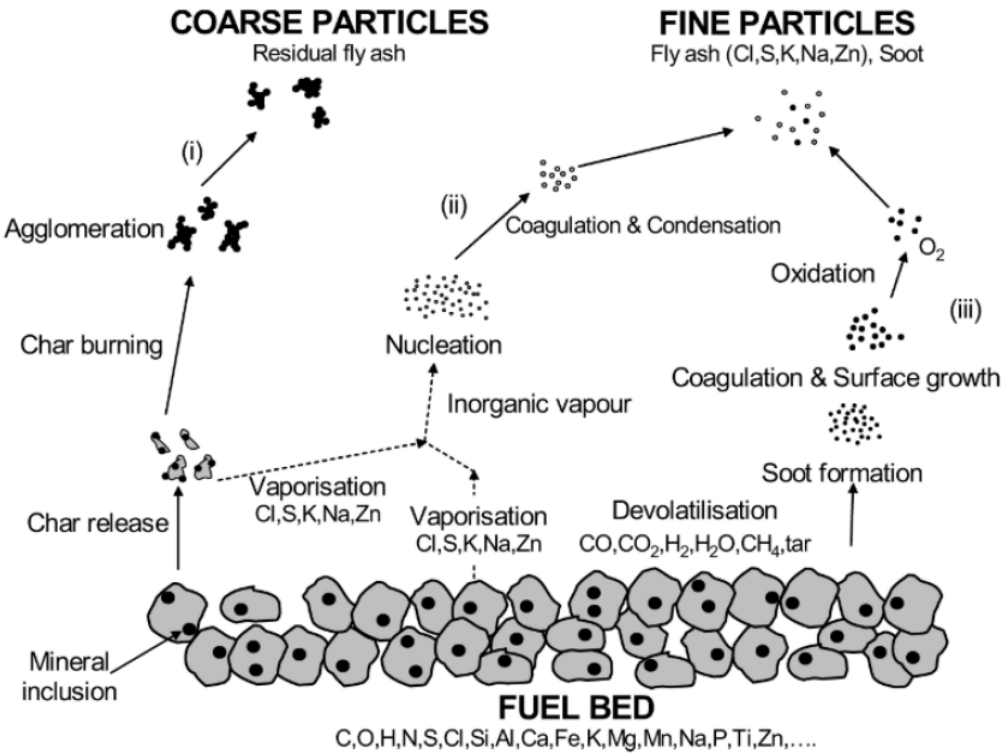

Figure 2-1: Simplified illustration of the particulate formation mechanisms during fixed-bed combustion of a solid biomass [21].

First of all it is important to note that particles are classified based on their size as following:

Table 2-1: Particle size terminology.

	Ultrafine	Submicron	Coarse
$[\mu m]$	< 0.1	$0.1 - 1$	> 1

An overview of the particle formation mechanism is given in Figure 2.1. Coarse fly ash particles are formed from non-volatilized ash entrained in the flue gas. They grow through agglomeration and are ejected from the burner via the gas [35]. On the other hand, sub-micron fly ash particles are formed through homogeneous nucleation of vaporized, easily volatile ash constituents K, Na, S, Cl, and heavy metals like Zn [21]. They can grow by coagulation or heterogeneous condensation on existing seed particles. Furthermore, sub-micron organic particles are called soot, and they are formed in the flames due to the incomplete combustion by complex mechanisms [35]. They will grow through coagulation, latter on oxidize and end up in the fine range.

2.1.2 Health impact

Particles emitted from biomass cook stove combustion cause around 4 million premature deaths annually, and they are responsible for many harmful effects like inflammation, genotoxicity which is toxix damaging to the DNA, cytotoxicity which refers to the ability of certain chemical to destroy living cells and other, which generate respiratory and cardiovascular health difficulties [3]. Furthermore, parameters like particle size and composition influence on the severity of the previously mentioned effects.

2.1.2.1 Size

For fine and ultrafine particles the health effects are more serious because they can reach deeper in the lungs [36]. Thus, the smaller the particle the greater the danger for humans. Furthermore, in theory a weak correlation has been found between Count Median Diameter (CMD) and genotoxicity, and number emission factor and toxicity, which implies that the highly concentrated, small particles have the highest toxicity [12]. However, in practice this statement has not been proven yet [12].

2.1.2.2 Composition

Certain studies [37] claimed that composition is a more important factor than size, and it has a large impact on the toxicological effects [3]. Especially metals are an important PM component because they promote the development of pulmonary and cardiovascular disease [37]. For instance, zinc induces the highest inflammatory responses in the lungs of mice [3]. Furthermore, Polycyclic aromatic hydrocarbons (PAH) are harmful pollutants which are generated during incomplete combustion. Fuels which produce emissions with high concentration of PAH can cause genotoxicity [3]. Therefore, the type of fuel plays an important role on the severity of health effects that PM emissions cause.

2.1.3 Conclusion

Even though the toxicological effects of particles in humans have not been fully understood, it is obvious that small particles and some chemicals pose a big threat for human well being.

Therefore, contributing to development of solutions for lowering fine particle emissions is the primary goal of this thesis and will be discussed in the following. A first factor to be considered is the design of the mixing, combustion and cooling in the cookstove. Optimisation of these aspects can already help to reduce particle emissions. As example in the next section we consider in the next section secondary air injection. Subsequently, the state of the art of particle removal technology will be analyzed in order to find the best best option for using within a cook stove, giving the highest removal efficiency of emitted particles. This is discussed in the remaining sections of this chapter.

2.2 Cookstove design

The cook stove uses primary air injection to promote combustion and heat release from the wood fuel to achieve the highest thermal efficiency. As a result toxic gases and particulate matter emitted which are dangerous for indoor air pollution of the household. Thus, various parameters are optimized in the laboratory through trial and error in order to find the most optimal design. Some of those parameters are geometrical design of the cook stove, flow rate and the speed of the primary and etc. Modifications in air injection design have already been implemented and tested in the industry as a possible solution for decreasing PM emissions. However, sometimes even the most optimal flow rate and speed of the primary air injection cannot reduce the emissions to lower levels, therefore secondary air injection is implemented downstream of the main combustion zone [24].

The position of the secondary air inlet is visualized in Figure 2-2, which represents one of the many possible cook stove designs. Furthermore, several articles have investigated the influence of the previously mentioned variables on the cook stove emissions [24] [22] [47] [8]. It should be noted that in the master thesis of Liam Cassidy [8] a more detailed review can be found. In the remainder of the subsection we will focus on the secondary air injection as it reduces PM emissions by controlling the flow field of the flue gas, and this methodology aligns with the goal of the thesis. Additionally, the dimensions of the cook stove and the position of air injection nozzles are also a very important parameter that have a huge impact on particle emissions, but unfortunately were not considered due to the time constraint.

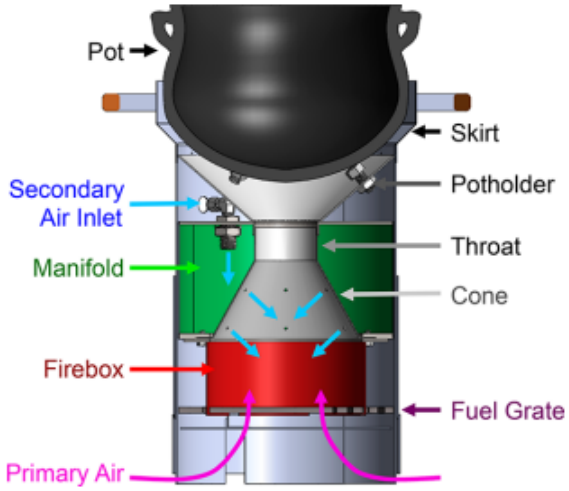

Figure 2-2: Modular Air Injection Cook Stove Design (MOD) section view [24].

Injecting secondary air into the flue gas introduces turbulence in the flow field, which will promote particle collisions and subsequently agglomeration. As a results PM emissions will significantly decrease, but if the optimal conditions are not chosen the number of ultrafine particles will increase [24]. Furthermore, velocity and the flow rate of the secondary air inflow are the most important parameter because they describe the interaction between the secondary air injection and the flue gas. The velocity causes turbulent mixing in the flow field which encourages complete combustion and lower toxic gas and PM emissions [24]. On the other hand, higher flow rates will quench the flames and decrease the temperature of the

combustion zone, thus incomplete combustion will take place and higher polluting emissions [24]. Hence, optimal magnitude of the velocity and the flow rate needs to be selected.

Measurements of the velocity and the flow rate of the secondary air injection in the MOD cook stove haven been performed and the results are summarized in Figure 2-3, Figure 2-4 and Figure 2-5., where the flow rates have been expressed in liters per minute (LPM). Furthermore, the y-axis in Figure 2-3 and Figure 2-5 represents the number of particles of a certain size per kW of cooking power. The following observations were made based on the [24] [22]:

1. From Figure 2-3 we can notice that number of ultrafine particles increases as the flow rate increase. This is because the combustion temperature decreases with increasing flow rate which prevents the oxidation of volatile organic gases or other matter that forms PM emissions. On the other hand, lowering the air-flow rate will lower the mass concentration of particles which will result in reduced coagulation and smaller particle size. Therefore, the number emission of ultrafine particles will decrease. Additionally, in Figure 2-4 for the flow rate of 15 kg s^{-1} the volume distribution is the smallest which indicates better turbulent mixing and better oxidation without lowering the combustion temperature. Lower flow rate would cause insufficient turbulent mixing and higher flow rate would lower the combustion zone temperature, causing higher PM emissions, therefore an optimal value needs to be chosen.

2. In Figure 2-5 the influence of velocity at a fixed flow rate is examined. We can observe that by increasing the air injection velocity the particle emission are decreasing above 10 nm are decreasing. The reason behind such behaviour is that the increase in velocity provides additional turbulent mixing, which will promote the oxidation of volatile gases and decrease particle formation. Therefore, a higher velocity is preferred. Also, for sufficiently small particles the increase in particle velocity does not have an impact.

From the previous observations it is clear that air injection represents a partial solution for decreasing air pollution if optimal flow rate and velocity are chosen. Additionally, the position of the secondary air injection point differs for each cook stove design, meaning that a separate analysis needs to be performed for every cook stove type in order to find the most optimal injection position. But even the best result that can be achieved by air injection design is found to lead to too high particle emissions. Thus, also particle removal methods must be considered, as discussed next.

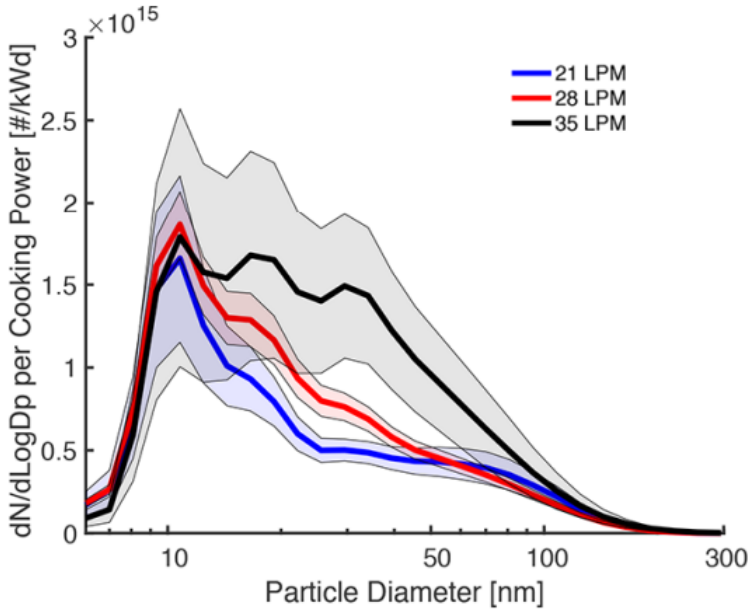

Figure 2-3: Size resolved distribution of total particle number emitted during the cold start, normalized by the cooking power, for three air injection flow rates [24]

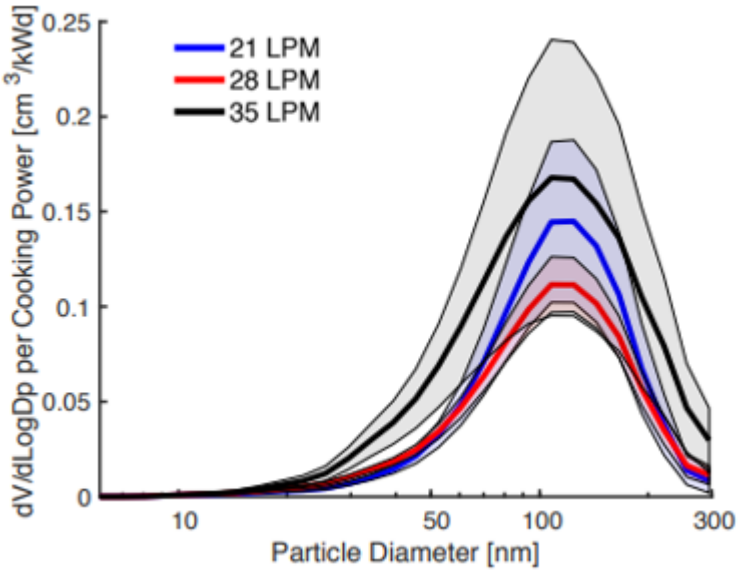

Figure 2-4: Volume distribution of total volume emitted during the cold start, normalized by the average cooking power, for three injection rates settings [24]

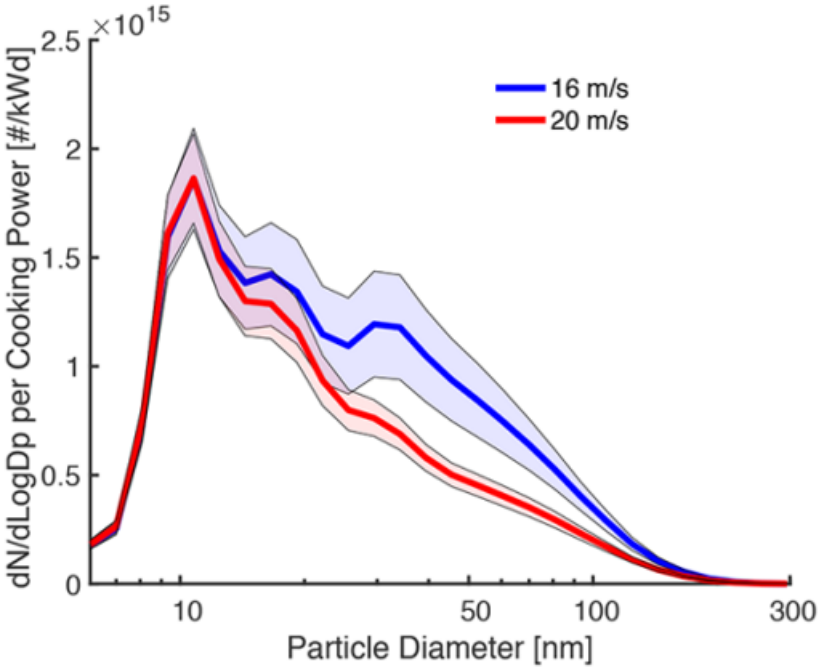

Figure 2-5: Size-resolved distribution of total particle number emitted during the cold start, normalized by the average cooking power, for two air injection velocity settings at a flow rate of 28 LPM: FMPS particle number distribution. [24]

2.3 Particle removal methods

In this section the state of the art of particle removal technology is briefly explained. One particular promising method, the turbulent agglomerator, will be elaborated more in detail.

As a solution to the problem of too high concentration of particles in flue gas often Electrostatic Precipitator (ESP) or Fabric Filters have been used to efficiently capture the emitted particles [20]. ESP's are placed at the end part of the exhaust pipe and use the electrostatic field to first electrify and then remove fine particles. On the other hand, filters are placed inside the exhaust pipe and use a porous medium to capture small particles in micro sized pores of the medium. However, both of this methods have essential drawbacks when applied to cookstoves. The ESP is energy consuming and the porous medium needs to be cleaned frequently. We shall come back to them at the end of this chapter. But there is a more fundamental problem. Even though by using the ESP, cyclone separators or fabric filters we can achieve removal efficiency of over 99 % for $PM_{2.5}$, this devices are not effective for smaller particles [28]. This is bad news because particles that are smaller than $PM_{2.5}$ represent the real danger as they can reach deep within the lungs and severe problems.

Instead we therefore must focus on methods to change the properties of the collection of particles by techniques changing the particle size distribution, by enhancing agglomeration of particles. Agglomeration combines particles to form larger particles and it will lower the fraction of most noxious ultrafine and fine particles, leading to a less harmful emission. Agglomeration can be seen as a pretreatment technology leading to a particle size distribution that afterwards can be handled effectively using ESP and filters if necessary.

There are five types of particle agglomeration technologies:

1. Acoustic agglomeration [28] [10]
2. Chemical agglomeration [17]
3. Turbulent agglomeration [4] [38] [27] [49]
4. Electrical agglomeraton [25]
5. Magnetic agglomeration [52]

The concept behind all these agglomeration techniques is that they reduce the number of small particles by causing them to grow in different ways, which will decrease their numbers in the ultrafine range.
First, acoustic agglomeration uses acoustic sound waves to perturb the flow field and make the particles collide, form bonds and grow [28]. Furthermore, it exhibits high removal efficiency and it is not affected by high flue gas temperatures [28]. Komarov et al [45] after performing experiments with acoustic agglomeration was able to increase the average particle diameter by 51% and reduce the particle numbers by 61%. Also, Zheng et al [28] achieved an efficiency of 45%.
Secondly, chemical agglomeration promotes particle growth by inserting chemical growth agents as spray liquids which first form a liquid bridge between the two particles [17]. Afterwards, the particles will fuse and the chemical droplets will evaporate [17]. Furthermore, Using different chemical agents will impact differently the removal efficiency. For instance,

in the work of Bin et al [17] the coagulation efficiencies of 6.4%,13.1%, 14.6% and 17.1% for water, Polyacrylamide (PAM), pectin and Sodium alginate (SA), respectively. While, Yiquan et al found a larger efficiency of 47.1% and 59.3% for two other agents [16].

In turbulent agglomeration obstacles are placed within the exhaust pipe in order to produce turbulence. The hope is that by the changes in the flow field and the increased turbulence the collision of particles will increase effectively leading to enhanced agglomeration and a decrease in the number of fine particles.

It is possible to combine different agglomeration methods. Sun et al [56] investigated the combined effect of chemical and turbulent agglomeration. Liquid spray droplets were inserted inside the pipe with obstacles and the removal efficiency was measured at the outlet. Thus, the agglomeration efficiency of 45.8% was achieved for when the combined agglomerations were used, while with turbulent agglomeration alone it is around 12%. Therefore, we can conclude that by combining turbulent and chemical agglomeration larger agglomeration efficiency will be achieved than when using it separately.

Nevertheless, with the application in cookstoves as main objective, the effect of only the turbulent agglomerator, which is a passive device, with little or no extra cost, here is selected for further study. We recall that the possibility remains to combine a turbulent agglomerator with an Electrostatic Precipitator, which is especially effective in the removal of larger particles [57] [17].

2.4 Turbulent Agglomerator

A device that enhances particle agglomeration by increasing the level of turbulence of the flow is called a turbulent agglomerator. They are already used in the industry for decreasing fine and ultrafine particle emissions by shifting the particle size distribution to larger scales, but only in systems with much larger power than a cookstove. The enhancement of turbulence is accomplished by perturbing the flow by obstacles. To a large extent the existing knowledge on their efficiency is purely empirical. How turbulent agglomeration works remains a fundamental problem with a lot of complexity. A theoretical framework is described in Chapter 4.

In practice we can find agglomerators of different shapes and sizes due to the one common goal of maximizing the removal efficiency. Usually it is pipe with a circular or rectangular cross section where the length is the more dominant dimension [57] [16] [20] [17]. There is no one single best solution since the problem depends on the turbulence already available in the flow before extra obstacles are added and the type of particle size distribution to be influenced. Therefore the optimisation of the geometry of each agglomerator is a design problem to be addressed.

2.4.1 Geometries tested in industry

In practice there are various shapes of turbulent agglomerators, from the long pipes with a rectangular cross section [57] [16] [20] [17] [38], to the cubic ones [49] [27] [26]. For considering the correct geometry we need to keep in mind the configuration of the cook stove. The main idea is to implement the turbulent agglomerator at a place where the flue gas exhaust is,

and in the case of a cook stove that is the chimney. Furthermore, an advantage is that the dimensions of the chimney are similar to the turbulent agglomerator, therefore we can directly select the agglomerators from the literature without re-scaling them. We selected for further study the four agglomerators studied in the work of Sun et al [57]. Before making our final choice we briefly describe all four.

The configuration of the four turbulent agglomerators that were in consideration are shown in Figure 2-6, with the remark that the fourth one has the same arrangement and dimensions as the second one. There is a difference between both in the form of the vortex sheets but it cannot be seen from the view direction in the figure. All agglomerators have length $1320mm$ and square cross section of $100mm \times 100mm$. Furthermore, they all have two rows of eight obstacles, called 'vortex sheets', at both sides of the centerline with equal spacing between them. Other dimensions can be seen in Figure 2-6.

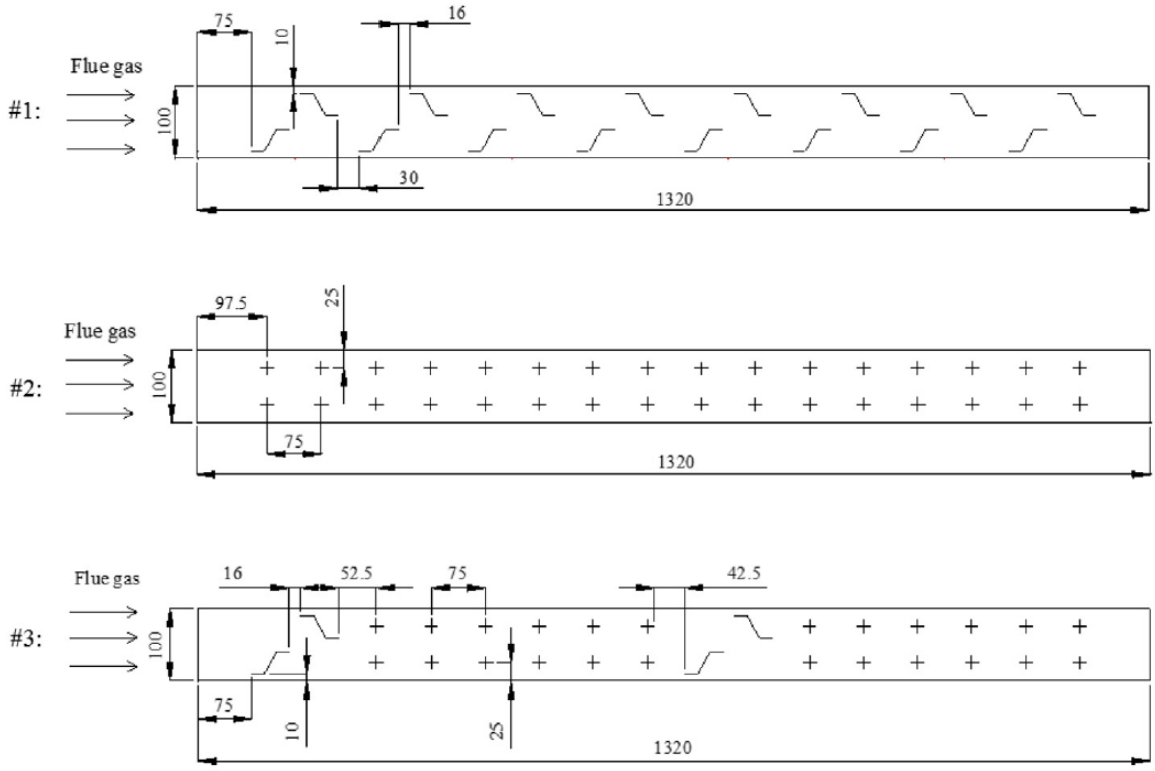

Figure 2-6: Geometry of the turbulent agglomerators [57].

The 3D configurations of the turbulent agglomerators can be seen in Figure 2-22. And the dimensions of the vortex sheets are shown in Figure 2-8. This clearly shows the different geometry of Z-type vortex sheet and cross type vortex sheet. Turbulent agglomerator 3 layout is not shown here since it is a combination of the 1 and 2.

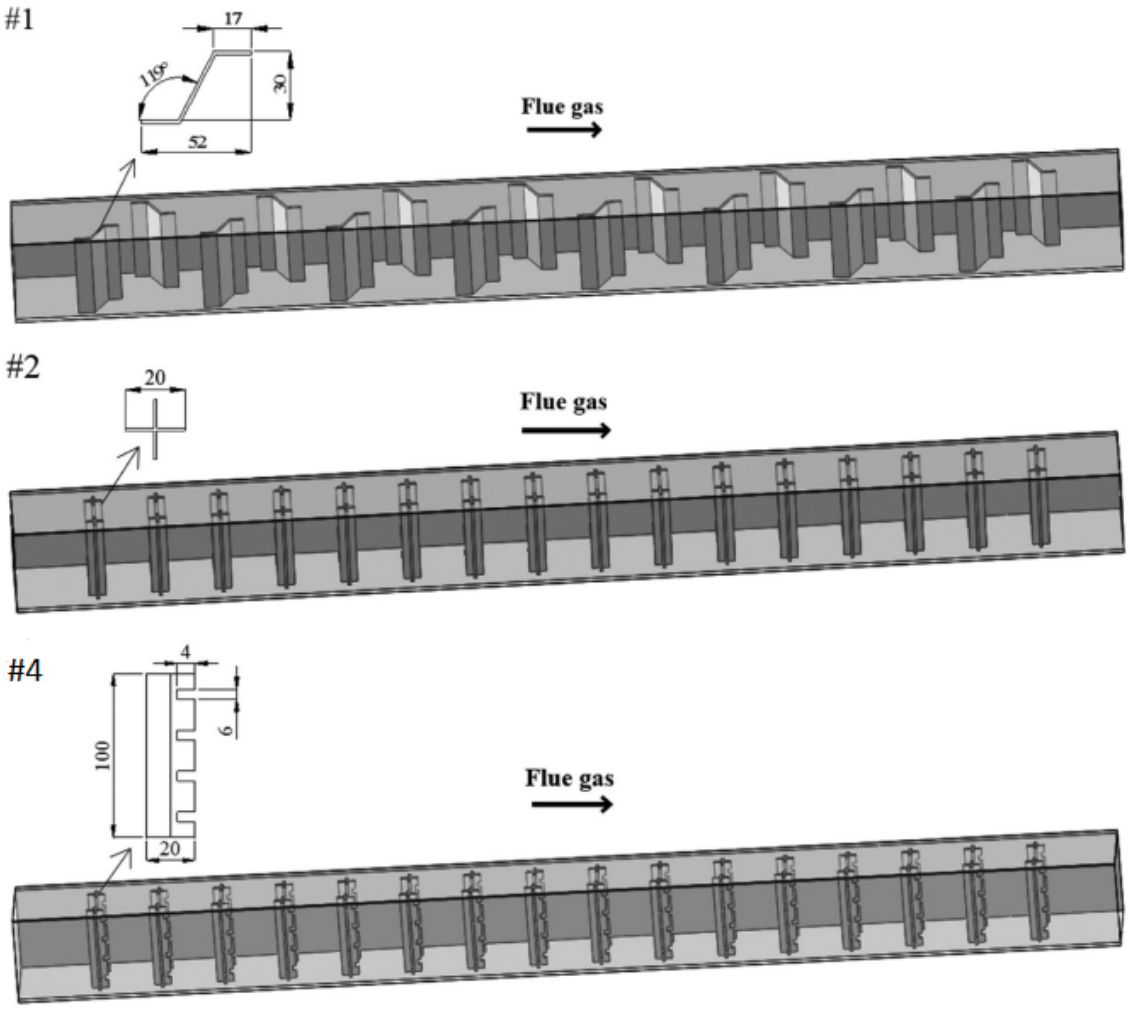

Figure 2-7: Structure of the turbulent agglomerators 1, 2 and 4 [55].

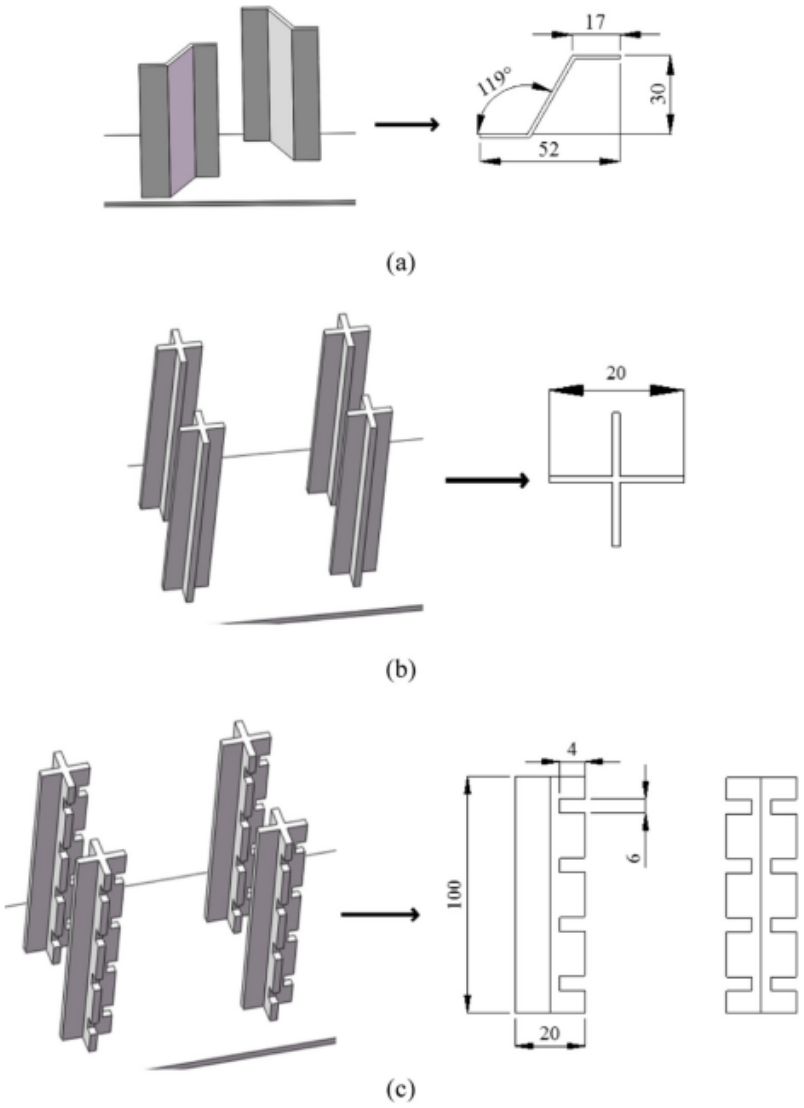

Figure 2-8: Structure of the vortex sheets in turbulence generators. (a) 1; (b) 2; (c) 4 [56].

2.4.2 Experiments

The experimental setup used in Ref. [57] is shown in Figure 2-9. It was created so that it can simulate the motion of a real life flue gas in all four previously mentioned turbulent agglomerators. First air is injected at a flow rate of $300\frac{m^3}{h}$ in a gas heater, which heats the air to about $150°C$. Afterwards, the heated air enters the buffer vessel with a stirrer. Furthermore, the vessel is connected with the solid aerosol generator which contains sampled fly ash particles from a coal-combustion power plant with a size distribution that is ranged from 0.26 to 149 μm [57]. Next, the stirrer mixes the heated air and the injected fly ash articles so that it can make a similar texture as the flue gas. Later on, the mixture enters the turbulent agglomerators. Valves are placed at the inlet of the agglomerators to limit the inlet speed at $10\frac{m}{s}$. Measurement devices such as the electrical low pressure impactor (ELPI+) are placed both at the inlet and the outlet of the agglomerators so that they could measure the Particle Size Distribution and calculate the agglomeration efficiency. ESP is placed after the turbulent agglomerator in order to remove fly ash particles.
The particle size distribution was measured at the outlet of the three turbulent agglomerators, for the cases with and without the ESP, and the results are represented in Figures 2-10-2-11. The black line from the graphs represents the initial particle distribution in the flue gas. Furthermore, the results for turbulent agglomerator were shown separately in section A.1 of the Appendix A, as a different initial distribution for the flue gas was considered.

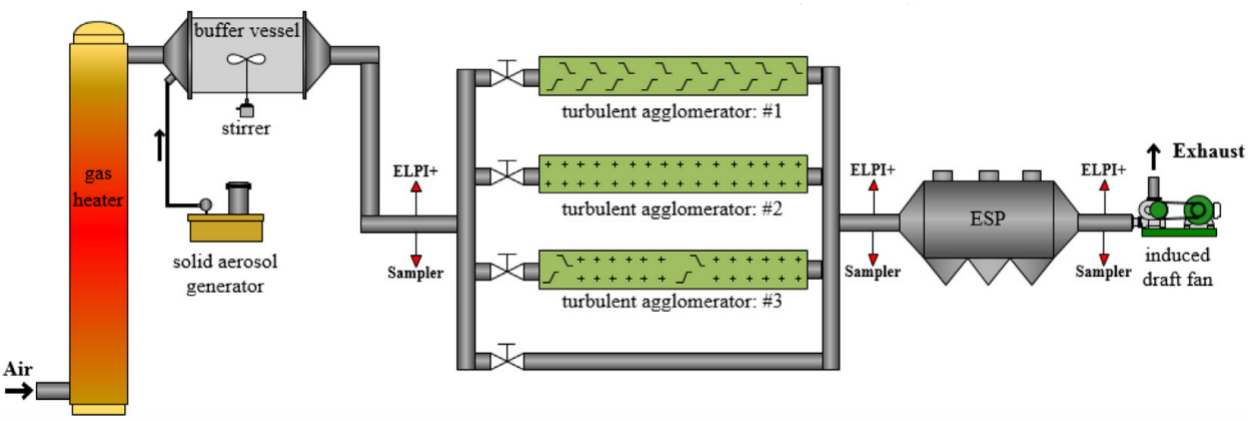

Figure 2-9: Schematic diagram of the experimental setup [57].

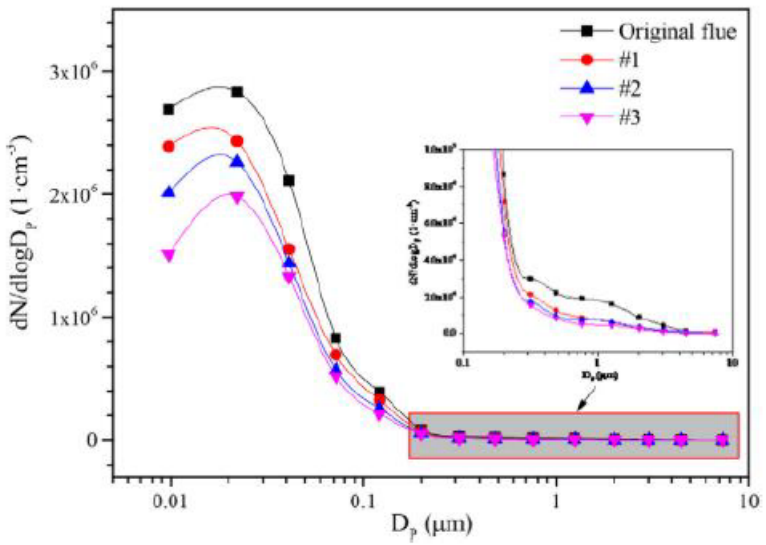

Figure 2-10: Particle size distribution in the flue gas for cases without (original flue) and with(cases 1-3) turbulent agglomerator [57].

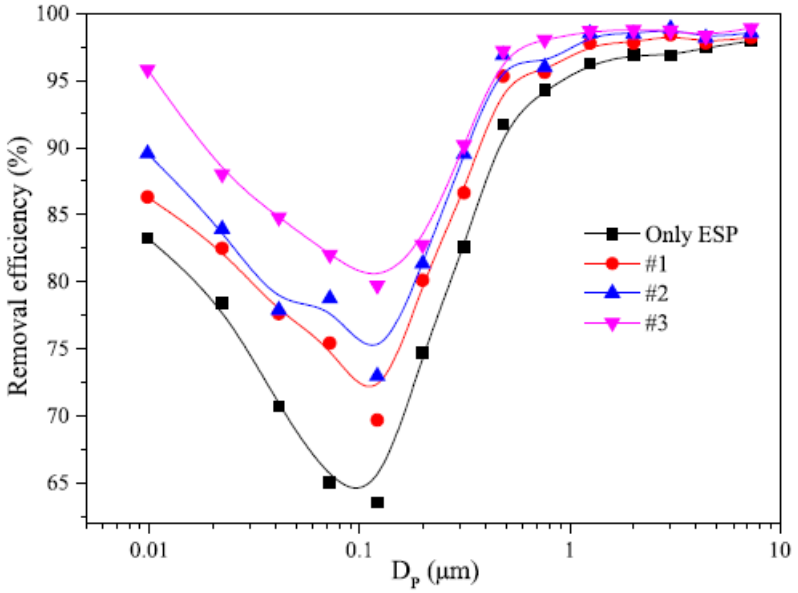

Figure 2-11: Removal Efficiency of the ESP after turbulent agglomeration [57].

2.4.3 Computed flow fields

The mean flow field of the turbulent agglomerators was computed in Ref. [57] using ANSYS Fluent using the k-ϵ model in order to get a better insight in the flow. From Figures 2-10 - 2-12 we can notice the existence of a large and small scale vortex structures which are created due to the vortex sheets. The large scale vortexes contain a higher amount of energy which they obtain from the main flow [57]. In the turbulent flow that energy is transferred to smaller vortexes through the process of nonlinear splitting until of turbulence cascade until the smallest scale of turbulence is reached [57]. Then their mechanical energy is converted into heat energy due to the viscosity of the fluid [57]. The mean flow field obtained using the k-ϵ model only shows the large vortexes. The location and size of those vortexes depends on the layout of the vortex sheets. Due to the varying arrangements of the vortex sheets inside the agglomerators the velocity flow field will have a different pattern and magnitude for each case.

At the beginning of the flow we see a spatially uniform mean velocity distribution of $10\frac{m}{s}$. When the flow passes the vortex sheets turbulence level increases. Behind the obstacles a wake region appears with low mean velocity and longer residence time. Most of the flue gas will pass directly via the region between the two rows of vortex sheets. Consequently, due to the steadiness of the flow and mass conservation the velocity in this region will increase. In summary, the flow field is divided into the main-flow and the back-flow region [57], where the first indicates the high speed region while the second specifies the low-speed (wake) region. The maximum mean velocity that is achieved is around $33\frac{m}{s}$ in turbulent agglomerator 3, while the minimum is below $5\frac{m}{s}$ [57] for all four cases. This indicates that the highest gradients of mean velocity acting as source for turbulent kinetic energy are present in turbulent agglomerator 3. Therefore it will have the highest turbulence intensity.

We can also observe that the wake regions are largest in agglomerator 1 while smaller ones are present in 2 and 4. The Z-type vortex sheets produce produce a large vortex and the cross type create smaller ones. On the other hand, in agglomerator 3 both Z-type and cross vanes are used, thus it will contain large and small scale vortexes. These vortexes have an immense impact on particle motion and residence time, but that will be discussed in subsection 2.4.4.

Additionally, we can notice from the x-z plane that the z velocity component for agglomerators 1, 2 and 3 is much smaller than for the agglomerator 4. Hence, in the first three cases there is no turbulent mixing in the z direction, thus only 2D vortexes will be produced. On the other hand, due to the small incisions on the vortex sheets of agglomerator 4 more flue gas will pass at a higher velocity in z-direction resulting in turbulent mixing and the creation of 3D vortex sheets. The advantage of the 3D vortex sheets is that turbulence is happening in both the x-y and x-y plane, which will cause a more chaotic motion for the particles and increase the collision frequency.

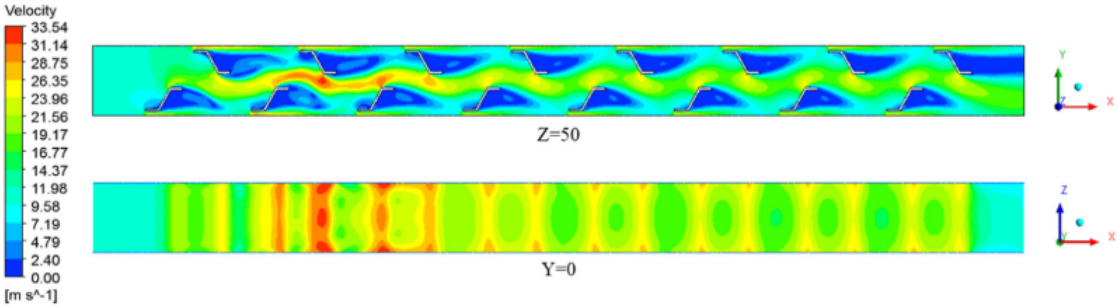

Figure 2-12: Velocity field of the turbulent aggloemerator 1 [56].

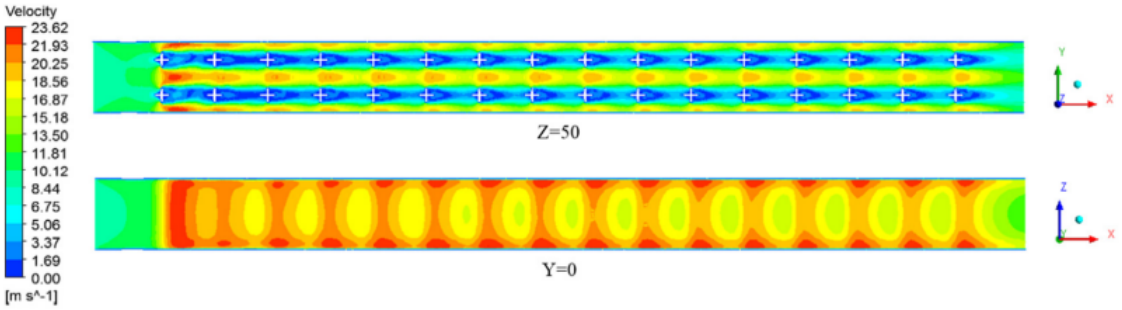

Figure 2-13: Velocity field of the turbulent aggloemerator 2 [56].

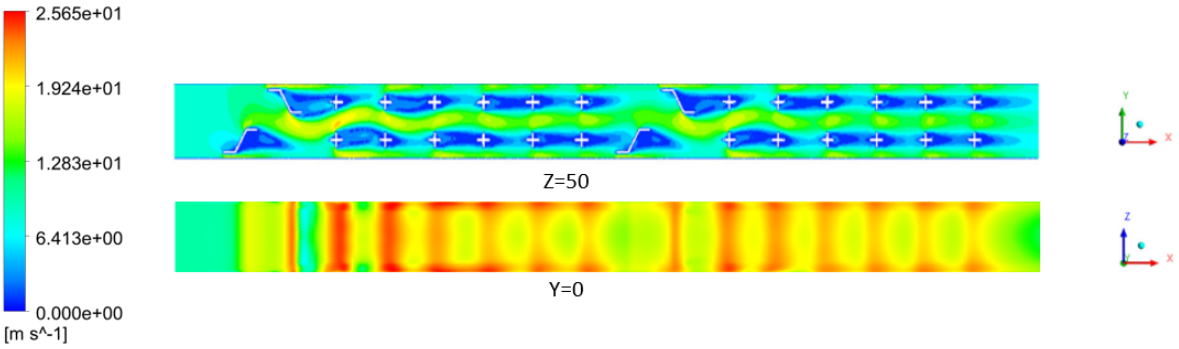

Figure 2-14: Velocity field of the turbulent aggloemerator 3 [57]

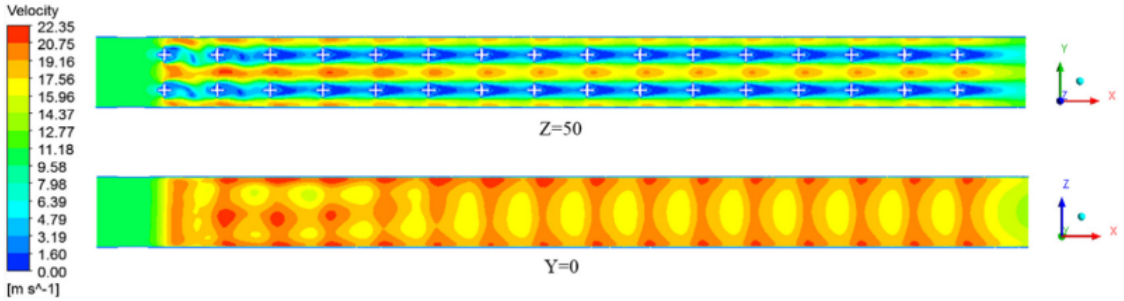

Figure 2-15: Velocity field of the turbulent aggloemerator 4 [56].

2.4.4 Computed particle tracks

The analysis of the particle motion is important in order to understand the agglomeration efficiency of the turbulent agglomerator. By using the Discrete Phase Model in ANSYS Fluent it is possible to track the particle paths and observe the location and residence time of particles of different sizes. Thus, by knowing this quantity we can keep modifying the shape of the vortex sheets until an optimal design has been reached in which the particle residence time and the collision frequency is the highest. The simulation of particle paths has not been combined with a simulation of particle collisions. Therefore this method does not provide a complete model for the evolution of particle size.

Furthermore the k-ϵ model does not provide a detailed description of the motion of particles in the flow, but contains modeling assumptions. This is explained in more detail in Chapter 4. But it is worth explaining the basics here.

The Stokes number ($\mathbf{S_T}$) is a non-dimensionless number describing how well particles follow the flow. By definition it is equal to:

$$S_{tk} = \frac{\tau_p}{\tau_K} \tag{2-1}$$

Where,

$$\tau_p = \frac{\rho_p d_p^2}{18\rho_g \nu} \tag{2-2}$$

$$\tau_K = \left(\frac{\nu^3}{\varepsilon}\right)^{\frac{1}{2}} \tag{2-3}$$

τ_p is the particle relaxation time (characterising the time needed to arrive at the state where surrounding flow and particle have the same velocity), and τ_K is the Kolmogorov time scale (the time scale of the smallest vortices), d_p is the particle diameter, ρ_p and ρ are the particle and fluid densities, ν is the fluid kinematic viscosity, ϵ is the turbulent dissipation rate of the flow. The value of the Stokes number provides the information needed to know whether or not a particle will follow the flow of the small vortices or rather follows a path determined by its own inertia. (Using other characteristic flow velocities, corresponding other Stokes numbers can be defined).

Particles with an $\mathbf{S_T}$ smaller than 1 tend to follow the flow, while particle with $\mathbf{S_T}$ bigger than 3 can move independently due to bigger size and inertia [57]. In the literature [57] [55] the Stokes number for the particle size of $1\mu m$ and $10\mu m$ in the flow considered here was calculated and the results are listed in Table 2-2

Table 2-2: Stokes number for different turbulent agglomerators.

	S_{T1}	S_{T2}	S_{T3}	S_{T4}
$1[\mu m]$	0.17	0.13	0.13	0.12
$10[\mu m]$	16.35	12.63	12.77	11.65

From the calculation we can conclude that all particles in the fine range will follow the motion in small vortices, while larger coarse particles will have an independent movement. Because larger vortices have a longer time scale, the particles will also follow motions induced by larger vortices and also follow the flow lines of the mean flow predicted by the k-ϵ model. Nevertheless there is a complication because the k-ϵ model only predicts the mean flow. The influence of the smaller vortexes on particle motion, leading to a a spatial dispersion of particles is not described by the just the mean flow field and the model for particle motion in turbulent flow needs a closer model for that. Including this the difference of the motion between small and large particles can be obtained.

This is visualized in Figures 2-16 (a)-(c) and 2-17, where the streamlines of the mean velocity field of the four turbulent agglomerators is compared to the particle paths with a diameter of $0.1\mu m$, $1\mu m$ and $10\mu m$. We can notice that particles in the fine range follow the streamlines, while the coarse particles have an independent movement, thus, this confirms the effect of the Stokes number.

More precisely, coarse particles mainly move along the centerline of the agglomerator with small fluctuations in the transverse direction (y-direction). On the other hand, smaller particles deviate more easily from the streamlines and largely end up in the wake region. In the case of agglomerator 1 we can observe that most of the coarse particle are concentrated in the main flow region without entering the back-flow region. Thus, collision between coarse and fine particles will happen rarely and agglomeration will mainly be between fine particles [57]. In the case of cross-type vortex sheets of agglomerator 2 we can notice that the back-flow region is smaller than at the agglomerator 1, and that the particles transitioned fast and frequently from wake to the main-flow and vice versa [57]. Thus, this results in a shorter residence time of fine particles in the wake, but increases it in the main flow resulting in an decreased agglomeration among fine particles, but an increase between fine and coarse particles [57]. Agglomerator 3 and 4 will support both agglomeration mechanisms. However the agglomeration efficiency will be different due to the difference in the y-direction fluctuations and the particle residence time, but this will be more discussed in subsection 2.4.5.

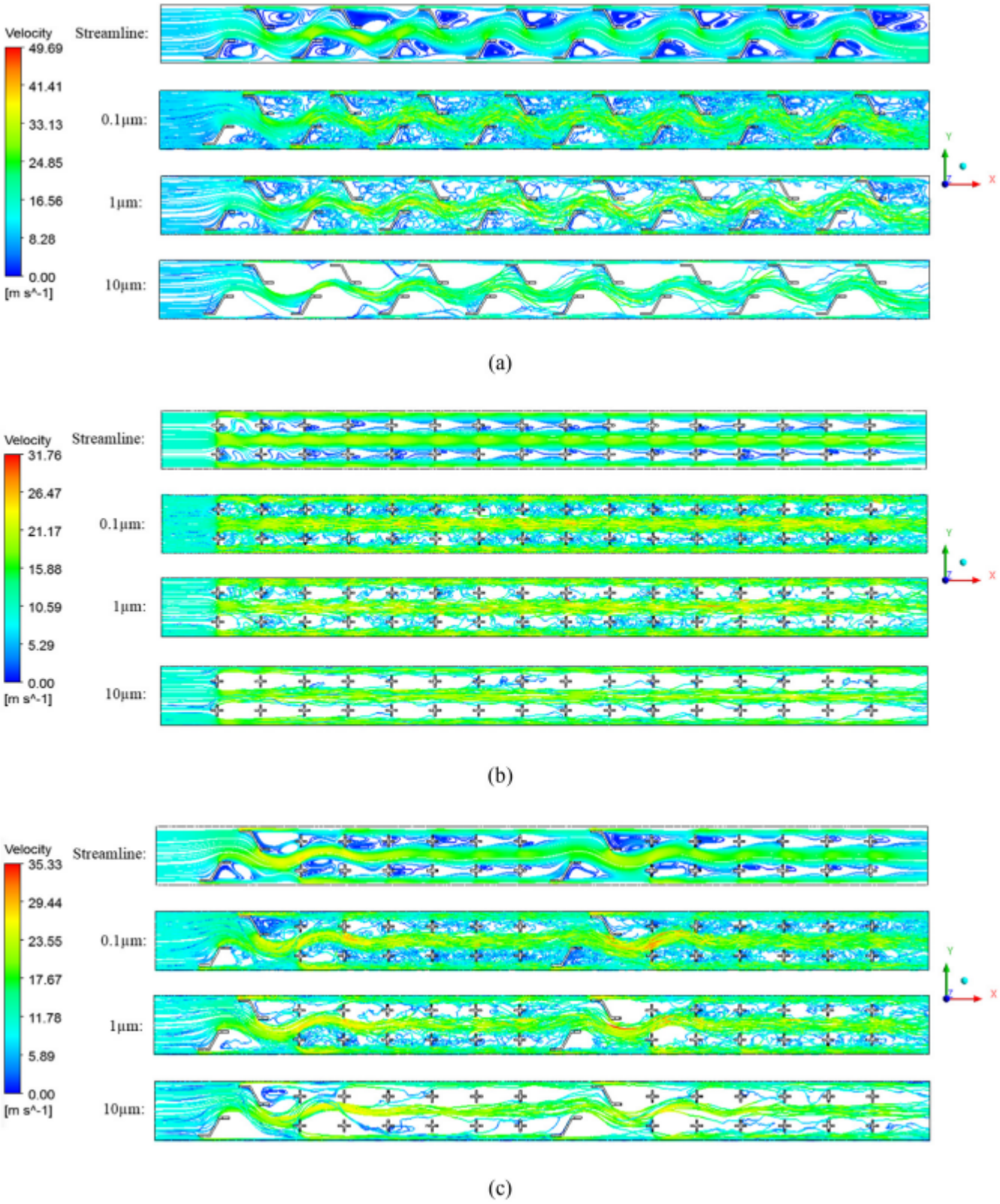

Figure 2-16: Particle motion in turbulent agglomerators 1, 2 and 3[57].

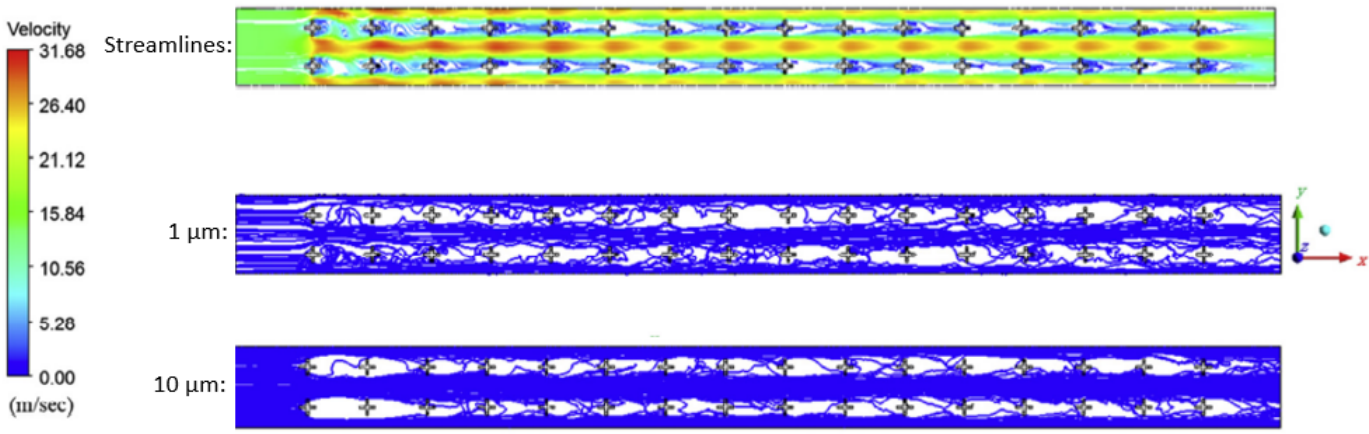

Figure 2-17: Particle Motion in turbulent agglomerator 4 [55].

2.4.5 Efficiency

The agglomerator is used to decrease the number of small particles. It is most efficient if all small particles have disappeared. It is defined quantitatively by the relative change in number of particles in a certain size class denoted by an index i as follows:

$$\eta_{N_i} = \frac{N_{i0} - N_{it}}{N_{i0}} \times 100 \tag{2-4}$$

Where N_{i0} and N_{it} are the number of particles of size class i at the inlet and the outlet of the turbulent agglomerator and the result is expressed as % change compared to inlet conditions.

It depends on the particle residence time and the y-direction fluctuations as described above. The obtained computational results for these quantities for particles of size 1 μm and 10μm are shown in Figure 2-18 and Figure 2-19 for each case.

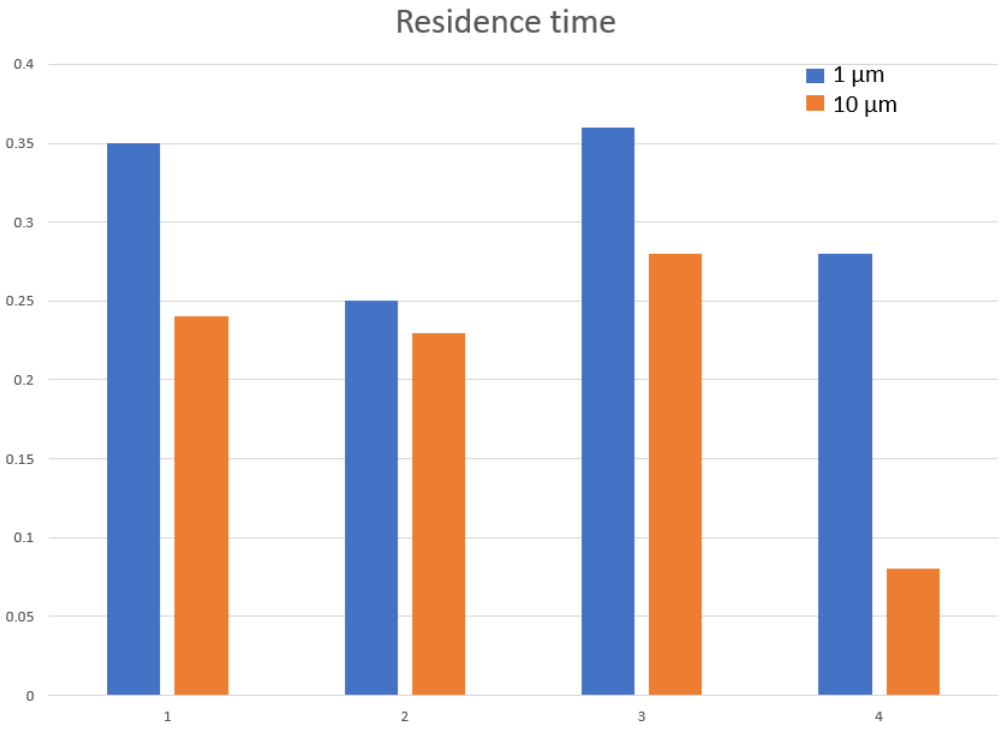

Figure 2-18: Particle residence time [57] [55].

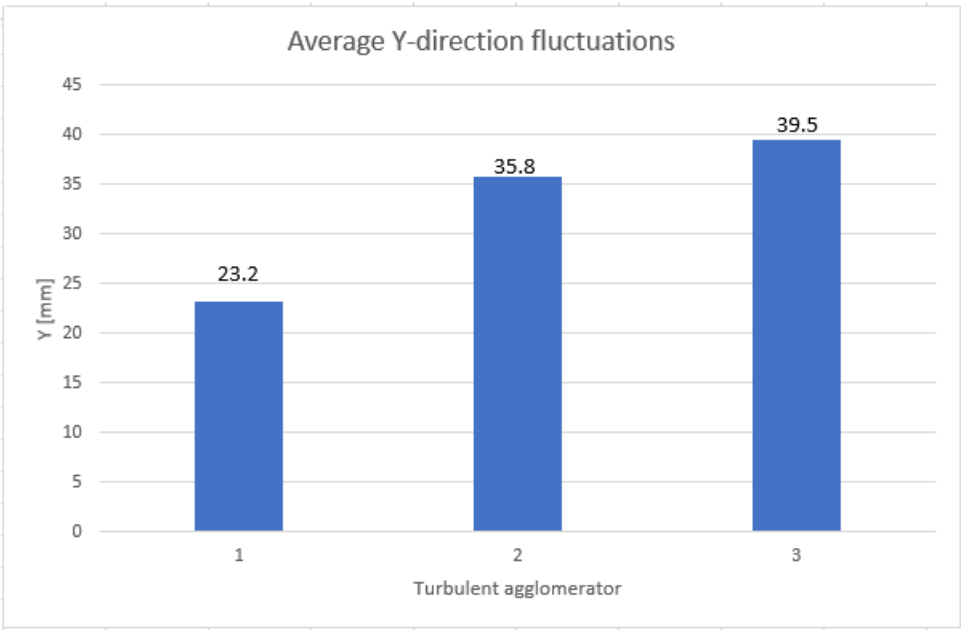

Figure 2-19: Y-direction fluctuations [57].

Thus, based on the shown data the turbulent agglomerator number 3 is the most efficient due to the highest residence time of fine and ultrafine particles and the highest Y-direction

fluctuations of coarse particles. This is in agreement with the experimental data listed in Table 2-3, where we can see that the turbulent agglomerator 3 exhibits the highest agglomeration efficiency for the particles in the ultrafine range. The performance of this agglomerator will be studied in Chapter 5 using an alternative computational model (sectional method for particle size distribution) and for a mean flow velocity characteristic of a cookstove chimney.

Table 2-3: Agglomeration efficiency for ultrafines (%) [57] [55].

	Agglomerator 1	Agglomerator 2	Agglomerator 3	Agglomerator 4
η	15.9	25.4	37.8	30.1

2.4.6 Combination with Electrostatic Precipitator(ESP)

The agglomerator only changes the size distribution and does not influence the total emitted mass of particles. To really remove particles additional devises are needed. Here we discuss the Electrostatic precipitators (ESP), a commonly used device for collecting fly ash particles. They are used in large scale appliances such as coal power plants for removing the dust particles, and in the metallurgical and the construction industry etc. [50]. Also, it is implemented in the chimney of small scale biomass combustion stoves for collecting emitted particles in order to decrease indoor air pollution [2] [7]. Furthermore, ESP is able to achieve the removal efficiency of 99.9% for for coarse fly ash particles, while for particles below the submicron range the capture efficiency is much lower due to the low electric charge [50]. Therefore the use of methods to make particles grow and shift the PSD to larger size, describes in previous sections enhances it operation. Combined with an agglomerator the ESP will collect more particles and the the removal efficiency will increase. Thus, that is why a lot of research is being conducted regarding this topic [57] [17] [20] [16] [56] [28] [10].

Keeping in mind that the goal of the thesis is to reduce particle emissions from a wood fired cook stove, a possible ESP structure for a small scale biomass fired stove is briefly considered here. It is represented schematically in Figure 2-20. The main components are the electrical corona wire and the grounded cylindrical collecting electrode. The flue gas enters into the ESP from the chimney and the fly ash particles get negatively charged by the corona wire. Afterwards, the positively charged electrode will attract the particle via the electrostatic Coulomb force and remove them from the flue gas.

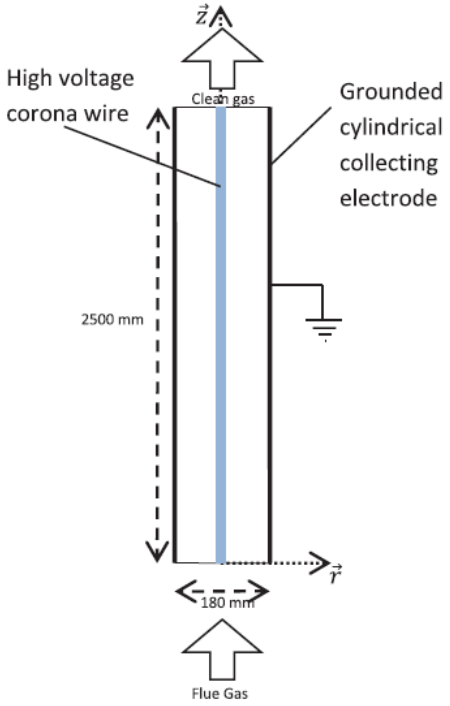

Figure 2-20: Electrostatic precipitator for a small scale biomass stove[57].

The result of using the four turbulent agglomerators in combination with the ESP on the total particle removal efficiency is shown in Table 2-4.

Table 2-4: Average Removal Efficiency [57] [55].

	Agglomerator 1	Agglomerator 2	Agglomerator 3	Agglomerator 4
η	81.5	84.43	87.5	89.1

We can see that the highest efficiency is exhibited by turbulent agglomerator 4 which is maybe due to the 3D vortex sheets which are formed. However, for our further analysis we stick to agglomerator 3 because we are only considering particle agglomeration. Furthermore, in Figures 2-11-A-2 the PSD before and after the use of turbulent agglomerator coupled with ESP is shown, while the black curve symbolises the use of only ESP. We can notice a strange behaviour where for the first three aglomerators the removal efficiency decreases as the particle size increases up to $0.1\mu m$. On the other hand, in this size range for agglomerator 4 the removal efficiency curve is fluctuating. The explanation behind for this behaviour has not been found in the literature. For particles outside the ultrafine range the collection efficiency will increase as the size increases, and this is due to the fact that larger particles have larger charge capacity, thus also the attraction Coulomb force will be stronger [6].

Additionally, parameters such as the flue gas temperature, flue gas velocity and the operational voltage of the electrostatic precipitator influence the collection efficiency of the ESP. The previously mentioned parameters are all connected among themselves, thus by affecting one the other will also exhibit some changes. For instance, the increase of the flue gas temperature will:

1. Decrease the density of the flue gas which will result in higher gas flow speeds. Consequently, the residence time of particles inside the ESP will decrease, which will result in lower efficiency [1].

2. Decrease the operational voltage of the electrostatic precipitator. This will lower the particle charging and weaken the electric field force; therefore, the collection efficiency of the ESP will be reduced [48]. On the other hand, if we keep the operational voltage constant while the flue gas temperatures varies the collection efficiency will be higher at higher temperatures [48].

One of the drawbacks of using the ESP is that it requires a constant energy supply while it operates because it uses electricity to attract and collect particles. The additional energy consumption will result as an additional cost. Therefore, the price of the device and its energy costs make this method economically unattractive for small scale biomass combustion appliances.

2.5 Filtering using a porous medium

A porous medium is a material consisting of a solid matrix surrounding narrow flow channels. It can be used for filtering if some constituents of the flow adhere to the solid surface. In flue gas cleaning applications we need material which can withstand large temperatures, like ceramics, in order to avoid melting. Porous filters made from such materials are used for lowering the PM and harmful gas emissions of the flue gas in large scale coal power production facilities [33] [32]. Also, ceramic porous plates are used in small scale biomass combustion appliances for reducing indoor air pollution [30] [13].

Furthermore, as wood fired cook stoves are classified under small scale biomass combustion the porous medium mentioned in [30] [13] will be briefly discussed. Nevertheless, in [30] the ceramic foams (Silicon Carbide) are implemented in the combustion chambers of the residential wood stoves. Different configurations were tested which resulted in a 20% average decrease of the particulate matter emission factors. The most optimal configuration was when the porous plates were placed near the walls, thus the emission factors decreased 61%.

Additionally, in [13] the PM emission was measured for ceramic porous plates of varying thickness and varying air inflow rates. From the experimental setup configuration presented on Figure 2-18 we can visualize how the plates are placed within the combustion chamber and at what locations air is entering the domain. Nonetheless, it was concluded that thicker porous plates have lower PM emissions and that by increasing the air flow rate the emissions of particulate matter reduce [13].

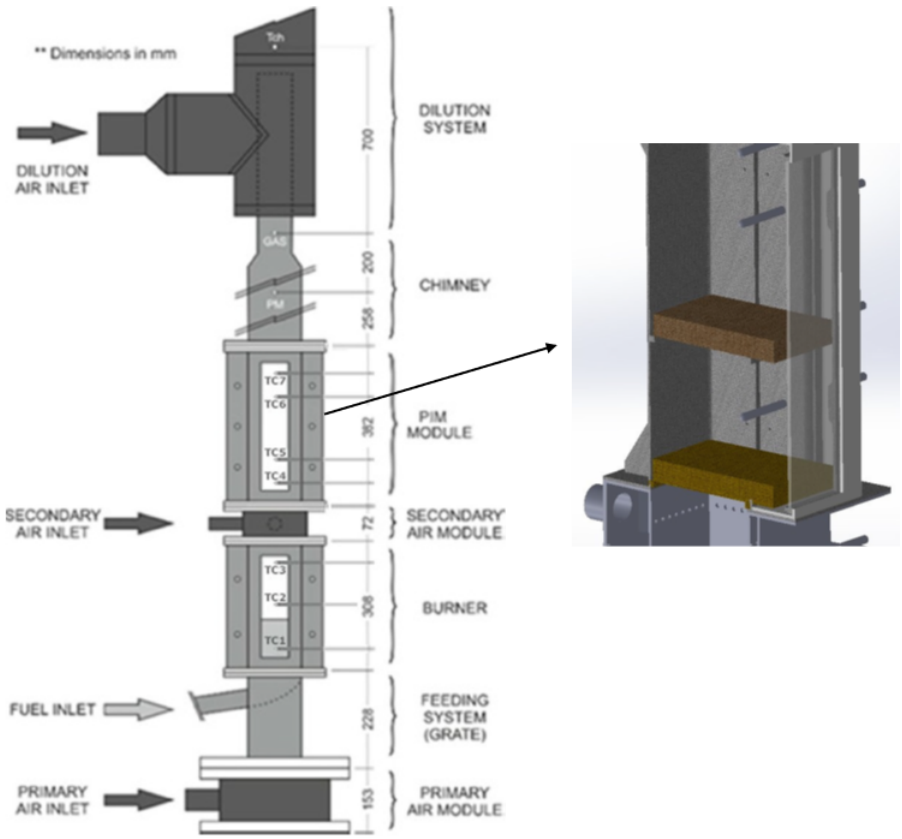

Figure 2-21: Combustion chamber with porous plates [13].

Apart from experiments, simulations of the flue gas movement through the porous medium have been performed in order to analyze the removing efficiency of fine and ultrafine particles [15]. Furthermore, two mechanisms were identified for deposition of sub-micron particles on the porous media [15]:

1. Brownian diffusion, which is caused by random motion of particles.
2. Sedimentation, which is a consequence of inertial acceleration and adhesive forces.

As a consequence of the first deposition mechanism, Brownian removal efficiency is obtained and it is expressed as a function of the Peclet number, while the Sedimentation efficiency is a consequence of the second and it is a function of the Gravity number. Both Peclet and the Gravity number are non-dimensional quantities which have been further explained in **AppendixA**.. Furthermore, the behaviour of these efficiencies with respect to their non dimensional numbers, have been represented on Figure 19 and Figure 20.

From Figure 19. the Brownian efficiency increases as Peclet number (**Pe**) decreases which indicates that porous media with smaller grain sizes has higher efficiency. In Figure 20. the Sedimentation efficiency is increasing as the Gravity number ($\mathbf{N_G}$) increases, which indicates that the efficiency will increase with increasing particle size (up to 1 m) due to the bigger inertial acceleration effect. Furthermore, both efficiencies depend on the Reynolds number ($\mathbf{R_e}$) and as it increases both efficiencies will decrease [15], meaning that as the flue gas flow speed through the medium increases less particles will be captured.

The advantage of using the porous media is the easy implementation as it can be fixed anywhere within the combustion chamber or the chimney in our case. Also, compared to the agglomerator it saves time in construction as it does not require vortex sheets which can be quite complex to make. Furthermore, it does not need an energy supply as the ESP. On the other hand, it requires frequent maintenance as pores have small load capacity.

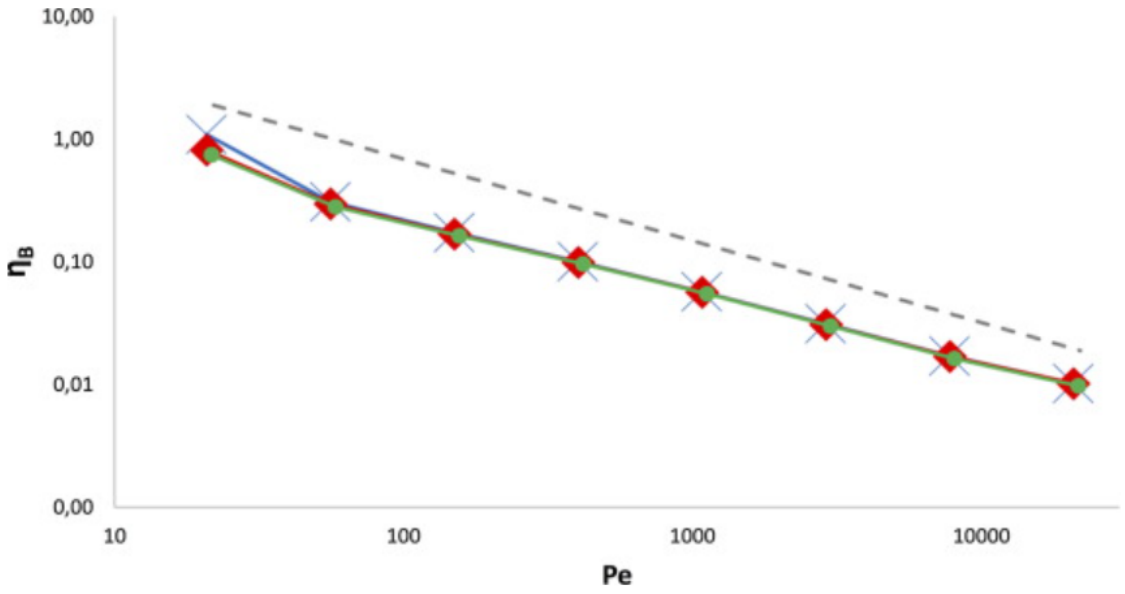

Figure 2-22: Brownian removal efficiency with varying Peclet number [15].

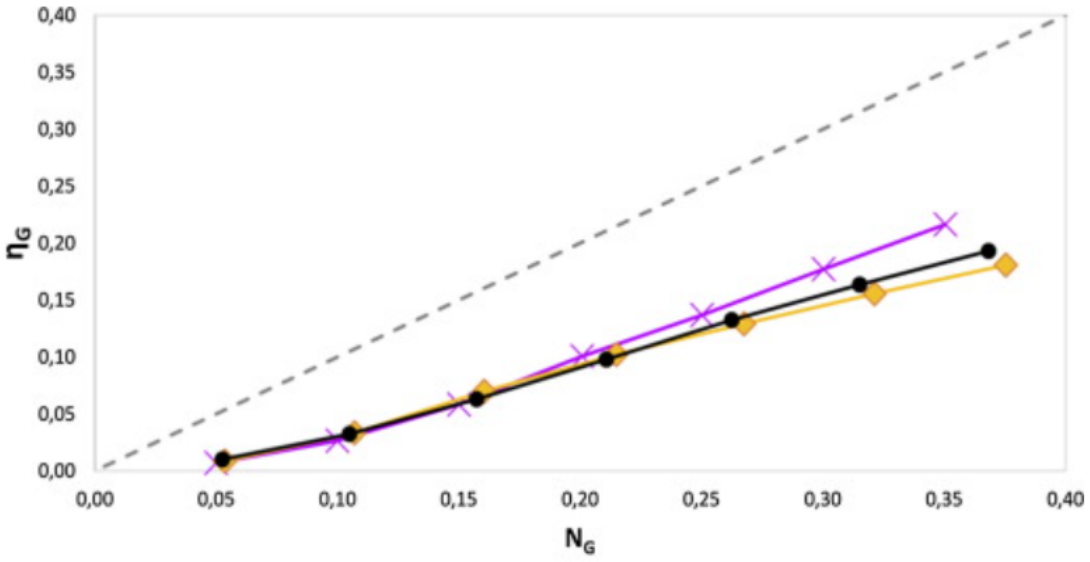

Figure 2-23: Sedimentation removal efficiency with varying Gravity number [15].

2.6 Conclusion

The following conclusions have been made:

1. The dimensions of the turbulent agglomerator are similar to the dimensions of the cook stove chimney, thus ti can be easily implemented within the design.
2. The flow field within the turbulent agglomerator can be divided into the high speed main-flow region where mainly coarse fly ash particles travel independently due to their high inertia, and the low-seed back-flow region which is located behind the vortex sheets and has a high concentration of fine particles because they follow the flow field due to low inertia.
3. There exists two types of particle agglomeration mechanisms, one that refers to the collision and fusion between two fine particles in the back-flow region, and the second one which implies the removal of fine particle by collision and coagulation with coarse.
4. The combination of z-type and cross-type vortex sheets produce a pattern of large and small scale vortexes, which give the highest residence time of fine and ultrafine particles and the highest Y-direction fluctuations of coarse particles. Therefore, turbulent agglomerator 3 will result in the highest agglomeration efficiency of 37.8% for particles in the ultrafine range, under the inlet velocity of $10\frac{m}{s}$.
5. As it gives the highest agglomeration efficiency for particles in the ultrafine range, turbulent agglomerator 3 will be further analyzed in the thesis to see if it can produce a similar agglomeration efficiency under normal cooking conditions.
6. Using the combination of ESP and turbulent agglomerator will result in giving the highest removal efficiency of ultrafine and fine particles. However, economic consequences will follow due to the price of the ESP and the additional energy consumption.
7. Turbulent agglomerator 4 presents the best fit for the ESP as they give the highest removal efficiency when coupled. However, agglomerator 4 does not give the highest agglomeration efficiency individually, thus it is not considered for furhter research.
8. Porous media uses the Brownian and Sedimentation deposition mechanism for capturing fine and ultrafine particles with their pores. Based on the behaviour of the efficiency curves from Figure 19 and Figure 20 it was concluded:
   (a) Porous media with smaller grain sizes have higher efficiency.
   (b) Sedimentation efficiency will increase with increasing particle size up to 1 μm.
   (c) As the flue gas flow speed through the medium increases less particles will be captured.

Chapter 3

Temperature, mass flow rate and pressure drop

3.1 Introduction

Before performing CFD simulations it is important to estimate certain quantities regarding the cookstove operation, especially when the CFD calculation only concerns a part of the complete cookstove. In this work the CFD simulations only concern the chimney with agglomerator installed. Important information to be supplied are the expected flow velocity and temperature at the inlet of the chimney. In this chapter this information is obtained based on a simple algebraic model if the flow and heat transfer in the complete cookstove. To be specific we consider a Plancha type cookstove, because it typically has a long cylindrical chimney which provides space for an agglomerator. The model used here was initially created by Prapas et al [41] in MATLAB, but minor corrections were made to the code in order to obtain what we need here.

A Plancha wood fired cook stove consists of the combustion chamber which is made of firebrick because it can withstand high temperatures and the round vertical chimney which is made of stainless steel. Furthermore, the two parts are connected by the stove channel, that is made from cast iron, and the complete structure can seen in Figure 3-1.
Pine wood fuel is inserted into the combustion chamber where the wood combustion takes place and hot flue gas is produced. Some of the heat from the combustion chamber will be lost to the environment. The flue gas flows into the stove channel where heat is transferred to the top plate carrying the cooking pots. Finally, the flue gas flows via the chimney into the environment.

3.2 Geometry

The dimensions of the combustion chamber, stove and the chimney are represented in Table 2-1.

Table 3-1: Dimension of the cook stove parts in mm.

Dimensions	**Combustion chamber**	**Stove**	**Chimney**
Height (Z)	110	25	1320
Width (W)	160	438	/
Length (L)	100	550	/
Thickness of the walls (t)	15	6.35	5
Inner diameter (r_i)	/	/	50
Outer diameter (r_o)	/	/	50

Other variables that are used latter on in the computation can be expressed by using the previous dimensions and they are represented in Table 3-2:

Table 3-2: Equations for the dimension of the cook stove parts.

Variable	**Combustion chamber(cc)**	**Stove(st)**	**Chimney(ch)**
Cross Section (A)	$W_{cc} \cdot Z_{cc}$	$W_{st} \cdot Z_{st}$	${r_i}^2\pi$
Perimeter (O)	$2 \cdot (Z_{cc} + W_{cc})$	$2 \cdot (Z_{st} + W_{st})$	/
Hydraulic Diameter (D_h)	$\frac{4A_{cc}}{O_{cc}}$	$\frac{4A_{st}}{O_{st}}$	/
Volume of the walls (V)	/	$Z_{st}W_{st}L_{st}$	${r_i}^2 Z_{ch}$
Bottom face surface (A_{bottom})	$L_{cc} \cdot L_{cc}$	/	/
Total Wall Surface A_{tot}	/	$2 \cdot (Z_{st}W_{st} + Z_{st}L_{st} + W_{st}L_{st})$	${2r_i}^2\pi + 2r_i\pi Z_{ch}$
Inner wall surface A_{in}	/	/	$2\pi r_i Z_{ch}$
Outer wall surface A_{out}	/	/	$2\pi r_o Z_{ch}$

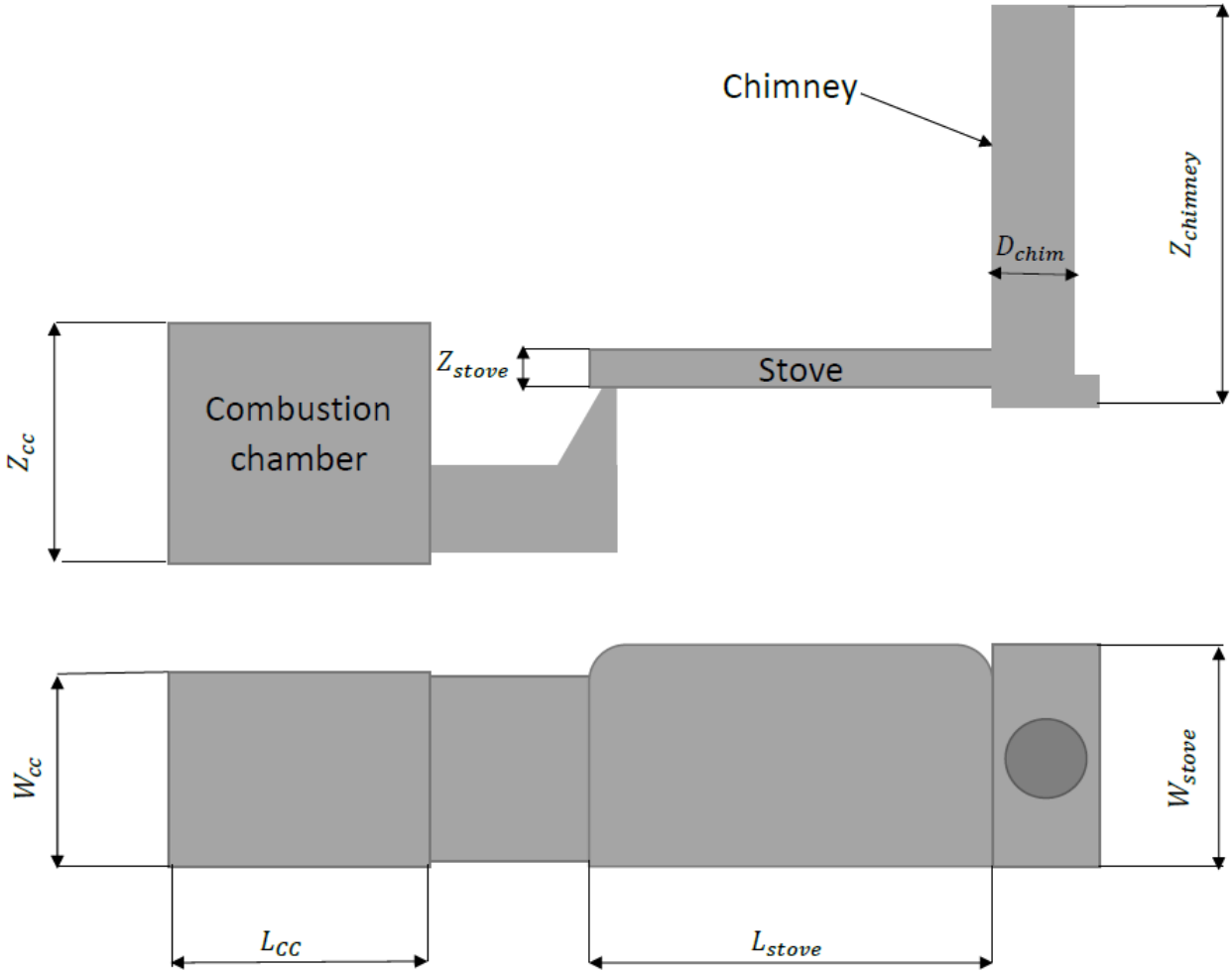

Figure 3-1: Sketch of the cook stove geometry

3.3 Operation variables

The external conditions and the required power are input variables for the algebraic model. They are listed in Table 3-3:

Table 3-3: Input variables.

Elevation above sea level [m]	750
Ambient temperature [K]	290
Cooking power [kW]	2-4

The elevation above sea level of the location where the cookstove is used is an important parameter because, together with ambient temperature, determines the air density. Here a reference altitude of 750 m is selected, and it was referred from [41]. Te ambient temperature is important as the environment acts as heat sink for the cookstove. Finally, the cooking power 2-4kW is a common range used for biomass cookstoves.

3.4 Gas properties

The air and flue gas properties are determined. Furthermore, the properties of the first one are a function of the elevation, while of the second are a function of the combustion temperature. Thus, their properties are defined with the following equations:

Ideal gas law applied to air:

$$\rho_{amb} = \frac{(P_{loc} \cdot MW_{air})}{(R_{univ} \cdot T_{amb})}; \tag{3-1}$$

Where ρ_{amb} is the air density and P_{loc} is the local barometric pressure which is a function of the elevation.

Empirical correlations for flue gas:

$$\nu = 0.000000123 \cdot (T - 273.15) + 0.000009571[46] \tag{3-2}$$

$$\rho = \frac{353}{T} \tag{3-3}$$

$$c_p = -5.35 \cdot 10^{-7} \cdot T^3 + 6.88 \cdot 10^{-4} \cdot T^2 + 2.75 \cdot 10^{-2} \cdot T + 1000[51] \tag{3-4}$$

$$k = 0.0244 + 0.6992 \cdot 10^{-4} \cdot (T - 273.15)[23] \tag{3-5}$$

Where ν is the kinematic viscosity, ρ is the flue gas density, c_p is the specific heat capacity and k the thermal conductivity.

3.5 Flow velocity

The flow field inside the cookstove is a buoyantly driven flow, which means that the flow field is induced due to the density difference between the flue gas and air, causing a hydrostatic pressure drop. Thus, assuming a uniform flue gas density, the theoretical velocity of the flue gas in the chimney is equal to:

$$V_{th} = \sqrt{2 \cdot g \cdot Z \cdot (\frac{\rho_{air}}{\rho_{flue}} - 1)} \tag{3-6}$$

The complete derivation of the theoretical velocity can be found in the Master Thesis of D.Q. Reyes (2020) [42].

In order to obtain a more realistic estimate of the losses inside the cookstove have to be taken into account. This is represent globally by the discharge coefficient depending on the losses due to the distributed heat addition and the viscous effects:

$$C_d = C_{heat} \cdot C_{viscous} \tag{3-7}$$

Where, C_{heat} is the coefficient of distributed heat addition and is estimated to be 0.95 [34], and $C_{viscous}$ is the coefficient of viscous loss and is equal to:

$$C_{viscous} = \frac{1}{\sqrt{1 + K_{overall}}} \tag{3-8}$$

where K_{overall} is the overall system loss coefficient depending on the losses in separate parts of the cookstove. Its derivation can be found in the A.3, Appendix A.

Knowing $K_{overall}$ the actual mass flow rate in the cookstove can be estimated (the mass can vary because more or less air can be entrained into the flue gas in the combustion chamber). Hence, it is computed in the following equation:

$$\begin{aligned} \dot{m}_{\text{total}} &= C_d \cdot V_{\text{th}} \cdot A_{\text{chimney}} \cdot \rho_g \\ &= \frac{A_{\text{chimney}} \cdot C_{\text{heat}} \cdot \rho_g \cdot \sqrt{2 \cdot g \cdot Z \cdot \left(\frac{\rho_a}{\rho_g} - 1\right)}}{\sqrt{1 + \sum K_{overall}}} \\ &= A_{\text{chimney}} \cdot C_{\text{heat}} \cdot \left(\frac{2 \cdot g \cdot Z \cdot \rho_g \cdot (\rho_a - \rho_g)}{1 + \sum K_{overall}}\right)^{0.5} \end{aligned} \tag{3-9}$$

where ρ_g denotes gas density. It should be noted that the mass flow rate is the result of the combined effect of the influence of both gas properties and pressure drop. Flue gas properties depend on fuel/air mixing, which depends on mass flow rate. Mass flow rate depends on combustion via the influence of density and temperature on flow and heat transfer. The

actual flow rate can be considered to be set by the pressure drop equation. The pressure drop in the chimney is considered in section 3.9

The mean flow velocity in different parts then also depends on the cross sectional area. The velocities in the combustion chamber and stove can are equal to:

$$V_{cc} = \frac{\dot{m_{total}}}{\rho_{amb} \cdot A_{cc}} \tag{3-10}$$

$$V_{st} = \frac{\dot{m_{total}}}{\rho_{flue} \cdot A_{st}} \tag{3-11}$$

In eq. 3-10 the air density is used in a large part of the combustion chamber the combustion is not yet complete and air is the main fluid component.

3.6 Non-dimensional groups

Non-dimensional numbers such as the Reynolds (Re), Nusselt (Nu) and Prandtl (Pr) number are computed because they are of essential importance for the heat transfer analysis. The Reynolds number is the ratio of the inertial and viscous forces, while Prandlt is the ratio of momentum diffusivity and thermal diffusivity. Furthermore, the Nusselt number $Nu$is a non-dimensional heat transfer coefficient. It has been expressed as a function of the Reynolds and Prandtl number for the stove and the chimney.

Pr is a fluid property, but it is temperature dependent. Its value in the chimney can be represented as a function of the average chimney temperature ($T_{\text{ch avg}}$) and this relation is used for both the stove and the chimney due to the small temperature variations between these two parts.

$$Pr = -7 \cdot 10^{-10} \cdot T_{\text{ch avg}}^3 + 1 \cdot 10^{-6} \cdot T_{\text{ch avg}}^2 - 0.0007 \cdot T_{\text{ch avg}} + 0.7809 \tag{3-12}$$

The Re and Nu of the stove and chimney are expressed by the following equations:

Stove

$$Re_{\text{stove}} = \frac{V_{\text{stove}} \cdot D_{\text{stove}}}{\nu_{flue}} \tag{3-13}$$

$$Nu_{\text{st}} = 9^2, Re_{st} < 3000 \tag{3-14}$$

$$Nu_{\text{st}} = 7.54 + \frac{0.03 \cdot \frac{Z_{\text{st}}}{L} \cdot Re_{\text{st}} \cdot Pr}{1 + 0.016 \cdot \left(\frac{Z_{\text{st}}}{L} \cdot Re_{\text{st}} \cdot P_r\right)^{\frac{2}{3}}}, \quad Re_{\text{st}} < 3000 \tag{3-15}$$

Chimney

$$Re_{\text{ch}} = \frac{V_{\text{ch}} \cdot D_{\text{ch}}}{\nu_{flue}} \tag{3-16}$$

$$Nu_{ch} = (\frac{F_{ch}}{8}) \cdot \frac{(Re_{ch} - 1000) \cdot Pr}{(1 + 12.7 \cdot (\frac{F_{ch}}{8}) \cdot Pr^{-0.66})}, Re_{ch} \geq 3000 \tag{3-17}$$

$$Nu_{ch} = 0.023 \cdot (Re_{ch}^{0.8} \cdot Pr^{0.4}), Re_{ch} < 3000 \tag{3-18}$$

3.7 Heat Transfer

Heat is transferred to the environment from the cookstove by convection, conduction and radiation. In the calculation of the heat transfer the influence of the cooking pot has not been described, in order to keep the model simple. First, the heat loss from the combustion chamber consists of contribution of convective/conductive heat transfer through the wall and radiative heat loss. The fraction of the firepower that is lost and not contributing to the final heat content of the flue has is called heat loss factor and is given by

$$\text{heat loss factor } = \frac{(Q_{\text{cond}} + Q_{\text{rad}})}{\cdot Q_{\text{firepower}}} \tag{3-19}$$

Where Q_{cond} and Q_{rad} are the heat losses from the combustion combustion chamber due to conduction and radiation. $Q_{firepower}$ is the firepower of the cookstove, and will be calculated below.

The heat loss from the stove and the chimney is expressed through the overall heat transfer coefficient U

$$Q = UA(T_{avg} - T_{ambient}) \tag{3-20}$$

where A is the heat transfer area, and T_{avg} is the average temperature in stove or chimney. The overall heat transfer coefficient for the stove and the chimney are given by

$$U_{stove} = \frac{1}{\frac{1}{h_{st}} + \frac{t_{st}}{k_{st}} + \frac{1}{h_o} + \frac{1}{h_{rad,st}}} \tag{3-21}$$

$$U_{chimney} = \frac{1}{\frac{1}{h_{ch}} + \frac{t_{ch}}{k_{ch}} + \frac{1}{h_o} + \frac{1}{h_{rad,ch}}} \tag{3-22}$$

Where, h_{st}, $h_{rad,st}$, k_{st} and h_{ch}, $h_{rad,ch}$, k_{ch} are the convective and radiative heat transfer coefficient and the wall thermal conductivity in the stove and the chimney, respectively. The variable t denotes the wall thickness. Furthermore, the convective and radiation heat transfer coefficients are expressed with the following equations:

$$h_{st} = \frac{Nu_{st} \cdot k_{flue}}{Z_{st}} \tag{3-23}$$

$$h_{ch} = \frac{Nu_{st} \cdot k_{flue}}{D_{ch}} \tag{3-24}$$

The radiative heat transfer coefficient is given by

$$h_{rad} = \sigma E(T_{avg}^2 - T_{amb}^2)(T_{avg} - T_{amb}) \tag{3-25}$$

where the emissivity of the flue gas is obtained from an empirical correlation:

$$\varepsilon = \exp(A_c + B_c) + \log 0.72\frac{V}{A} \tag{3-26}$$

V and A is the volume and the surface of each part separately. While, the coefficients A_c and B_c are a function of the average temperature, and are equal to:

$$A_c = 0.848 + 9.02 \cdot 10^{-4} T_{avg} \tag{3-27}$$
$$B_c = 0.9589 + 4.8 \cdot 10^{-6} T_{avg} \tag{3-28}$$

The formula for the radiation heat transfer coefficient is the same for both the stove and the chimney,but the average temperature, volume and surface area are different in each case.

3.8 Determination of the temperature

The temperatures of the stove and the chimney can be determined by using the conservation of energy equation and the physical properties of the gas. The heat balance and the thermodynamic relation between heat and temperature are given by

$$dQ = -U(T - T_{amb})\, dA \tag{3-29}$$
$$dQ = H dT \tag{3-30}$$

Here Q is heat transfer rate and H is heat transfer rate per unit temperature increase.

Then,

$$-U(T - T_{amb})\, dA = H dT \tag{3-31}$$

Where H is the transfer rate of heat supplied to the flue gas, per K temperature increase,

$$H = \dot{m}_{\text{total}} \cdot c_p \tag{3-32}$$

Using the method of separation of variables the temperature increase can be calculated:

$$\frac{U}{H}\int_0^A dA = \int_{T_{in}}^{T_{ambut}} \frac{dT}{(T - T_{amb}} \tag{3-33}$$

Integrating we obtain,

$$\frac{-UA}{H} = \ln \frac{(T_{\text{out}} - T_{amb})}{(T_{\text{in}} - T_{amb})} \tag{3-34}$$

Finally, the temperature increase in a part of the cookstove can be obtained. Now we consider three parts. For cookstove and chimney we obtain an inlet and an outlet temperature from

$$T_{\text{out}} = T_{\text{in}} + (T_{\text{in}} - T_{amb})\, e^{-\frac{UA}{H}} \tag{3-35}$$

For the combustion chamber we determine the final temperature from the firepower by including a possible the Heat Loss Factor 3-19. Other temperature changes are computed by using the solution of the heat balance equation eq. 3-35.Thus, the inlet and outlet temperatures for combustion chamber, stove and chimney are:

$$T_{\text{out cc}} = T_{amb} + \frac{(1 - \text{heat loss factor}) \cdot Q_{firepower}}{\dot{m}_{total} \cdot c_p} \tag{3-36}$$

$$T_{\text{in st}} = T_{\text{out cc}} \tag{3-37}$$

$$T_{\text{out st}} = T_{amb} + T_{\text{in st}} - T_a mb) \cdot e^{-(\frac{U_{st} A_{cooking}}{\dot{m}_{total} c_p})} \tag{3-38}$$

$$T_{\text{in ch}} = T_{\text{out st}} \tag{3-39}$$

$$T_{\text{out ch}} = T_{amb} + (T_{\text{in ch}} - T_{amb}) \cdot e^{-(\frac{U_{ch} A_{\text{ch inner wall}}}{\dot{m}_{act} c_p})} \tag{3-40}$$

3.9 Pressure drop

The pressure drop in the chimney is the main driving mechanism behind the flue gas flow in the cookstove. Furthermore, the draft is caused due to the density differences and the chimney height. Thus, the ideal pressure drop without any losses in the chimney follows is given by the difference in static pressure:

$$\Delta P_{\text{ideal}} = Z_{ch} \cdot g \cdot (\rho_{amb} - \rho_{flue}) \tag{3-41}$$

However, when the viscous losses in the chimney are included then we obtain the actual pressure drop which is can be obtained from the following equation:

$$\begin{aligned} \Delta P_{\text{real}} &= \Delta P_{\text{ideal}} + \Delta P_{\text{loss}} \\ &= Z_{ch} \cdot g \cdot (\rho_{amb} - \rho_{flue}) - \frac{K_{ch} \cdot \rho_{flue} \cdot v_{\text{ch}}^2}{2} \end{aligned} \tag{3-42}$$

Where K_{ch} is the loss coefficient within the chimney.

3.10 Results and discussion

The model developed in this chapter concerns a Plancha cookstove. It was selected because the long chimney provides opportunity to install a turbulent agglomerator of the type discussed in Chapter 2 and suppress emissions of small particles. The results of the model provide mass flow rate and temperature and hence velocity at the entrance of the chimney. This can used as inlet boundary conditions of the chimney / turbulent agglomerator. It should be noted however that the presence of obstacles in the flow as used in the turbulent agglomerator will result in an increase in frictional loss and apart from the functionality of the agglomerator in particle agglomeration, also its influence on the achieved mass flow rate should be taken into consideration in design of the agglomerator and the present model can be extended to do so. This has not been included in our study. We have taken representative properties of a calculation without the agglomerator to find representative inlet boundary conditions for agglomerator simulations.

The results are shown in model in Figures 3-2.-3-6. As independent parameter is used the cooking power, the heat released by combustion. The final temperature depends on both heat released and total mass flow rate. The higher temperature, the lower the density of the flue gas will get lower, which can be seen in Figure 3-3., and the gas will become lighter, resulting in stronger buoyancy effects. Therefore, the buoyancy force will accelerate the flue and the velocity will increase, which can be observed from Figure 3-2. But this higher velocity will also lead to higher pressure drop, preventing unlimited increase of velocity.

Furthermore, the overall heat transfer coefficient will also change depending on temperature and flow velocity. Increase of both temperate and heat transfer coefficient at increasing firepower can be seen in Figure 3-4 and Figure 3-6.

The representative values of velocity and the inlet temperature of the chimney taken into account for assembling the boundary conditions in the CFD simulation of the agglomerator, are given in Table 3-4.

An extension of the model including the effects of the turbulent agglomerator would be of interest for final design.

Table 3-4: Mean values of the cook stove estimations.

Velocity	0.9	$\frac{m}{s}$
Temperature	405	K

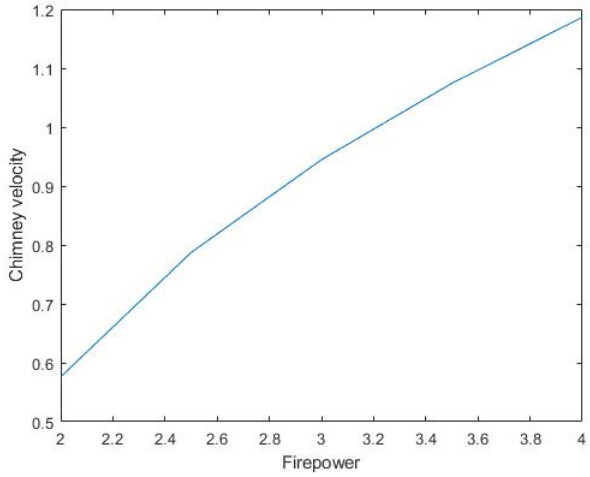

Figure 3-2: Average flue gas chimney speed.

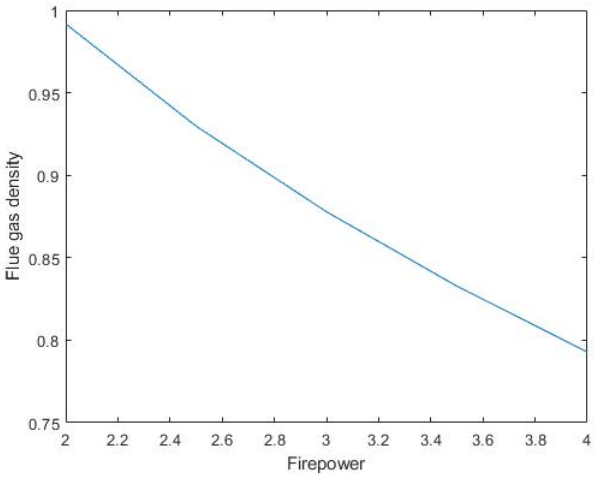

Figure 3-3: Flue gas density.

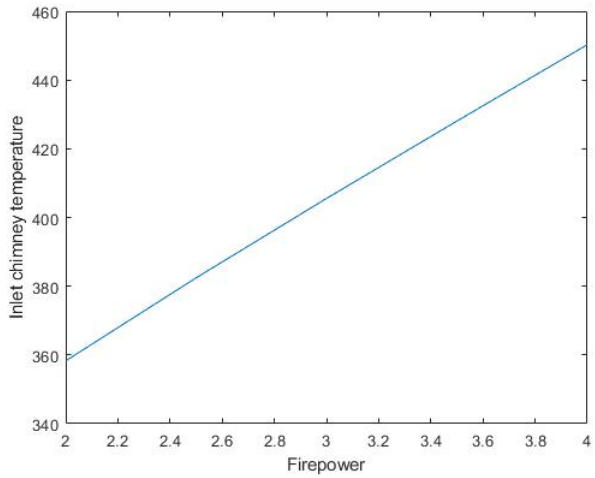

Figure 3-4: Inlet chimney temperature.

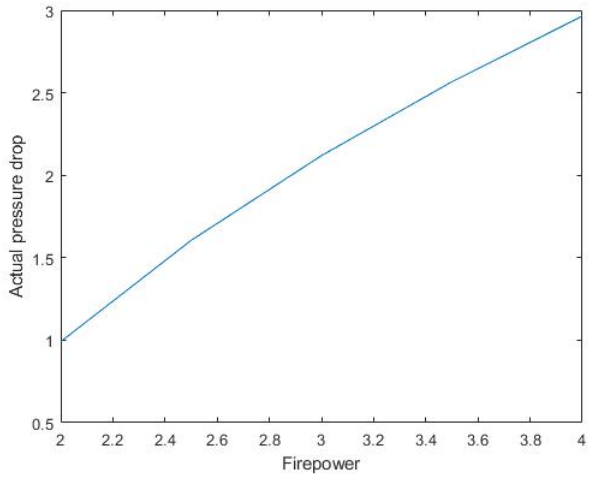

Figure 3-5: Actual pressure drop in the chimney.

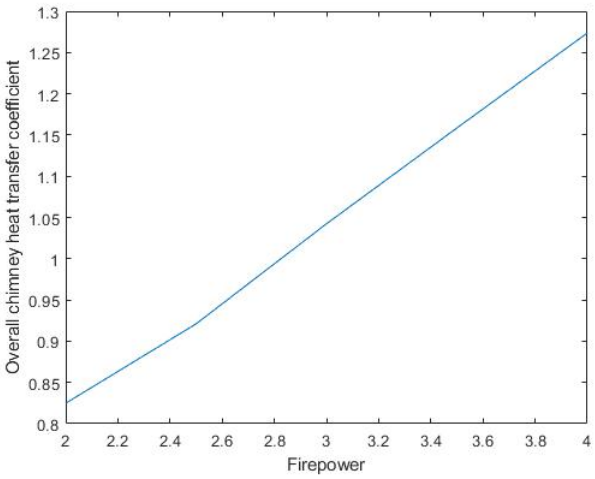

Figure 3-6: Overall cookstove heat transfer coefficient.

Chapter 4

Modelling of dispersed multiphase flow

4.1 Introduction

In order to describe the flow of flue gas containing particles theoretical models are needed for the description of 'dispersed multiphase flow'. In this chapter the models we have used are described and the modeling options are discussed. Both the Eulerian Lagrangian (EL) approach and the Eulerian-Eulerian (EE) approach are discussed. The EE approach is combined with the sectional method for solution of the particle size distribution (PSD).

In the EL method the gaseous phase is described as a continuum and the particle phase as a set of discrete entities with position, velocity and properties evolving in time. The most important property in this work is the particle diameter. The EL approach allows determination of the trajectories followed by small and large particles. In order to describe a turbulent agglomerator the influence of collisions between particles would have to be included. The EE approach describes the gas phase and the particle phase as interpenetrating continua. In order to include particle size as independent parameter in the EE approach, each size class is represented by a different continuum. In general the particle size can be described by the particle size distribution (PSD). An equation for the PSD can be derived, describing all processes modifying the size distribution: creation, agglomeration, breakage, growth, etc. but also transport in physical space by convection and diffusion. Dividing the particle size range in subintervals, the mass in each subinterval is considered a different continuum. Particle agglomeration then becomes a transfer process between the subintervals of the PSD. The subintervals are also called sections and a solution method describing mass transfer between sections is called 'sectional method'. Integration of the sectional method in the EE approach is possible by associating each section with a different continuum. To make this operational the volume fraction of each continuum must be determined and also its velocity and turbulence properties.

4.2 Eulerian-Lagrangian method

4.2.1 Laminar equations

The flow field of the continuous phase is described using the Eulerian approach [[57]]. We consider the case with only momentum transfer between the phases and no mass or heat transfer. Quantities such as the velocity, temperature then can be obtained from the governing equations.

Continuity:

$$\frac{\partial \rho}{\partial t} + \frac{\partial}{\partial x_i}(\rho u_i) = 0 \tag{4-1}$$

Momentum:

$$\frac{\partial}{\partial t}(\rho u_i) + \frac{\partial}{\partial x_i}(\rho u_i u_j) = -\frac{\partial p}{\partial x_i} + \frac{\partial \tau_{ij}}{\partial x_i} + \rho g_i + F_i \tag{4-2}$$

Energy:

$$\frac{\partial(\rho T)}{\partial t} + \mathrm{div}(\rho u T) = \mathrm{div}\left(\frac{\lambda}{c_p}\,\mathrm{grad}\, T\right) + S_T \tag{4-3}$$

Where ρ is the density; u_i is the axial velocity; p is the pressure; τ_{ij} is the stress tensor; g_i is the gravity force; F_i is the external volume force in the i direction; T is the temperature, λ is the thermal conductivity of the fluid, c_p is the specific heat capacity; S_T is the viscous dissipation term [57].

4.2.2 Turbulence model

In order to describe a turbulent flow the laminar transport equations are averaged. The resulting equations are unclosed because they contain unknown correlations. To solve this closure problem model assumptions are made for correlations between velocity fluctuations (Reynolds stress) and for correlations between velocity and temperature. In the 'two-equation models' this involves adding extra equations for turbulent kinetic energy k

$$k = \tfrac{1}{2} u_i' u_i' \tag{4-4}$$

and turbulent energy dissipation rate ϵ. The variable u_i' denotes the difference between instantaneous and mean value of the i-th component of the velocity. Together they determine the turbulent viscosity, describing the diffusive effect of turbulent mixing, given by:

$$\mu_t = C_\mu \bar{\rho} \frac{k^2}{\epsilon} \tag{4-5}$$

The transport equations for k and ϵ are of the following general form:

$$\frac{\partial}{\partial t}(\rho k) + \frac{\partial}{\partial x_i}(\rho k u_i) = \frac{\partial}{\partial x_j}\left(\alpha_k \mu_{eff} \frac{\partial k}{\partial x_j}\right) + G_k + G_b - \rho\varepsilon - Y_M \tag{4-6}$$

$$\frac{\partial}{\partial t}(\rho \varepsilon) + \frac{\partial}{\partial x_i}(\rho \varepsilon u_i) = \frac{\partial}{\partial x_j}\left(\alpha_\epsilon \mu_{eff} \frac{\partial \varepsilon}{\partial x_j}\right) + C_{1\varepsilon}\frac{\varepsilon}{k}(G_k + C_{3\varepsilon}G_b) - C_{2\varepsilon}\rho\frac{\varepsilon^2}{k} \tag{4-7}$$

Here $\mathbf{G_k}$ represents the generation of turbulence kinetic energy due to the mean velocity gradients; $\mathbf{G_b}$ is the generation of turbulence kinetic energy due to buoyancy; $\mathbf{Y_M}$ represents the contribution of the fluctuating dilatation in compressible turbulence to the overall dissipation rate; $\mathbf{C_{1\epsilon}}$, $\mathbf{C_{2\epsilon}}$, $\mathbf{C_{3\epsilon}}$ are constants; $\mu_{\mathbf{eff}}$ is the effective viscosity (sum of laminar and turbulent viscosity); $\alpha_{\mathbf{k}}$ and α_ϵ are the inverse Prandtl numbers for $\mathbf{k}$ and ϵ; The standard values of the model constants are $C_\mu = 0.09$, $C_{\epsilon_1} = 1.44$, $C_{\epsilon_2} = 1.92$, $\alpha_k = 1.00$, $\alpha_\epsilon = 1/1.30$.
In this work we shall use the standard k-ϵ turbulence model with standard wall functions for the particle agglomeration, and the RNG k-ϵ for the particle tracking because it has already been proven successful in the work of Sun et al. (2019), who studied the turbulent agglomerator with the EL approach [57]. The advantage of the RNG model is that it can accurately describe flow with streamline curvature [5]. In the turbulent agglomerator this type of flow is present due to the configuration of the vortex sheets.

4.2.3 Discrete Phase Model

The particle acceleration is given by Newtons second law of motion, and have the general form [57]:

$$m_p \frac{dv_p}{dt} = F_{\text{drag}} + F_{\text{pres}} + F_{\text{vir.mass}} + F_{\text{gravity}} \tag{4-8}$$

where,

$$F_{\text{drag}} = \frac{3}{4} m_p \frac{\rho_g C_D}{\rho_p d_p} \|v_g - v_p\| \tag{4-9}$$

$$F_{\text{pres}} = -\frac{m_p}{\rho_p}\nabla P \tag{4-10}$$

$$F_{\text{vir mass}} = \frac{m_p \rho_g d(v_g - v_p)}{2\rho_p \quad dt} \tag{4-11}$$

$$F_{\text{gravity}} = m_p \frac{\rho_p - \rho_g}{\rho_p}\vec{g} \tag{4-12}$$

$$\tag{4-13}$$

and,

$$C_D = \begin{cases} 24\left(1 + 0.15\text{Re}^{0.687}\right)/\text{Re} & \text{Re} \leq 1000 \\ 0.44 & \text{Re} > 1000 \end{cases} \tag{4-14}$$

$$R_{pq} = \frac{\alpha_q \alpha_p \rho_p f}{\tau_p} \tag{4-15}$$

where,

$$f = \frac{C_D \cdot R_e}{24} \tag{4-16}$$

Where m_p and d_p are the the mass and diameter of the particle, F_{drag} is the drag force, F_{pres} the pressure gradient force, $F_{\text{vir mass}}$ is the virtual mass force and F_{gravity} is the gravity force. Furthermore, ρ_p and ρ_g are the density of the particle and gas phase, respectively. v_p and v_g are the velocity of the particle and the gas phase. Furthermore, $\mathrm{C_D}$ is the Schiller and Naumann drag coefficient, $\mathrm{R_{pq}}$ is the momentum exchange coefficient between the two phases and f is the drag function. In the present work only the drag force and gravity are important. Sun et al. (2019) [57] have reported on the trajectories and the concentration fields of particles deduced using the Lagrangian equations. Describing particle agglomeration in the Lagrangian framework would require formulation of collision and agglomeration models. This is not explored further here but instead an Eulerian method is used to describe the behavior of the particle phase, as described next.

4.3 Eulerian-Eulerian method

In the EE method the evolution of both the gas phase and the particle phase are described by Eulerian equations. In case of multiple particle size classes Eulerian equations are associated with each size class. In general one has to consider transport equations for mass, momentum and energy. The mass density associated with a particle class is the product of the intrinsic particle density and the volume fraction it occupies.

4.3.1 Multi-fluid model

When all particles together are considered to form one phase the model corresponds to the Eulerian two-fluid model, considering gas and particles represented as two interpenetrating fluids. When different size classes of particles are considered to form a different flow, a multifluid model is obtained with one gas phase and a number of particle phases. It was used for simulating the particle agglomeration in Ref. [38]. The continuity and momentum equations are computed for each phase separately. For a turbulent flow, the equations are considered to be Reynolds averaged equations. The different phase are labeled using an index p, taking values between 1 and N. Considering any of the phases with index value q, the volume fraction occupied by a phase with index q is denoted α_q. The transport equations for this phase are given by:
The continuity equation:

$$\frac{\partial}{\partial t}\left(\alpha_q \rho_q\right) + \nabla \cdot \left(\alpha_q \rho_q \vec{v}_q\right) = \sum_{p=1}^{N} \left(\dot{m}_{\mathrm{pq}} - \dot{m}_{\mathrm{qp}}\right) + S_q \tag{4-17}$$

Where $\tilde{\mathbf{v}}_{\mathbf{q}}$ is the velocity of the phase $\mathbf{q}$, $\dot{\mathbf{m}}_{\mathrm{pq}}$ is the mass transfer rate from phase $\mathbf{p}$ to phase $\mathbf{q}$ and $\dot{\mathbf{m}}_{\mathrm{pq}}$ from phase $\mathbf{q}$ to phase $\mathbf{p}$. In our case considering only agglomeration there is only

mass transfer between particle phases and in the direction from sections with small particles to sections with large particles.

When the multifluid model is used in combination with the population balance model for the particle size evolution, the volume fractions α_q of particle size classes follow from the solution of the population balance equation in combination with information for the total particle phase volume fraction.

The momentum equation:

$$\frac{\partial}{\partial t}\left(\alpha_q \rho_q \vec{v}_q\right) + \nabla \cdot \left(\alpha_q \rho_q \vec{v}_q \vec{v}_q\right) = -\alpha_q \nabla p + \nabla \cdot \bar{\bar{\tau}}_q + \alpha_q \rho_q \vec{g} + \sum_{p=1}^{N} \left(\vec{R}_{pq} + \dot{m}_{pq}\vec{v}_{pq} - \dot{m}_{qp}\vec{v}_{qp}\right) \tag{4-18}$$

Where $\bar{\bar{\tau}}_q$ is the phase stress tensor of the phase **q**. It is of the general form:

$$\bar{\bar{\tau}}_q = \alpha_q \mu_q \left(\nabla \vec{v}_q + \nabla \vec{v}_q^T\right) + \alpha_q \left(\lambda_q - \frac{2}{3}\mu_q\right) \nabla \cdot \vec{v}_q \bar{\bar{I}} \tag{4-19}$$

In the left hand side of the momentum equation are present the transient and the convective term. In the right hand side are the pressure gradient force the stress term and the gravity term followed by terms related to momentum transfer between the phases. $\mu_{\mathbf{q}}$ and $\lambda_{\mathbf{p}}$ are the shear and bulk viscosity of the **q** phase. $\tilde{\mathbf{R}}_{\mathbf{pq}}$ is the momentum exchange between phases caused by slip between the phases [5]. The momentum transfer due to mass transfer is the product of the mass transfer rate and the difference in velocity between two phases denoted $\vec{v}_{pq}$.

4.3.2 Standard k-ϵ

For our two test cases, where particle agglomeration was simulated, we have used the Standard k-ϵ per phase turbulence model with standard and enhanced wall equations near the walls. Using this model the kinetic energy and the turbulence dissipation rate are computed for gas and solid part of the flow separately and in case of particles divided in classes according diameter range, for each range separately. The wall functions describe the profiles of turbulence close to the walls. [5]. The Standard turbulence model has been used earlier for describing particle agglomeration in a turbulent agglomerator in Ref. [38]. the Realizable k-ϵ model has also been used for simulating particle agglomeration, however in the Lagrangian framework [19].

In the case of the multifluid EE approach, the following turbulence transport equations apply: The k-equations:

$$\frac{\partial}{\partial t}\left(\alpha_q \rho_q k_q\right) + \nabla \cdot \left(\alpha_q \rho_q \vec{U}_q k_q\right) = \nabla \cdot \left(\alpha_q \left(\mu_q + \frac{\mu_{t,q}}{\sigma_k}\right) \nabla k_q\right) + \left(\alpha_q G_{k,q} - \alpha_q \rho_q \epsilon_q\right) + \sum_{l=1}^{N} K_{lq}\left(C_{lq}k_l - C_{ql}k_q\right) - \sum_{l=1}^{N} K_{lq}\left(\vec{U}_l - \vec{U}_q\right) \cdot \frac{\mu_{t,l}}{\alpha_l \sigma_l} \nabla \alpha_l + \sum_{l=1}^{N} K_{lq}\left(\vec{U}_l - \vec{U}_q\right) \cdot \frac{\mu_{t,q}}{\alpha_q \sigma_q} \nabla \alpha_q \tag{4-20}$$

The ϵ-equations:

$$\frac{\partial}{\partial t}\left(\alpha_q \rho_q \epsilon_q\right) + \nabla \cdot \left(\alpha_q \rho_q \vec{U}_q \epsilon_q\right) = \nabla \cdot \left(\alpha_q \frac{\mu_{t,q}}{\sigma_\epsilon} \nabla \epsilon_q\right) + \frac{\epsilon_q}{k_q}\left[C_{1\epsilon}\alpha_q G_{k,q} - C_{2\epsilon}\alpha_q \rho_q \epsilon_q + \right. \tag{4-21}$$

$$\left. C_{3\epsilon}\left(\sum_{l=1}^{N} K_{lq}\left(C_{lq}k_l - C_{ql}k_q\right) - \sum_{l=1}^{N} K_{lq}\left(\vec{U}_l - \vec{U}_q\right) \cdot \frac{\mu_{t,l}}{\alpha_l \sigma_l}\nabla\alpha_l + \sum_{l=1}^{N} K_{lq}\left(\vec{U}_l - \vec{U}_q\right) \cdot \frac{\mu_{t,q}}{\alpha_q \sigma_q}\nabla\alpha_q\right)\right]$$

Where,

$$C_{lq} = 2, C_{ql} = 2\left(\frac{\eta_{lq}}{1+\eta_{lq}}\right) \tag{4-22}$$

and,

$$\eta_{pq} = \frac{\tau_{t,pq}}{\tau_{F,pq}} \tag{4-23}$$

These equations describe the turbulence properties of phase $\mathbf{q}$ including interactions with all phases $\mathbf{l} = 1, ..., N$; $\sigma_{\mathbf{k}}$ and $\sigma_{\mathcal{E}}$ are the Turbulent Prandtl numbers for $\mathbf{k}$ and $\mathcal{E}$. $\tilde{\mathbf{U}}_{\mathbf{l}}$ and $\tilde{\mathbf{U}}_{\mathbf{p}}$ are the phase weighted velocities; $\mathbf{K_{pq}}$ is the exchange coefficient and $\mu_{\mathbf{t}}$ is the turbulent viscosity; $\tau_{\mathbf{t,pg}}$ is the Lagrangian integral time scale and $\tau_{\mathbf{F,pg}}$ is the characteristic particle relaxation time.

There are two types of interaction terms between the phases, appearing in the three summations in the k and equations: the first sum describes the effect of difference in turbulence level between the phases, the second and third sum describe the effects of turbulent mixing (turbulent viscosity) in combination with difference in velocity between the phase and gradient in volume fraction. All these terms simplify considerable in the special case when the different size classes have the same velocity, as assumed in the 'homogeneous model' used to describe the convection of the particle size distribution (see below).

4.4 Population balance model

In this part the population balance model for describing the particle phase properties is explained. Furthermore, the solution methods which are applied for solving the population balance equation are briefly discussed.

4.4.1 The Number Density Function

For a statistical description of a population of polydisperse particles the particle state vector is needed [44]. It depends on the external coordinates $\vec{x}$ which describe the particle position in space, and the internal coordinates ϕ which represent the size, composition and temperature of the particles [4]. The number density function can is state vector describing the distribution of particles in position space and in composition space and in time. It is denoted by $n(\vec{x}, \phi, t)$ and denotes the number density of particles (particles per unit volume in space and per unit of the particle property considered) at a given time.

4.5 Population Balance Equation

The Population Balance Equation (PBE) is the transport equation for the number density. It described the effects of the different phenomena affecting its value. In case of particles in a flow a cloud of particles is convected and influenced by diffusion phenomena and simultaneously processes physical describing interaction between particles result in local changes in the number density. To describe convection information on the flow is needed and this explains why an equation for the number density has to be combined with an equation for the flow. Here this is done by coupling it with the EE equations for disperse multiphase flow. This method has been frequently used in the literature as it requires less computational effort than Lagrangian particle tracking.

We now consider a number density for the case that the composition is defined by the volume V and is denoted as $n(V,t)$ (suppressing the dependence on position in space). Phenomena such as particle nucleation, growth, aggregation and breakage are described in the PBE. Because of forces between particles and turbulent motion of the flow field particles some particles may collide, fuse and grow, thus forming larger particles. However, particles can also break and form smaller particles.Therefore, we have birth and death terms linked to the particle aggregation and breakage.The population balance equation is of the following general form:

$$\begin{aligned}\frac{\partial}{\partial t}[n(V,t)] + \nabla\cdot[\vec{u}n(V,t)] + &\underbrace{\nabla_v\cdot[G_v n(V,t)]}_{\text{Growth term}} \\ &= \underbrace{\frac{1}{2}\int_0^V a\left(V-V',V'\right)n\left(V-V',t\right)n\left(V',t\right)dV'}_{\text{Birth due to Aggregation}} \\ &- \underbrace{\int_0^\infty a\left(V,V'\right)n(V,t)n\left(V',t\right)dV'}_{\text{Death due to Aggregation}} \\ &+ \underbrace{\int_{\Omega_v} pg\left(V'\right)\beta\left(V\mid V'\right)n\left(V',t\right)dV'}_{\text{Birth due to Breakage}} \\ &- \underbrace{g(V)n(V,t)}_{\text{Death due to Breakage}}\end{aligned} \tag{4-24}$$

The terms on the left hand side are the transient term and the convection term (momentum flux). The terms on the right describe the effects of different physical processes influencing the particle volume. Growth G_v of particles leads to a change in particle volume and shifts the size distribution along the volume coordinate. The aggregation kernel α characterises 'birth' and 'death' of particles due to aggregation has the mean of a probability density for aggregation processes. It has to be integrated over all possible combinations, with $V - V'$ being the volume of particles which aggregate with particle of volume V' to form particles of volume V [4]. Similarly breakage is described by a probability density. In this work only aggregation is considered.

The precise form of the aggregation kernel depends on the application: the material properties of particles and fluid, the thermodynamic state (temperature) and the flow properties (laminar or turbulent).
The aggregation of the smallest particles (smaller than 1 μm) is dominated by the effect of Brownian motion, driven by molecular motions of the fluid. Larger particles are aggregating due to flow effects. Aggregation of larger particles is mainly caused by flow effects. In turbulent flow a distinction can be made between effects of the smallest eddies (in the size of the Kolmogorov length) and larger eddies (in the inertial range of turbulence). These turbulent length scales have to be compared with the diameter of the particles in order to judge with aggregation kernel is dominant [4] [49]. This is elaborated in the next sections.

4.5.1 Free molecular aggregation kernel

The free molecular aggregation kernel is used when most particles are smaller than $1\mu m$ [4] [49]. In this size range particles mostly collide due to Brownian motion. The aggregation kernel which was proposed by Otto et al (1999) [54] is equal to:

$$a\left(L_i, L_j\right) = \frac{2k_B T}{3\mu} \frac{\left(L_i + L_j\right)^2}{L_i L_j} \tag{4-25}$$

Where k_B is the Boltzmann constant, T is the absolute temperature of the fluid and μ is the dynamic viscosity of the fluid.

4.5.2 Turbulent aggregation kernel

During the flow of the flue gas through the agglomerator turbulence is being created near the wall and at the obstacles (the vortex sheets). The turbulence is characterised by a range of eddy size from the largest scale where the turbulence is generated to the smallest scales where the turbulence is dissipated [4]. Which agglomeration process is dominant (and which agglomeration kernel is to be used) depends on the relative size of particles compared the range of smallest eddies in the flow carrying the particles, which is the Kolmogorov length scale given by:

$$\eta = \left(\frac{\nu^3}{\varepsilon}\right)^{1/4} \tag{4-26}$$

Here ν is the kinematic viscosity (material property) and ϵ is the turbulent dissipation rate (flow property) of the fluid (the flue gas).
If both particles that are colliding are smaller than η then aggregation will occur due to the viscous subrange mechanism. Due to their low inertia, such small particles follow the flow and can be assumed to have the same velocity. They are brought together by the local velocity gradient, characterised by the dissipation rate and the viscosity. The kernel from Saftman

and Turner (1956) is then used [39]:

$$a\left(L_i, L_j\right) = \varsigma_T \sqrt{\frac{8\pi}{15}} \dot{\gamma} \frac{\left(L_i + L_j\right)^3}{8} \tag{4-27}$$

Where L_i and L_i are diameters of colliding particles **i** and **j**. ς is the collision coefficient (capture efficiency of the collision, see [4] for details) and $\dot{\gamma}$ is the shear rate at the Kolmogorov scale.

$$\dot{\gamma} = \left(\frac{\epsilon}{\nu}\right)^{0.5} \tag{4-28}$$

If both particles are bigger than η, then the aggregation is happening due to the inertial subrange mechanism. This means that particles will have independent velocities before the collision. Thus, the kernel from Abrahamson et al (1975) is applied [29]:

$$a\left(L_i, L_j\right) = \varsigma_T 2^{3/2} \sqrt{\pi} \frac{\left(L_i + L_j\right)^2}{4} \sqrt{\left(U_i^2 + U_j^2\right)} \tag{4-29}$$

Where, U^2 is the mean squared particle velocity.

Otherwise,if only one of the particles is larger than the Kolmogorov scale, the aggregation kernel is taken as the one proposed by Haibo et al (2005) [53]:

$$\beta_t\left(S_t < 1\right) = \left(L_i + Lj\right)^3 \sqrt{\frac{8\pi}{15} \frac{\varepsilon}{v}} \cdot c_0 \left(\frac{\eta}{\left(L_i + Lj\right)}\right)^{0.08 + 0.897 S_t} \tag{4-30}$$

Where ε is the turbulent dissipation rate, ν is the kinematic viscosity and S_T is the Stokes number.

4.5.3 PBE solution method

Several methods exist for solving the PBE. Two types of methods are available in Fluent, sectional methods and variants of the method of moments.

1. Sectional method
    - Homogeneous
    - Inhomogeneous
2. Method of Moments
    - Standard Method of Moments
    - Quadrature Method of Moments

- The Direct Quadrature Method of Moments

In the sectional method the size range is subdivided in a finite set of subranges and the the continuous number density is approximated by a discrete histogram, as shown in Figure 4-1. The integrals in the PBE are replaced by summations.

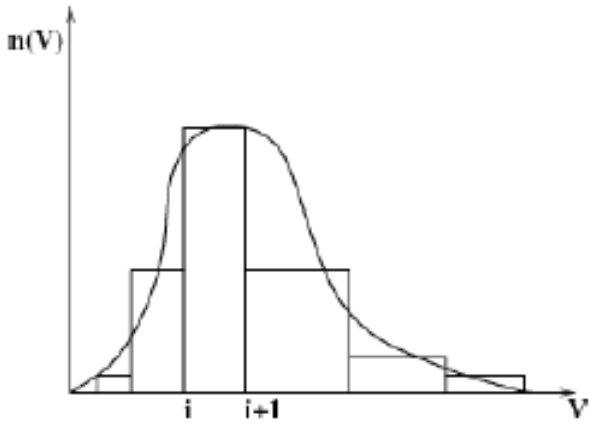

Figure 4-1: A Particle Size Distribution (PSD) as Represented by the Discrete Method.

On the other hand, in the method of moments, only a small subset of the moments of the distributed are solved for and the PBE is related to this finite number of moments by closure assumptions.

The sectional method can easily be combined with the EE multifluid model in the sense that the particles in a size class are assumed to form one fluid of the EE model. However, the computational cost is larger than that of the method of moments.
When the discrete number density is known then the volume occupied by the particles in a size range is known (particle density is assumed constant). In any region of space the volume not taken by particles then is taken by the gas and the volume fractions needed in the EE approach are known.

But to solve the EE equations also the velocity of a particle class must be solved for. Obtaining the solution of the velocity fields of all subranges takes a lot of computational time can lead to convergence problems. A lot of simplification occurs when it is assumed that the fluids representing all particle size classes move with the same velocity. This is called the 'homogeneous section method'. In this method only one momentum equation for the dispersed phase is solved. It is suitable when the total size range of particles is not very wide, so that they all have similar Stokes number and follow the flow in similar way. In the application to agglomeration of particles in flue gas the assumption of equal velocity does not seem to be suitable because the different velocity of small and large particles, bringing them in different parts of the domain is an important phenomenon. Nevertheless even in the homogeneous model the particle agglomeration process can proceed at different rates in different regions of space depending on the local flow properties and agglomeration effects can be quantified. Therefore the homogeneous model and inhomogeneous model will be applied in subsequent steps of the investigation.

To solve the PBE and the EE equations boundary conditions have to be specified. At the inlet the volume fractions of particle classes are defined. On the one hand there are the volume fractions of the particle size classes as fraction of the volume occupied by particles. On the other hand there is the volume fraction of solid particles in the solid-gas mixture. Based on temperature and temperature then the gas density and the mixture density can be obtained.

Chapter 5

Turbulent agglomerator with additional air injection

5.1 Introduction

The objective of this chapter is to test the proposed model of Euler-Euler turbulence model in combination with the sectional method for the population balance equation using a simple test case.

The studied geometry functions as turbulent agglomerator using obstacles in the flow, but in addition uses a high velocity air jet to induce additional turbulence and Experiments have been performed on this geometry and the conclusion has been made that by the air jet the agglomeration efficiency will increase [18]. The jet velocity can play an important part as by increasing it the removal removal efficiency will gradually increase [18]. A similar result was obtained in the work J.Li et al (2017) [26], where a square agglomeration chamber without internal vortex sheets was used.

In Computational Fluid Dynamics (CFD) applications for engineering design it is important to consider various test cases of increasing complexity. Two-dimensional (2D) simulations can already reveal essential trends. Such study was carried out for multiple cases to chose the configuration of the vortex sheets in turbulent agglomerator to obtain the best removal efficiency [38].

Next more realistic three dimensional simulations should be made (see next chapter). Further more, higher accuracy can be expected from Large Eddy Simulation (LES), in stead of Reynolds Averaged Navier-Stokes simulations (RANS). Usually, RANS is used for modeling of industrial engineering problems, as it requires less computational time [38]. However, LES is also applied. Turbulence in a 3D square turbulent agglomerator was simulated by using Large Eddy Simulation in [26]. This resulted in a higher computational cost, but the results regarding the agglomeration can be expected to be more accurate as the turbulent motions are resolved above a limiting scale. In particular this also applies to the turbulent motions of the discrete phase. One of the important findings of [26] is that as the jet inlet velocity

is increased so is the agglomeration efficiency , which agrees with the idea elaborated in [18]. In this chapter we report on numerical simulations related to the setup studied in [38].

5.2 Experimental setup

The turbulent agglomerator considerd in [38] is a vertical circular pipe with 1000mm length and an inner diameter of 50 mm with inflow at the top and outflow at the bottom. In the side wall of the cylinder there is a small round jet nozzle of 2mm diameter which is located 150 mm below the inlet. A set of square vanes of dimension 15mm $\times$ 15mm was installed in equidistant positions along the centerline of the pipe. The spacing and angle of inclination of the vanes has been varied but the case of spacing 100 mm and inclination $30°C$ was found to be about optimal giving the highest agglomeration efficiency and will be studied here. Figure 5-1 provides a sketch of the configuration. The flue gas enters from above at a velocity of 0.8 ms^{-1}, while at the jet inlet air enters through a cylindrical inlet at the side with a velocity of 22 ms^{-1} [38].

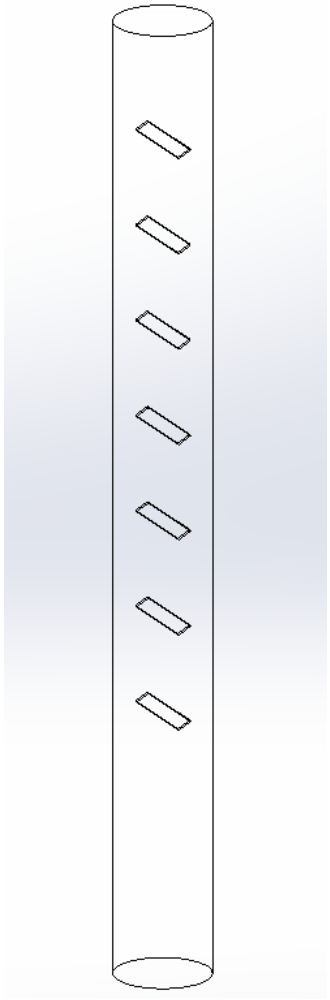

Figure 5-1: Sketch of the agglomeration chamber [38].

5.3 CFD setup

The simulation was done using the Euler-Euler method with the homogeneous approach for the section method to obtain the particle size distribution. The commercial software ANSYS Fluent 2019 R3 was used. The setup of the CFD problem used a rectangular 2D domain. This is a poor representation of the cylindrical pipe and this will have to be taken into account in the interpretation of the results. The dimensions and the model of the computational domain are shown in Table 5-4. and Figure 5-2, respectively.

Table 5-1: Geometry of the computational domain

Dimension	Value
Pipe diameter	50 mm
Jet nozzle diameter	2 mm
Length	1000 mm
Vane angle	30°
Vane edge length	15 mm

The computational domain was meshed ANSYS Workbench 2019 meshing tool. Structured mesh was applied near the walls and the rest of the domain, while around the vortex sheets refined semi-structured mesh is applied to precisely capture the vortex shedding. Structured and semi-structured mesh can be seen on Figure 5-3. Afterwards, the mesh statistics and quality were assessed and represented in Table 5-2 and Table 5-3. The values of the parameters are in good agreements with the ANSYS recommendations where it is advised for the aspect ratio to be less than 3, orthogonal quality to be above 0.1 and the skewness to be in range of -0.5-0.5.

Table 5-2: Mesh characteristics

Dimension	Value
Elements	96363
Nodes	292179

Table 5-3: Mesh quality

Dimension	Value
Average skewness	0.07149
Average aspect ratio	1.0808
Average orthogonal quality	0.98489

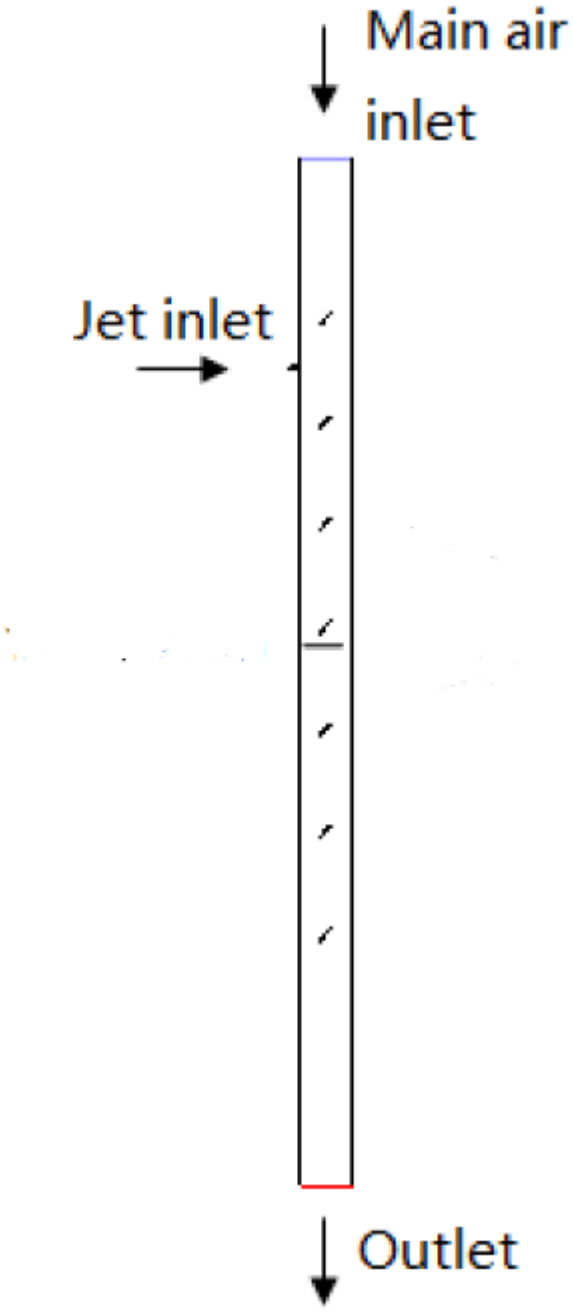

Figure 5-2: Computational domain.

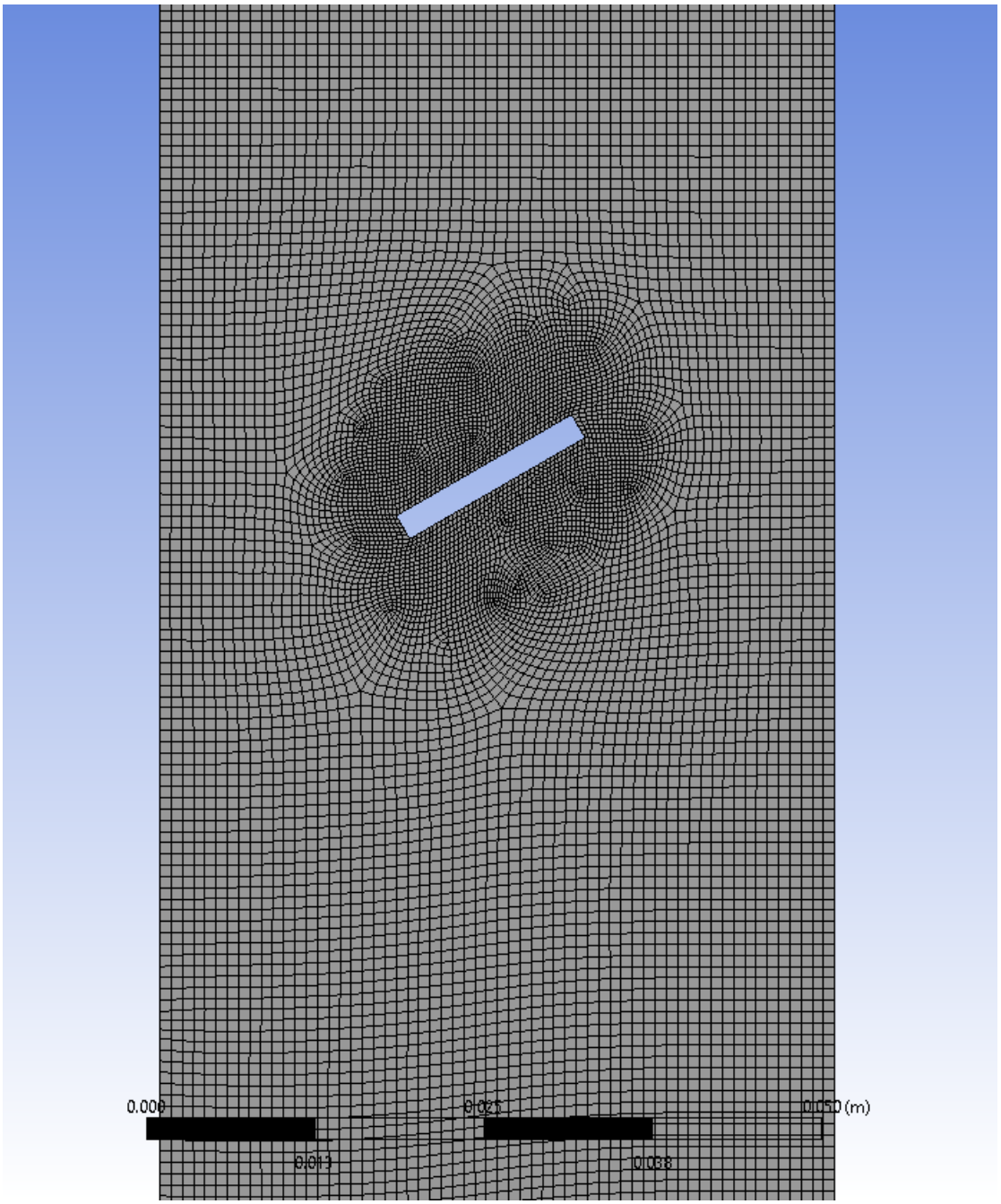

Figure 5-3: Mesh of the domain.

For the multiphase flow model the Eulerian-Eulerian two fluid model is used, where it is assumed that both the primary phase (air) and the secondary phase (particles) are continuous. The volume fraction and the density of these two phases at the main inlet is given in Table 5-4. The Standard $k-\epsilon$ per phase turbulence model with enhanced wall functions was selected for modelling turbulence. The Population Balance Model (PBM) is chosen for describing particle agglomeration with the turbulent aggregation kernel as described in Chapter 4. For solving the population Balance Equation the Sectional-Homogeneous method was selected.

Table 5-4: Properties of the phases

	Air	**Particles**
Volume fraction	0.9997	0.0003
Density [kgm^{-3}]	1.25	1838

For the inlet boundary conditions the speed of the air and particles is 0.8 ms^{-1} at the main inlet. At the jet inlet only air is entering at an velocity of 22 ms^{-1}. The pressure and the no-slip boundary conditions were selected for the outlet and walls, respectively. The initial particle size distribution and the volume fraction of each particle size is shown in Table 5-5.

Table 5-5: Initial volume fraction of particles in bins, labeled by bin center values [38]

	$\mathbf{Bin_8}$	$\mathbf{Bin_7}$	$\mathbf{Bin_6}$	$\mathbf{Bin_5}$	$\mathbf{Bin_4}$	$\mathbf{Bin_3}$	$\mathbf{Bin_2}$	$\mathbf{Bin_1}$	$\mathbf{Bin_0}$
Particle size [μm]	0.43	0.68	1.08	1.72	2.73	4.33	6.88	10.9	17.3
Volume fraction [%]	0.24	3.11	8.62	22.52	29.71	12.93	5.50	10.22	7.15

The simulation is transient with the time step size of 0.001s. Furthermore, the simulation time of 9.5s because after that period the lowest net mass flow rate of 0.0232 kgs^{-1} was achieved. A steady state solution is not obtained because of instability of the main flow at scales equal or larger than the largest length scale of turbulence.

5.4 Results and Discussion

In this section we are going to analyze the flow field inside the agglomerator to see how the air injection influences the motion of particles. Furthermore, the removal efficiency is computed and compared with the initial one. The flow conditions will vary so that we could see the influence of the flow field on particle agglomeration.

5.4.1 Flow field

Before calculating the removal efficiency of the emitted particles it is important to analyze the flow field. The air injection is entering at a much higher velocity than the flue gas at the main inlet, therefore the velocity field near the nozzle will contain a higher level of turbulence. The reasoning behind this is that during the mixing process near the nozzle mechanical energy is supplied to the flow field which will create turbulence and consequently turbulent eddies [4]. These eddies are vortices which come in different sizes as shown in Figure 5-4. Thus, they have a positive effect on agglomeration due to their ability to retain smaller particles close to each other, which will increase the chance for particles to collide, fuse and agglomerate. Unfortunately, RANS cannot capture the turbulent eddy due to lack of resolution, while LES or Direct Numerical Simulation (DNS) can visualize them in the flow field.
The mean velocity field of the turbulent agglomerator can be observed from Figure 5-5. First of all, there is a big velocity difference at the two inlets due to the jet injection, thus the turbulence intensity will be higher in the flow field around inlet 2. After entering the jet stream will interact with the wall, which will result in the creation of a higher level turbulence region near wall region due to the no slip boundary condition. Furthermore, it will result in an high concentration and agglomeration of particles in the vicinity of the wall, but that will be discussed in section 5.4.2. Moreover, another consequence of the air injection is the creation of different scale vortex structures near the nozzle and around the vortex sheets, which can be observed in Figure 5-6.

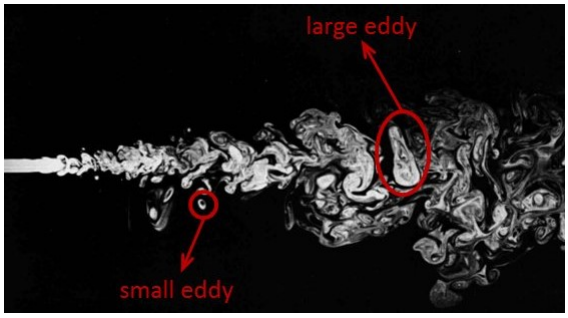

Figure 5-4: Different scale turbulent eddies [9].

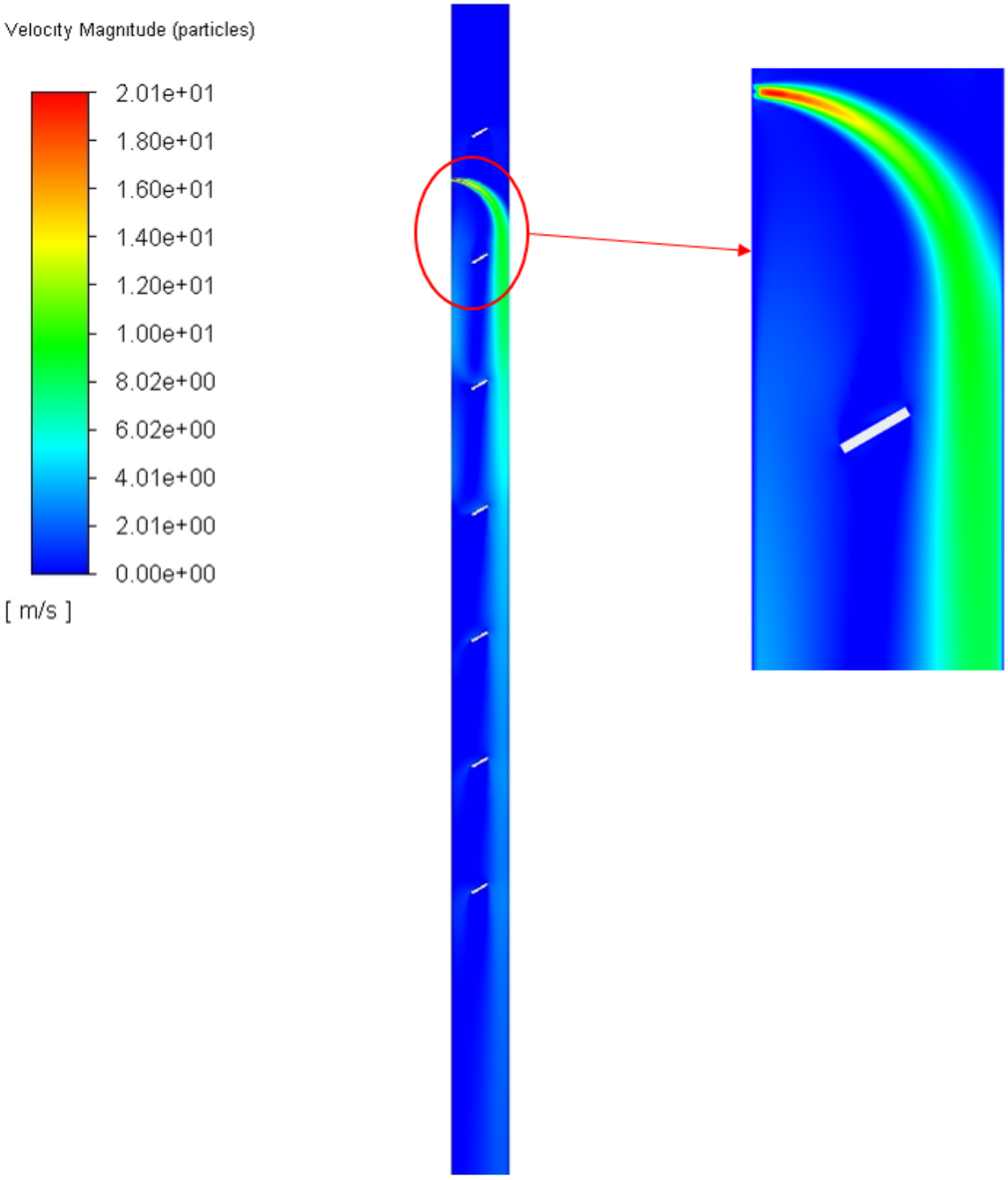

Figure 5-5: Mean Velocity Field of Air.

The vortex sheets promote particle agglomeration by large recirculation zones and smaller vortices around the vortex sheets. Moreover, after the interaction between the fluid and the vane huge recirculation zones are created in the gap space between the vortex sheets, and it is repeating in sequence along the length of the turbulent agglomerator. Furthermore, there is the presence of smaller vortices which are mainly located in the wake region, below the lower left corner of the vortex sheet. However, exceptions are the second vane, which is directly interacting with the air injection and forming a smaller vortice above itself, and the third vane, which does not form vortex at all. Particles which are smaller than the Kolmogorov length scale follow the fluid flow in the recirculation region due to their low inertia. Additionally, the particle flow trajectory is mainly straightforward where they bypass other particles which travel opposite directions, without frequent interaction. On other hand, particles in the smaller vortices have a shorter residence time due to the shorter trajectory, but they are more densely clustered and collide among themselves. Thus, the agglomeration efficiency is much higher in the smaller vortices due to the higher collision frequency of particles. Therefore, it can be concluded that due to the absence of small scale vortexes, the third vane is the least efficient.
Additionally, in the upper parts of the vortex sheets the velocity field is much higher than the lower parts, thus this indicates high turbulence and bigger chance for agglomeration to happen in this zone.

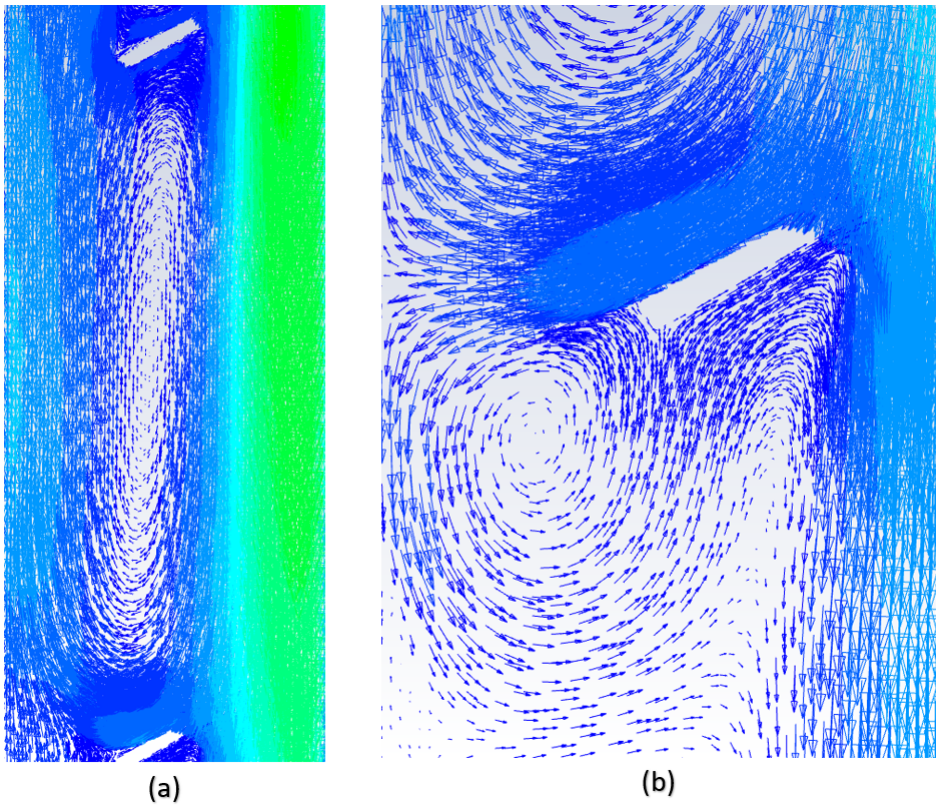

Figure 5-6: Visualization of: (a) Large scale recirculation zone (b) Small scale vortex structure.

5.4.2 Concentration of particles

The initial volume fraction of the particulate phase within the multipiphase flow is 0.0003. However, after 10s of the flue gas flow through the aggloemrator the volume fraction of the particles decreases to 0.00011, which represents a 37% decrease. The reason for the reduction is particle agglomeration which is promoted with the help of the air jet injection and the turbulent agglomerates. Thus, an analysis of particle concentration across the flow field will be performed for the better understanding of particle agglomeration.

Initially at the main inlet the the volume fraction distribution across the cross section is uniform and its the highest. Afterwards, the flow field encounters the first vortex sheets after which it will split and result in a reduced concentration of the particles in the wake region, which can be observed in the enlarged part of Figure 5-7. Furthermore, when the particles reach the jet stream they are redirected to the near wall region, due to the high intensity of the air injection. As a result, high particle concentration zone near the wall and along the length of the agglomerator will be formed. Additionally, the strongest turbulence intensity will be in the vicinity of the jet inlet which will result in a narrower zone of particle concentration near the wall. Latter on, as turbulence weakens along the length of the turbulent agglomerator, the influence of the jet will weaken and the particle concentration zone near the wall will steadily get wider. Moreover, in the zone below the air injection the presence of particles is near zero due to the jet stream that acts like a boundary and prevents particles from entering.

Furthermore, in order to obtain a more accurate behaviour of particles the concentration of the highest and lowest particles size, 17.3 μm (Bin0) and 0.43 μm (Bin8) respectively, was analyzed. The volume fractions of Bin-0 and Bin-8 are observed on Figure 5-8. and we can conclude that for both particles the volume fraction is the uniform and highest near the main inlet, afterwards at the outlet the distribution will become higher non-uniform for Bin-0 and reduced non-uniform for Bin-8. The reasoning for such behaviour we find in the source term for both bins, which is visualized on Figure 5-9 and Figure 5-10, respectively. Nonetheless, for Bin-0 it can be observed that the air injection acts like a source and promotes the creation of bigger particles, thus that is why the volume fraction below the jet injection increases. On the other hand, for Bin-8 the jet stream acts like a sink, which means the jet is promoting removal of fine particles. Furthermore, there exists a weak sink zone along the length of the wall, while at the vortex sheets is one order lover. Therefore, the jet air injection and the wall have a bigger influence in fine particle removal than the vortex sheets.However, vanes still contribute to the removal of fine particles which can noticed in Figure 5-7, where the concentration of fine particles decreases in the wake zones where particle agglomeration happens.

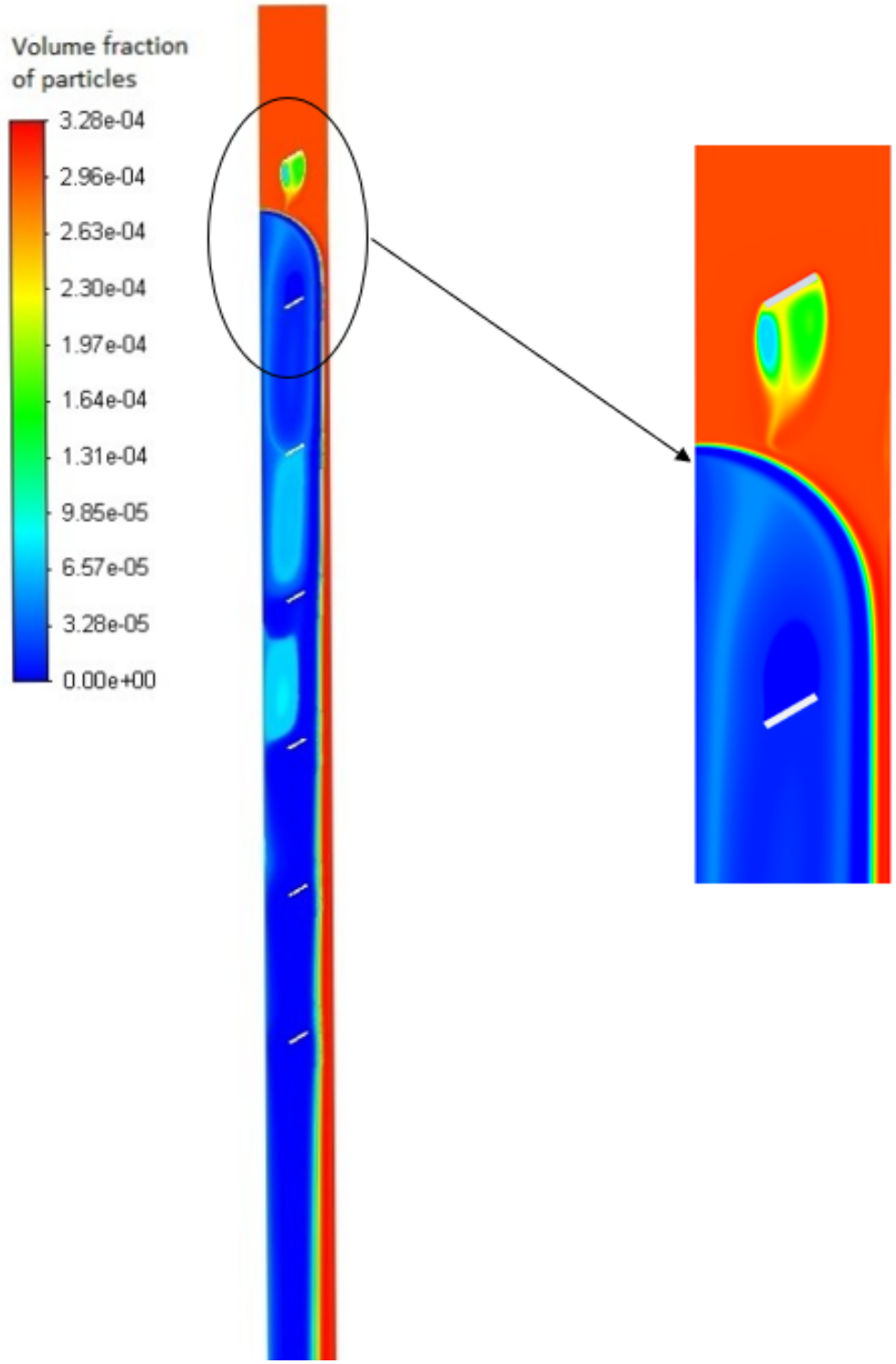

Figure 5-7: Volume fraction of the particulate phase.

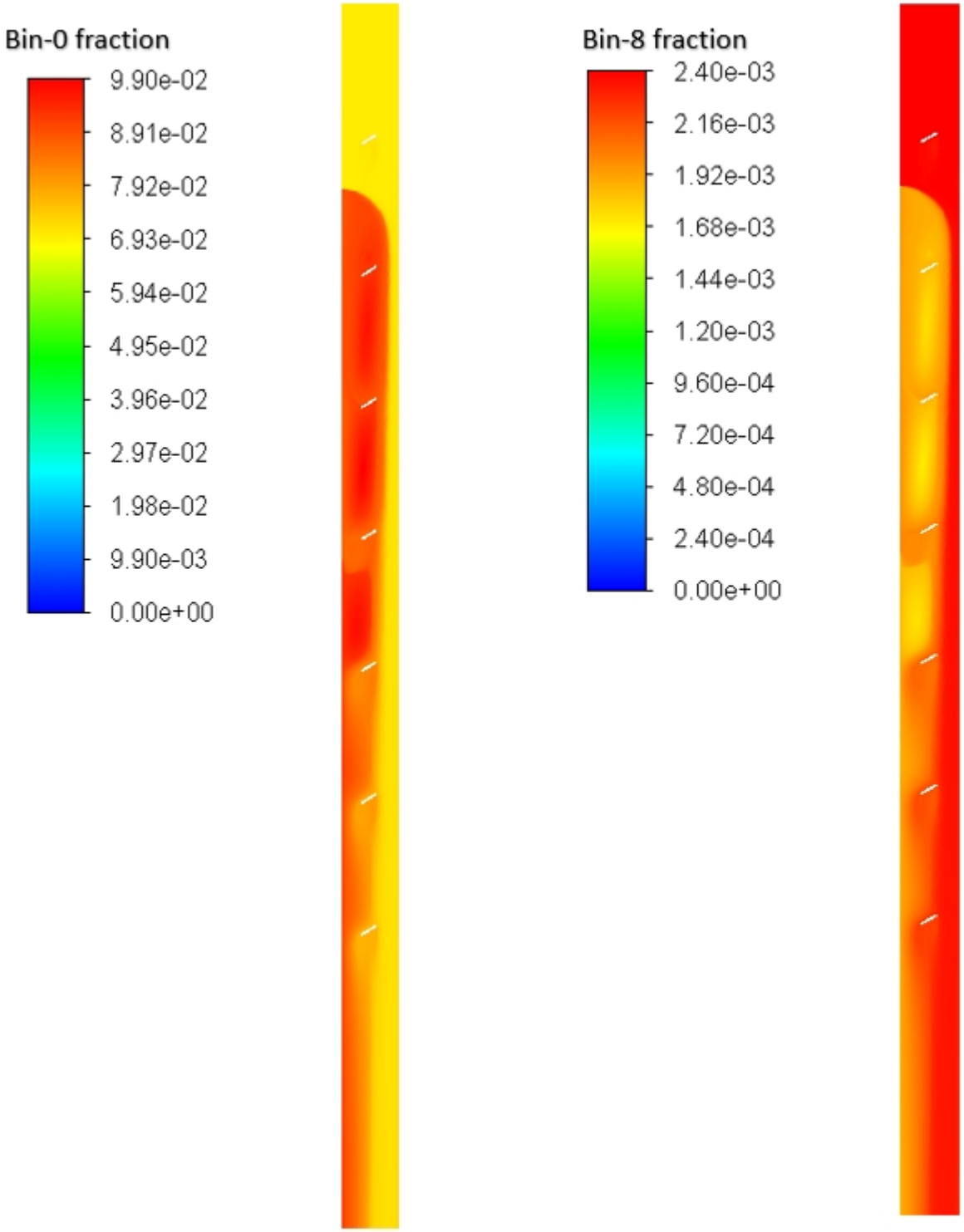

Figure 5-8: Volume fraction of Bin-0 and Bin-8.

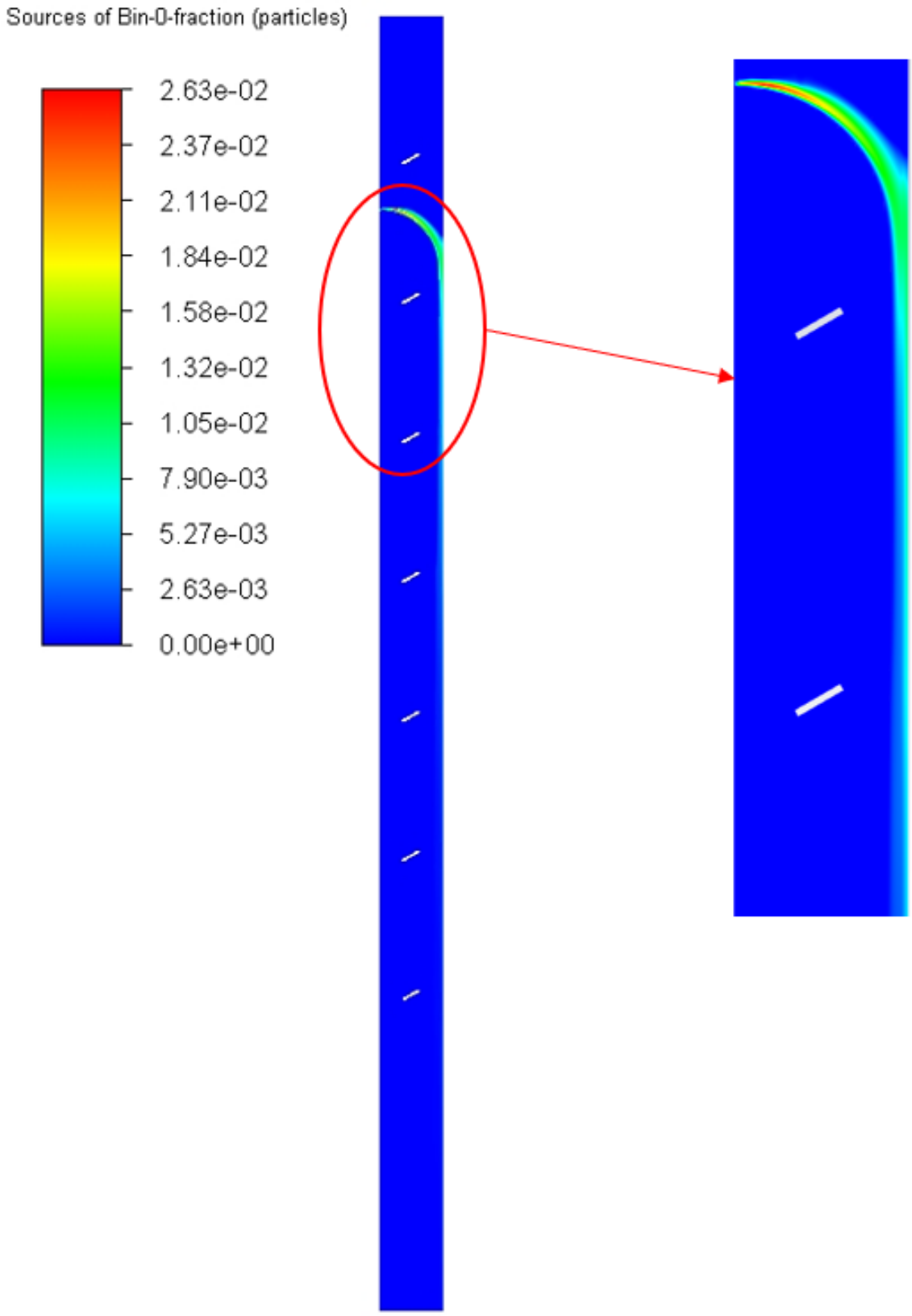

Figure 5-9: Source term of Bin-0.

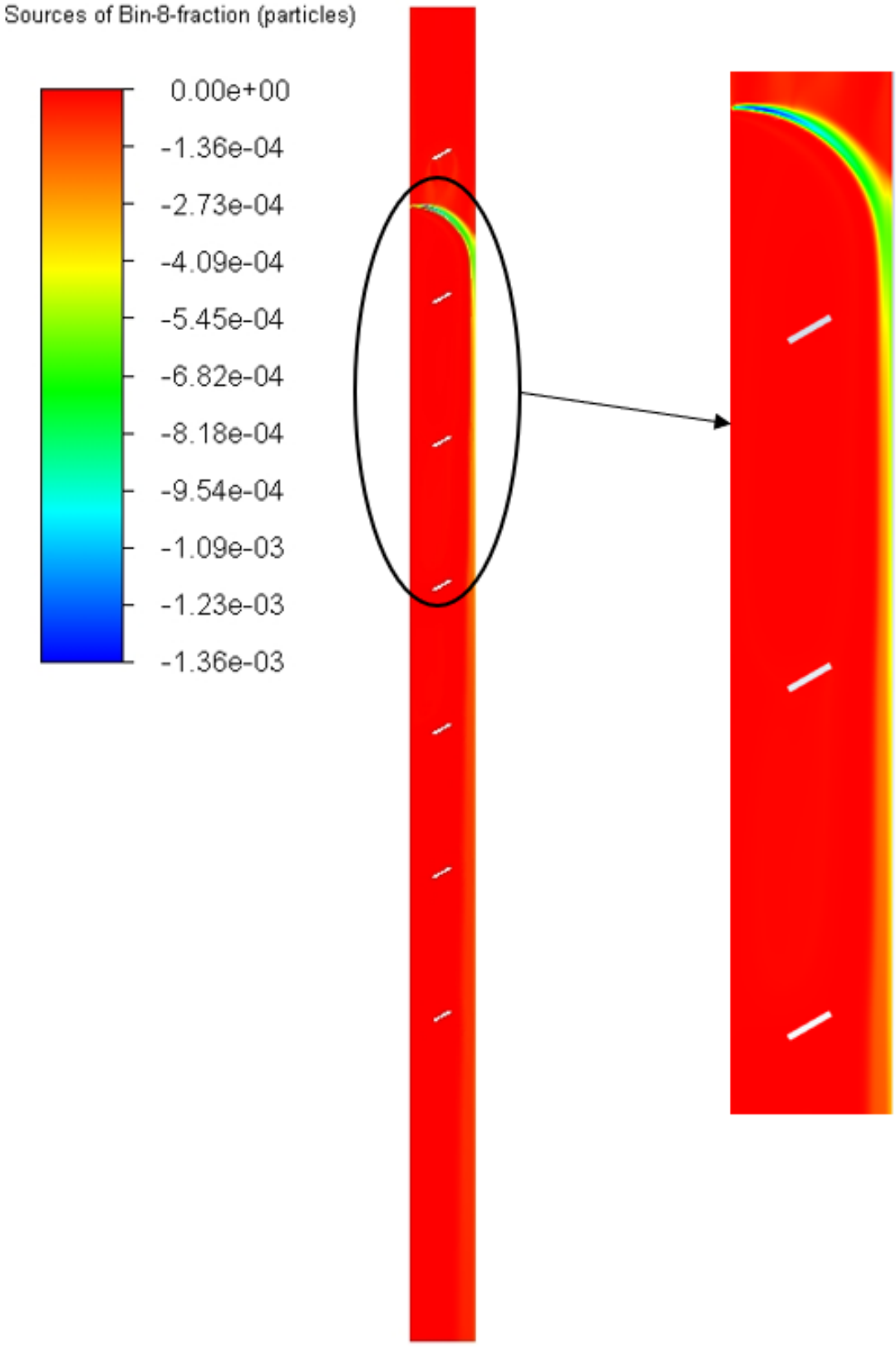

Figure 5-10: Source term of Bin-8.

5.4.3 Removal efficiency

The removal of particles within the flow field is described with the removal efficiency, which is in the literature [57] obtained from the following equation:

$$\eta = \frac{N_{in} - N_{out}}{N_{in}} \times 100 \tag{5-1}$$

where, N_{in} and N_{out} are the number of particles per cubic matter at the inlet and outlet, respectively.

However, in our case we need to consider a scaling factor, which takes into account the dilution effect of air. By injecting pure air through the jet nozzle the flue gas from the main inlet is getting diluted, which will as a consequence decrease the number of particles per unit volume. Therefore, the number of particles at the outlet will indeed be reduced, however not by pure agglomeration. Thus, in order to eliminate this effect a correction factor has been introduced for the inlet number density function (N_{in}), and it is equal to:

$$y = \frac{\dot{V}_{\text{main inlet}}}{(\dot{V}_{\text{main inlet}} + \dot{V}_{\text{jet inlet}})} \tag{5-2}$$

Therefore, the corrected number of particles based on the combination of the two inlet streams, which is used in eq. (5-1), is equal to:

$$N_{\text{in correction}} = y \cdot N_{in} \tag{5-3}$$

The removal efficiency for air injection velocity 22 ms^{-1} is represented in 5-11, and the result for particles larger than 6 μm are found to be in a reasonable agreement with the experimental results. On the other hand, for particles lower than 2 μm exhibit a much bigger deviation is found. Therefore, the numerical model is unable to accurately simulate the removal of particles in the sub-micron range, while the numerical error for larger ones is under 15 %.

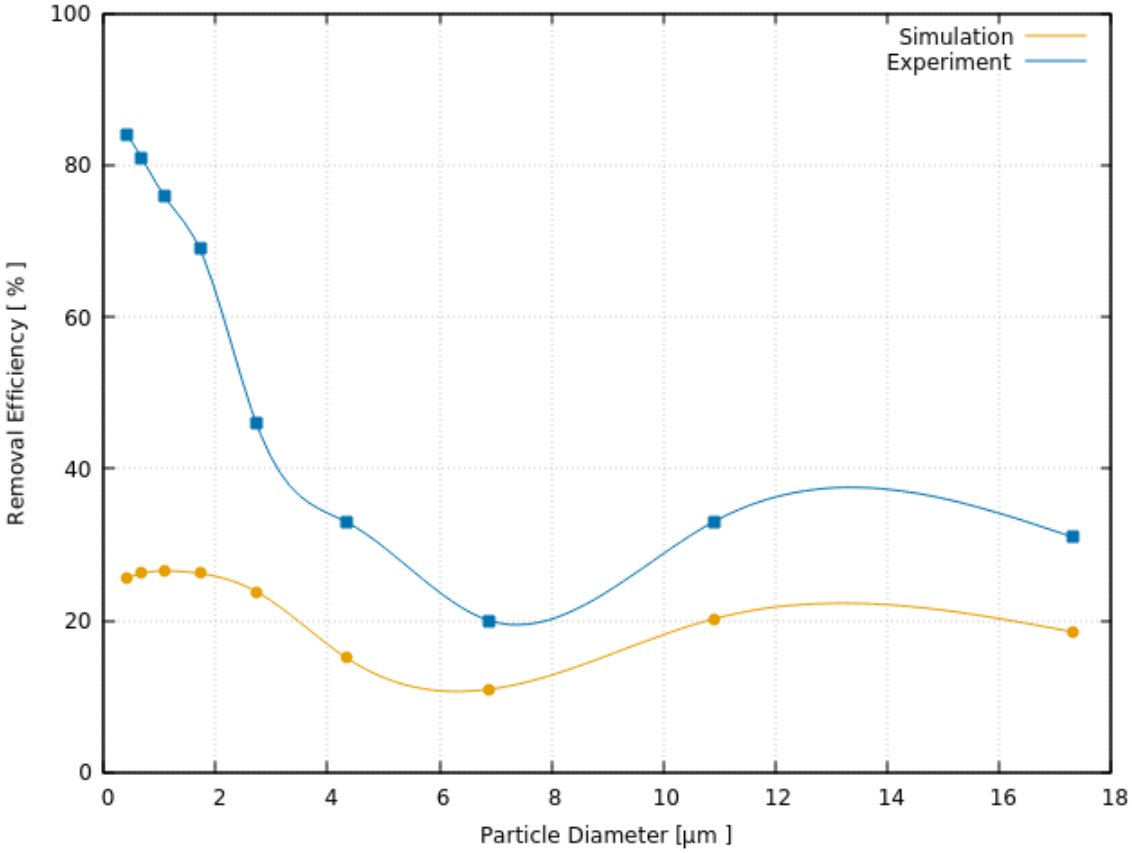

Figure 5-11: Removal efficiency for the air injection velocity of 22 ms^{-1}.

.

Additionally, air injection at different velocities was simulated in order to see how the removal efficiency will be influenced, and the results are shown in the Figure 5-12. The air injection velocity was varied between (0-29) ms^{-1}, resulting in the lowest removal efficiency for 29 ms^{-1}, while the highest was for 11 ms^{-1}. Thus, the magnitude of the velocity plays an important role on particle agglomeration, and an optimal value needs to be chosen.

The low removal efficiency at an air injection speed of 0 ms^{-1} implies the vortex sheets have a weak impact on the agglomeration effect. Furthermore, the removal curve is positive for smaller particles, while for larger ones is negative. Therefore, such behaviour indicates the birth of coarse particles due to their interaction with smaller ones. Additionally, after agglomeration, the smaller particles will be removed.

At 11 ms^{-1} the particle removal is higher than the reference value taken from the literature [38] (22 ms^{-1}), which implies a possibility that the scaling factor was not considered during the computation of the removal efficiency.

The removal efficiency curve of the 29 ms^{-1} jet velocity is purely negative, and indicates particle number density increase due to agglomeration throughout the whole Particle Size Distribution (PSD). Therefore, this velocity would be undesirable as it promotes the production of fly ash particles. On the other hand the numerical accuracy of the results needs further investigation.

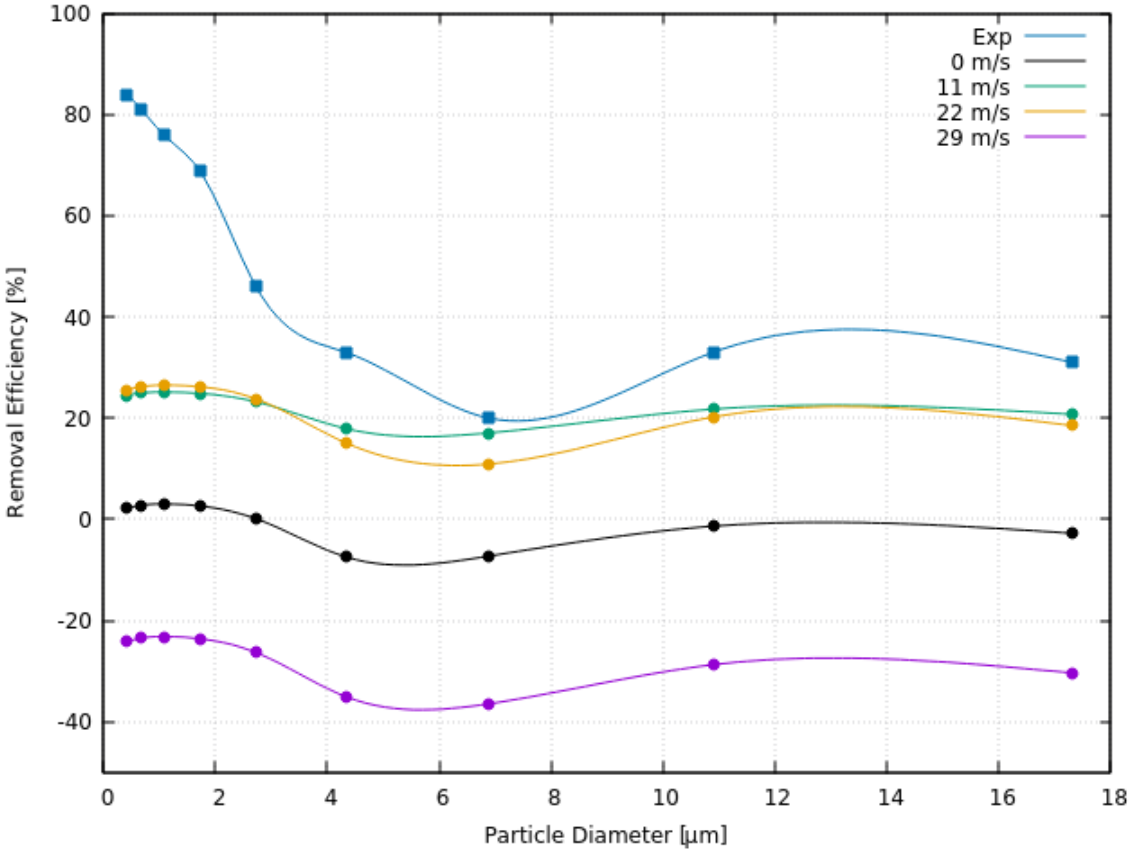

Figure 5-12: Removal efficiency for varying air injection velocity [ms^{-1}].

5.5 Conclusion

From the previous observations, the following conclusions have been made:

1. The air jet injection introduces additional turbulence within the flow field, which causes perturbations, and increases the collision frequency and agglomeration among particles.

2. The jet stream plays a more important role in removing fine particles which was concluded based on the physical source term. Nonetheless, the source terms of the jet and the wall region are negative for fine particles, hence this indicates their removal. On the other hand, the negative source term value of the agglomerator was one order of magnitude lower, thus indicating its weaker influence.

3. The vortex sheets form large recirculation zones in the gap regions between themselves, along the the length of the agglomerator, and small scale vortex structures in wakes. Consequently, the residence time of particles is larger in the recirculation zones due to the longer flow path, but the collision frequency is lower. Therefore, smaller vortices have a stronger influence in promoting particle agglomeration.

4. For the computation of the removal efficiency the scaling factor was introduced, to account for the dilution effect of the injected air.

5. The removal efficiency for the reference speed of 22 ms−1 agrees well for particles above 6 μm, while for smaller particles the error is much larger. Therefore, the numerical model is unable to accurately simulate the removal of particles in the sub-micron range.

6. The removal efficiency for varying air injection speed was investigated, and it was concluded that the magnitude of the jet velocity does not play a crucial role, as the optimal value needs to be chosen.

7. At 0 ms^{-1} the removal efficiency curve will exhibit positive values for smaller particles due to their removal, and negative values for larger particles because of their production due to agglomeration. Furthermore, the highest efficiency is exhibited at 11 μm, thus puts into question whether the scaling factor was taken into account when computing the removal efficiency in [38]. Additionally, at 29 μm the removal curve is purely negative, which indicates particle number density increase due to agglomeration throughout the whole PSD.

Chapter 6

Particle Tracking Analysis for a chimney flow with turbulent agglomerator

In this chapter particle paths are analyzed under the cookstove flow conditions using the Eulerian-Lagrangian dispersed multiphase flow model. Trajectories of particles of different sizes are compared.

6.1 CFD Setup

Turbulent agglomerator 3, which was elaborated in subsection 2.4, was considered for the flow domain due to its high effectiveness. The agglomerator is a long duct with a square cross section, with 8 pairs of Z-type and cross type vortex sheets aligned along the centerline, and it is visualized in Figure 6-1. The length and width of the agglomerator domain are given in Table 6-1 , while other regarding the structure and the arrangement of the vortex sheets can be found in subsection 2.4.1.

Table 6-1: Size parameters of the turbulent agglomerator.

Dimension	**Value[mm]**
Edge fo square cross section	100
Length	1320

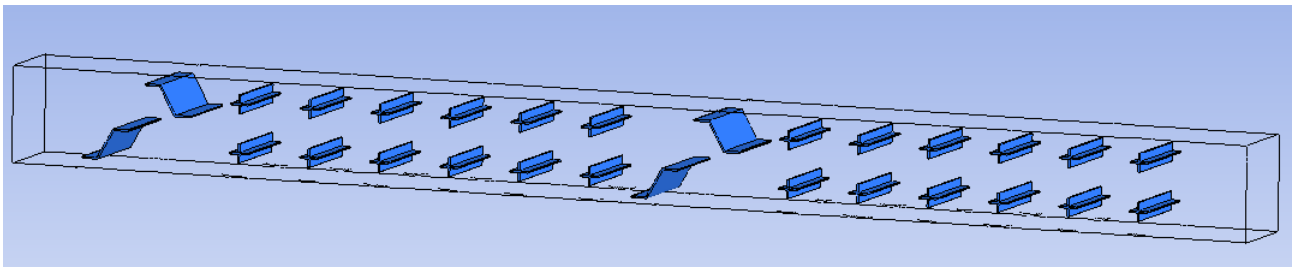

Figure 6-1: Sketch of the structure of the turbulent agglomerator.

The Eulerian-Lagrangian Model is used for following the trajectory of each injected particle, and analyzing the particle flow field. The turbulence of the continuous phase was modeled by using the RNG k-ϵ with the standard wall functions. The governing equations have been described in subsections 4.2.3 and 4.2.2. The energy equation is also solved providing the temperature of the flue gas and the density via the equation of state.

In order to simulate a case more representative of the cookstove chimney some inlet simulation parameters different from those of [57] were used, namely different inlet velocity and temperature were used as shown in Table 6-1. Since the velocity is lower than in the case of [57] it can be expected that the turbulence level and the agglomeration rate by turbulence will be also be lower.

Table 6-2: Inlet simulation parameters for the turbulent agglomerator.

Parameter	Value	Unit
Temperature of the flue gas	405	K
Velocity of flue gas	0.9	ms^{-1}
Viscosity of flue gas	$2.24 \cdot 10^{-5}$	$kgm^{-1}s^{-1}$
Density of flue gas	0.87	kgm^{-3}
Diameter of fly ash particles	0.1; 1; 10	μm
Density of fly ash particles	2100	kgm^{-3}
Inlet velocity of fly ash particles	0.9	ms^{-1}
Total flow rate of fly ash particles	$4.2 \cdot 10^{-4}$	kgs^{-1}

The model was meshed in CF-MESH+ meshing tool, with a structured grid applied in the whole domain. Around the vortex sheets and near the walls grid refinements are applied in order to better resolve the flow at the boundaries. In Figure 6-2 the computational domain is shown. Figure 6-3 shows the refinements at the boundaries. The mesh size and mesh quality parameters are listed in Table 6-3 and Table 6-4. The values of both the skewness and the aspect ratio are in agreement with the reference values from practice, which were mentioned in section 5.3.

Table 6-3: Mesh characteristics

	Number
Elements	2531396
Nodes	2825677

Table 6-4: Mesh quality parameters

Dimension	Value
Average skewness	0.068
Average aspect ratio	1.090

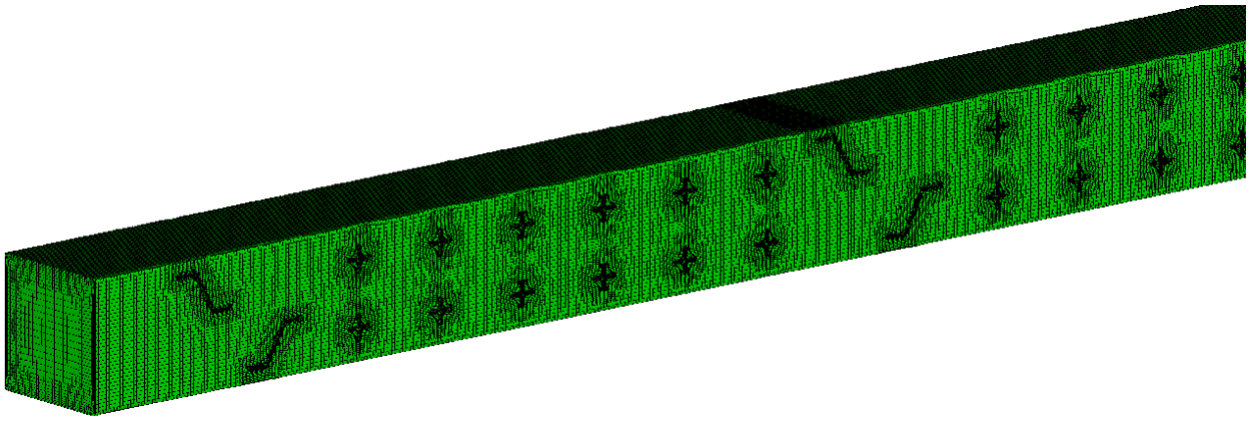

Figure 6-2: Computational domain.

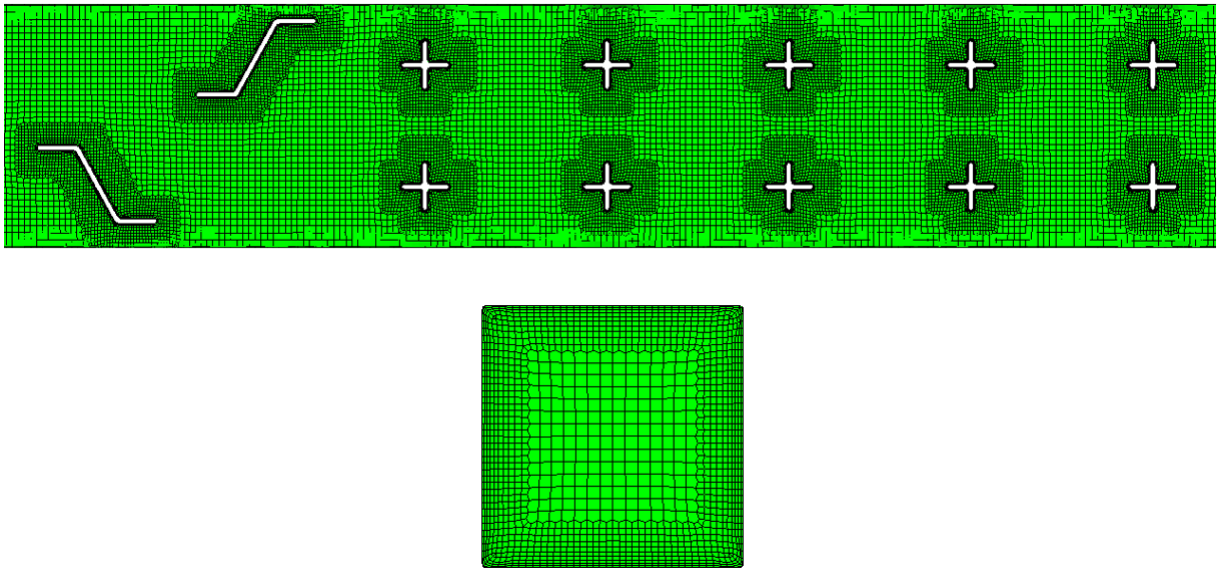

Figure 6-3: Refinements at the boundaries.

6.2 Computed Mean Flow Field

The same flow pattern of the flue gas, as shown for the turbulent agglomerator 3 in subsection 6.3, is found in Figure 6-4, but with a different velocity magnitude. In the case studied here the flue gas is entering at a uniform velocity of 1.62 ms^{-1} through the main inlet. Afterwards, the flow encounters Z-type and cross type vortex sheets which perturb it and increase the turbulence level. The presence of obstacles results in the creation of the high speed main-flow region which is between the two rows of vortex sheets, and a low-speed backflow region, in the wake behind the vortex sheets. A peak velocity of around 4.6 ms^{-1} in the main-flow region will be obtained, an increase by a factor 3 time compared to inlet conditions. Furthermore, in the back-flow region of the vortex sheets large and small scale vortices are created, which have a strong influence on particle dynamics, but that will be elaborated more in depth in subsection 6.3. Due to strong similarities with the flow field of turbulent agglomerator 3 at higher velocity, we can expect that this configuration of vortex sheets works well also under cookstove flow conditions.

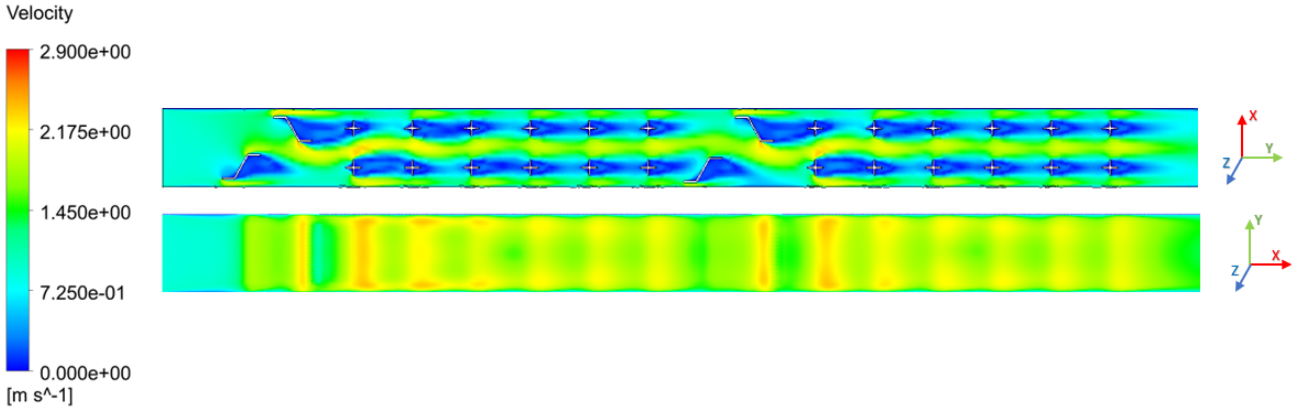

Figure 6-4: The mean velocity field.

6.3 Computed particle tracks

The particle dynamics during the flue gas flow through the turbulent agglomerator can be determined by following the particle. From the x-y plane from Figure 6-4 in can be seen that it is not the mean flow that brings particle in the wake flow. The z velocity component is very small. In the k-ϵ model, the turbulent momentum exchange between mean flow and wake region is represented by the turbulent diffusion. In the Lagrangian particle tracking model this is represented by adding a random component to the particle velocity, depending on local turbulence conditions. In the literature results reviewed in subsection 2.4.4 the trajectories for particles of 0.1;1;10 micrometers diameter were computed and analyzed. Thus, now the goal is to determine the flow path of the same particle size, but different inlet conditions in order to investigate the particle behavior under the cook stove flow conditions.

From Figure 6-5 the particle trajectories of varying sizes are visualized, and we can notice that particles in the fine and ultrafine range have a bigger concentration in the back-flow regions, while the coarse ones are mostly present in the main-flow region. This happens due to the

small inertia of fine and ultrafine particle, hence they follow the flow in the wakes behind the vortex sheets.

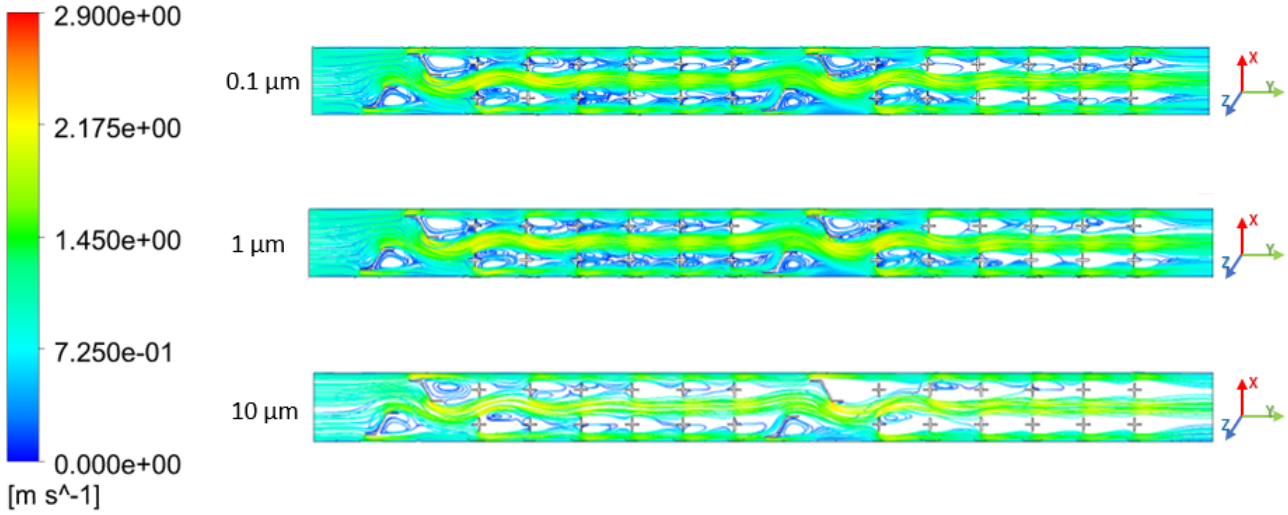

Figure 6-5: Particle trajectories of particles with varying sizes.

We recall that this effect is represented by the Stokes number. According to [57] if $S_T < 1$ then the particle follows the flow, while if $S_T > 3$ then it has an independent pathline. Also, for the computation of the Stokes number eq. 2.4.4 was used, using the overall mean value of the turbulence dissipation rate and the following results were obtained:

Table 6-5: Stokes Number

	Ultrafine	**Fine**	**Coarse**
$\mathbf{S_T}$	0.892	89.2	8920

The result directly reflects the influence of the particle diameter, which enters quadratically in the Stokes number. The values for the submicron and coarse particles differ significantly than the ones gathered from the literature in Table 2-2, as they should be lower due to the smaller inlet velocity. The potential issue could be the Eddy Dissipation Rate used in eq. 2-3, as in our case the volume average value across the flow domain is used. Apart from that, ultrafine and coarse particles satisfy the conditions as the St for the first is smaller than 1, and for the latter much bigger than 3. Therefore, for submicron particles the calculated Stokes number is not valid because from Figure 6-5 it is obvious that they are present in the back-flow region, which implies that they follow the flue gas.

Moreover, the particle residence time also plays a role in particle agglomeration, as the longer it is, the possibility for a collision to happen increases. Thus, their value has been computed and represented in Table 6-6.

Table 6-6: Particle Residence Time

	Ultrafine	Fine	Coarse
t[s]	1.22	1.22	1.11

It was found that particles in in the fine and ultrafine range have the same residence time which, while the coarse have a slightly lower. Furthermore, this is because smaller particles will be retained in the wakes of the vortex sheets, which we can notice from Figure 6-5. Also, due to the increased concentration of fine and ultrafine in the back-flow regions the collision frequency will increase, thus promoting agglomeration among smaller particles. On the other hand, coarse particles from the main flow region fluctuate and interact with other fine particles, which are moving from one wake region to another. Furthermore, after the collision of the coarse and fine particle, they will coalesce and grow.

Therefore, we can have two agglomeration mechanisms, one present in the wake region between fine and ultrafine particles, while the other one is in the main flow region between coarse and fine particles. Furthermore, both agglomeration mechanisms are shown in Figure 6-6.

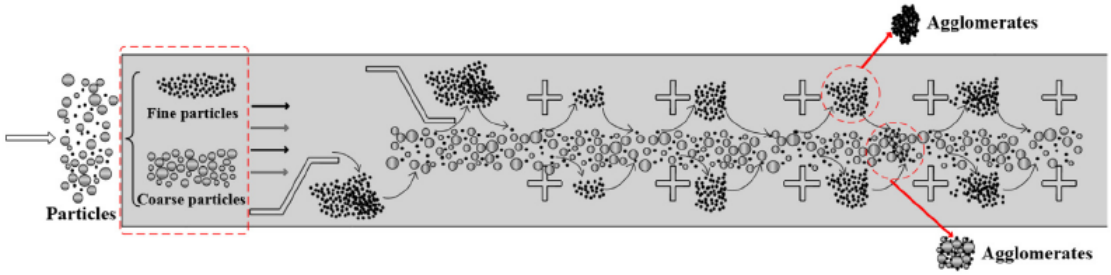

Figure 6-6: Particle agglomeration mechanisms [57].

6.4 Conclusion

The following conclusion can be made based on previous observations:

1. The flow field of the turbulent agglomerator 3 under cookstove inlet conditions forms a similar flow field pattern as in the article of Sun et al [57]. Thus, large scale and small scale vortices are formed due to the vortex sheets, and promote particle agglomeration.

2. Fine and ultrafine particles are clustered in the wake region behind the vortex sheet, because they follow the flow of flue gas due to their low inertia. On the other hand, coarse particles are mostly remain in the fluctuating main-flow region because they do not follow the gas flow so well.

3. The computation of the Stokes number based on a volume averaged dissipation rate is not accurate enough. A local value should be used to better see the border line between particles that follow and not follow the flow.

4. Two agglomeration mechanisms are present, the first is the agglomeration between fine and ultrafine particles in the back-flow regions, and the second is among coarse and fine particles in the main-flow region.

5. Based on the flow field and particle tracks, the configuration of Z-type and cross type vortex sheets can be applied for the cookstove, with the potential of achieving similar removal results as in section 2.4.4.

Chapter 7

Application of population balance equation to turbulent agglomerator

In this chapter the particle agglomeration under cookstove inlet conditions in turbulent agglomerator 3, will be analyzed . Furthermore, the results obtained using the homogeneous solution method will be discussed, that is in particular particle concentration and coalescence within the agglomerator.

7.1 CFD Setup

An Eulerian-Eulerian multiphase flow model was used for simulating the flue gas and the particle phase, Hence both phases were considered to be continuous media. The homogeneous method was used for solving the population balance equation. Furthermore, the drag and the virtual mass force were considered for the interactions among the two phases. Turbulence was modelled using the standard k-ϵ per phase turbulence model with standard wall functions. Additionally, the energy equation was used to account for the temperature effects. Furthermore, the inlet phase characteristics are represented in Table 7-1.

Table 7-1: Inlet phase parameters

Parameter	value	Unit
Flue gas density	0.87	kgm^{-3}
Flue gas velocity	0.9	ms^{-1}
Flue gas temperature [K]	405	K
Particle density	2100	kgm^{-3}
Particle velocity	0.9	ms^{-1}

The particle agglomeration phenomena are described by using the aggregation kernel, discussed in 4.5, on the Population Balance Model. The boundary conditions at the inlet are computed from the Particle Size Distribution curve, which has been obtained through experiments in work of Sun et al. [57], and it is shown in Figure 7-1.

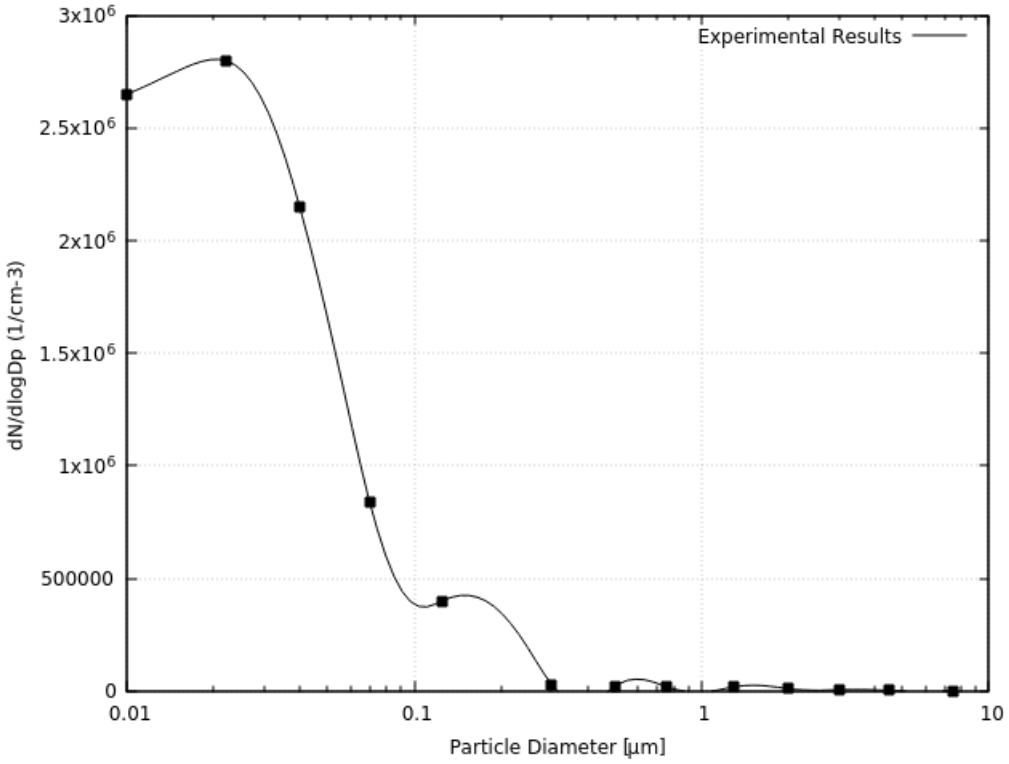

Figure 7-1: Particle size distribution in the flue gas without the turbulent agglomerator [57].

Based on measurements reported in [57] the following derived quantities can be obtained in order to specify the the inlet boundary conditions in the CFD simulation:

$$\begin{aligned} \alpha &= \sum_{0}^{12} N_i \cdot V_i \\ &= \sum_{0}^{12} \alpha_i \end{aligned} \tag{7-1}$$

Where, α is the particle volume fraction, α_i is the volume fraction of the particle size i, N_i is the number of particles of size i per unit volume of the flue gas, and V_i is the volume of a particle size i.
Hence, the bin fractions at the inlet are equal to:

$$f_i = \frac{\alpha_i}{\alpha} \tag{7-2}$$

The bin fractions of the PSD from Figure 7-1 (original flue) are represented in Table 7.1.

Table 7.1 Bin fractions of the initial particle distribution.

	particle size (μm)	fraction
Bin-0	7.5	0.484
Bin-1	4.5	0.209
Bin-2	3	0.155
Bin-3	2	0.0918
Bin-4	1.3	0.0454
Bin-5	0.75	$9.68 \cdot 10^{-3}$
Bin-6	0.5	$3.15 \cdot 10^{-3}$
Bin-7	0.3	$9.29 \cdot 10^{-4}$
Bin-8	0.125	$8.96 \cdot 10^{-4}$
Bin-9	0.07	$3.3 \cdot 10^{-4}$
Bin-10	0.04	$1.58 \cdot 10^{-4}$
Bin-11	0.022	$3.42 \cdot 10^{-5}$
Bin-12	0.01	$3.04 \cdot 10^{-6}$

The computational domain is the same as from the Figure 6-2, however it was necessary to use a smaller number of cells than in the Eulerian-Lagrangian simulation of the same experiment reported in Chapter 6, in order to avoid run time errors in the simulation. The reduced number of elements resulted in thinner refinement zones in the vicinity of the walls and around the vortex sheets. The mesh characteristics and quality parameters are shown in Table 7-2 and Table 7-3. All the mesh quantities are within reasonable ranges.

Table 7-2: Mesh characteristics

	Number
Elements	1892126
Nodes	2166768

Table 7-3: Mesh quality parameters

Parameter	**Value**
Average skewness	0.0941
Average aspect ratio	1.1798

7.2 Computed Mean Flow Field

By using the Homogeneous solution method to solve the PBE, it is assumed that all the particle size classes have the same velocity (In the RANS framework this refers to the mean velocity). The computed particle velocity is visualized in Figure 7-2. The flow pattern is similar to the flue gas flow field from sections 2.4.3 and 6.2 where the EL method was applied, and the flow in analysis in sections 2.4.3 and 6.2 is also valid here.

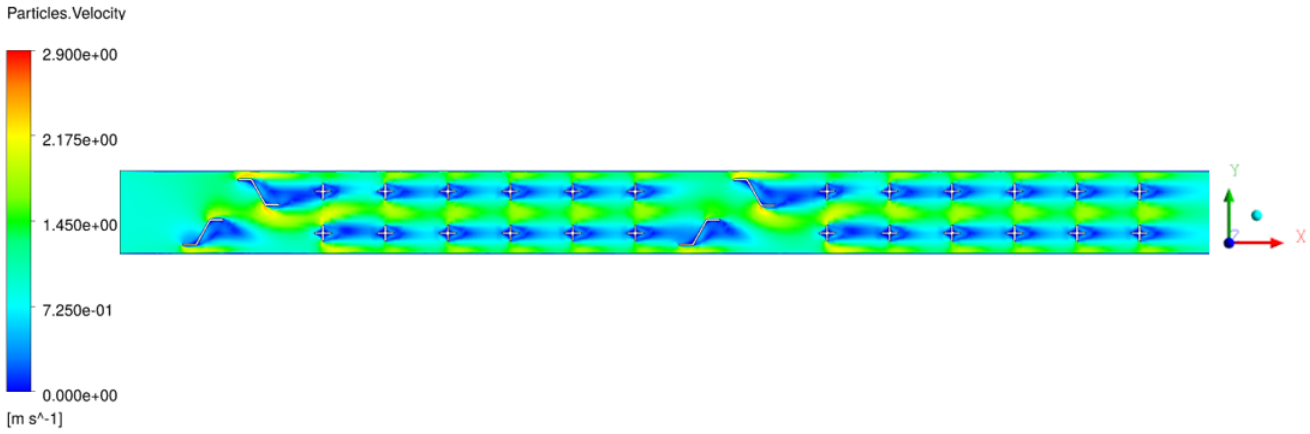

Figure 7-2: Particle mean velocity field.

Nevertheless, some more comments can be given related to the impact for the processes described by the PBE. The particles enter through the inlet at a uniform velocity of 0.9 ms^{-1}. They encounter Z-type and cross-type vortex sheets that will create turbulence. The turbulence will result in turbulent agglomeration in addition thermal effect of Brownian motion. Whereas the Brownian motion effect is depending on temperature, the turbulence effect depends on the turbulent energy dissipation rate. 6.3. But both effects have more time to play their role when the residence time is larger. This can happen in the stagnation points before and the wakes behind the obstacles in the flow. Therefore it can already be expected that the agglomeration rate per unit volume will be largest in those areas. More detail on the flow field is provided by the vector field of mean velocity shown in Figure 7-3. If the particles. It should be recalled that the particle motion is not following this vector field since turbulent diffusion is superimposed on it by the turbulent diffusion term in the mean momentum equation. But longer residence time in combination with higher turbulence dissipation rate are the factors that combine to lead to larger effect of turbulent agglomeration. It can be argued that the smallest particles have higher probability to end up in the wake region since they follow all motions of the flow, and then are more densely clustered and collide in the wakes of the vortex sheets, whereas on the other hand the in the main flow channels between the obstacles or between the wall and the obstacles the main clustering mechanism is the interaction between coarse and fine particles that are leaving the wake region. However this can not be confirmed from the mean flow field of the particle phase.

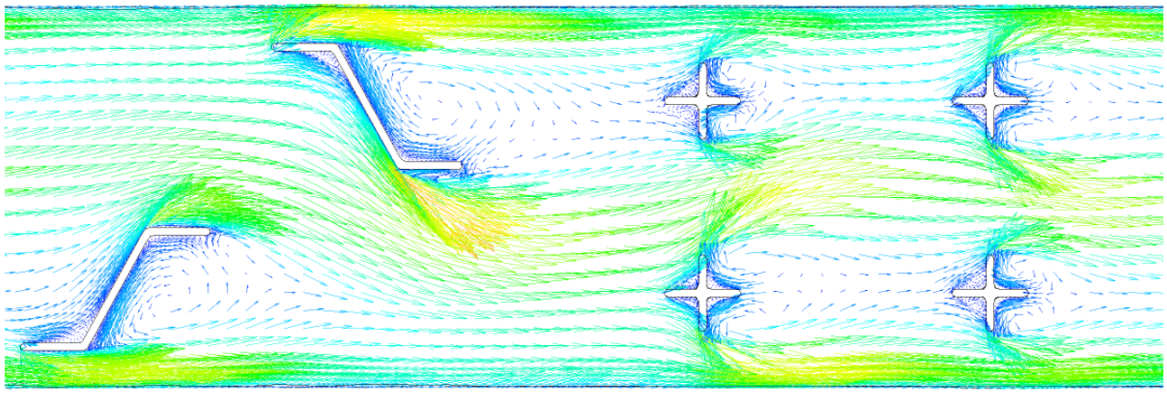

Figure 7-3: Mean vector velocity field of the particulate phase.

7.3 Particle Concentration

The volume fraction of the particulate phase in the flue gas is uniform at the inlet and equal to $4.573 \cdot 10^{-7}$. Afterwards, the fluid flow encounters obstacles, which will introduce an instability and cause a chaotic motion of particles. The increased turbulence will promote particle agglomeration. The agglomeration process leads the volume fraction of all particles together unchanged. Nevertheless after some time the predicted particle volume fraction pattern shows slight nonuniformity as shown in Figure 7-4 is obtained. Te highest concentration of particles is observed in the wake of the second Z-type vortex sheets of the first row, and close to the upper wall. A possible explanation for the appearance of nonuniformity in the total particle volume fraction in the homogeneous model is the effect of the overall slip between the gas phase and the particle phase. In this way they might slightly redistributed differently in space. But it should not be seen as a direct effect of agglomeration. But a contribution from numerical error cannot be excluded and could be studied using grid refinement. In order to understand the agglomeration phenomena the concentration of different particle size classes should be studied and this is done next.

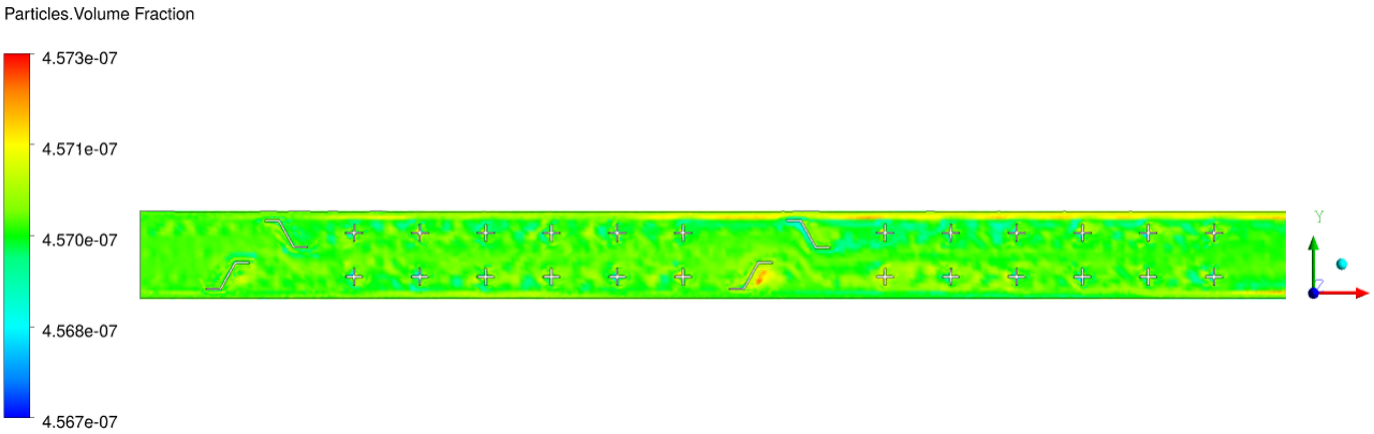

Figure 7-4: The volume fraction of the particulate phase within the flow field.

The behaviour of the smallest and largest particle sizes, 0.01 μm (Bin 12) and 7.5 μm (Bin 0)

respectively, were investigated by analyzing their volume fraction in the particle phase and their source terms. These two terms are of key importance as they combined fully describe the agglomeration process.

First, the concentration (bin-fraction f_{12}) of the smaller particle is shown in Figure 7-5 (a). The value at the inflow is very small: $3.04 \cdot 10^{-6}$(See Table 7.1) and the difference between the highest and lowest value is quite small. It indicates a rather weak agglomeration process present in the flow domain. Nevertheless, the uniform spatial distribution at the inlet changes into a nonuniform distribution by a local decreases that predominantly takes place under the influence of the vortex sheet arrangement, reaching eventually a fraction of around $2.994 \cdot 10^{-6}$. Thus, this will result in an 1.5 % volume fraction decrease when compared to the initial state. Furthermore, in the wakes behind the vortex sheets the concentration of particles is small compared to the rest of the domain. Hence this indicates that particle coalescence has most direct effect that region. To demonstrate this effect further, the source terms of the same particle size is visualized in Figure 7-5 (b). As expected, in the wakes of the vortex sheets the source term is stronger (more negative) than in the rest of the flow domain, thus this confirms that small particle removal by agglomeration is mostly occurring in the vicinity of the obstacles. It should be remarked that in the population balance equation the evolution of concentration is determined both by the agglomeration and by the spatial transport by convection and diffusion. The concentration value is then the result of the combined effect. If the agglomeration rate is too slow the concentration would be only determined by the physical transport and the observed effect would not be seen.

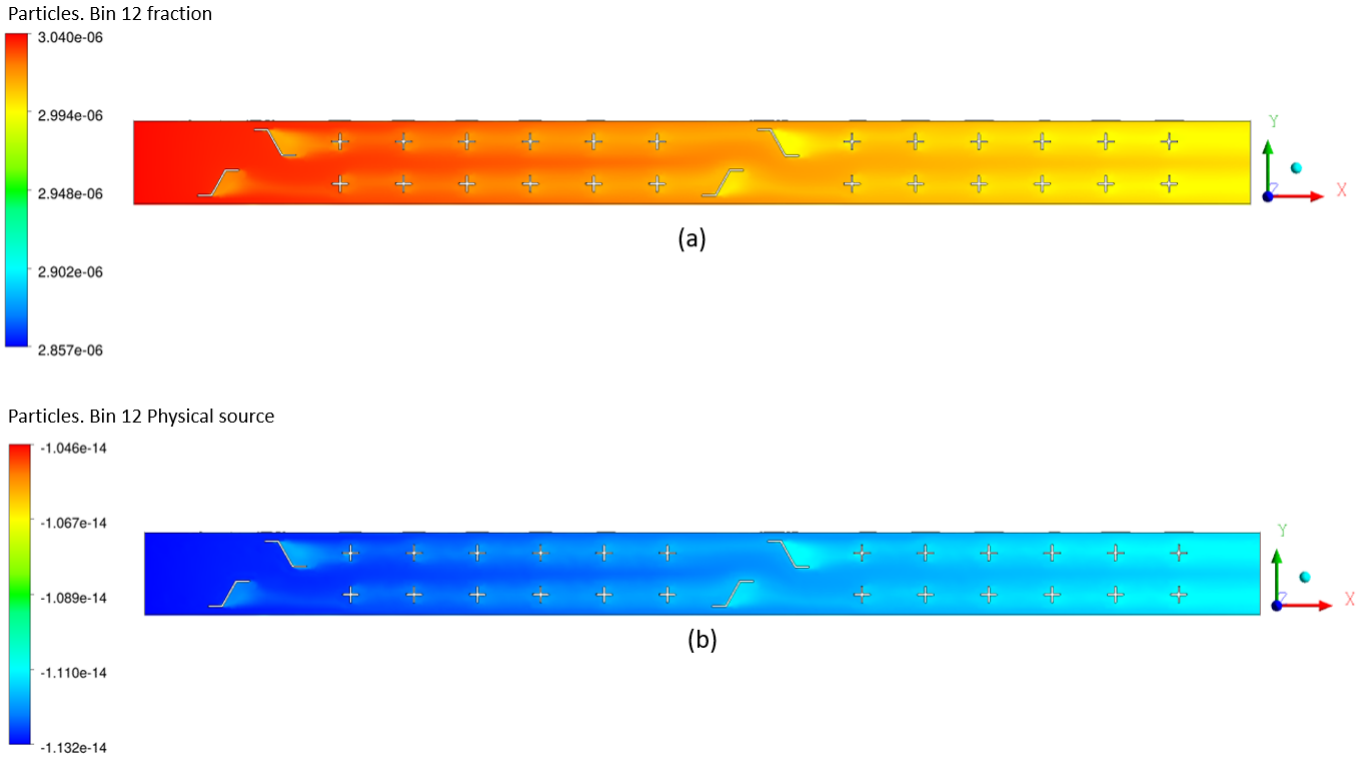

Figure 7-5: (a) Bin-12 fraction of the particle phase; (b) Bin-12 physical source term of the particle phase

Next, the behaviour of the largest particle size (Bin 0) was investigated. This is the particle size that in the end collects all particles and is expected to increase. The value at the inlet was specified to be 0.483 according the data in table 7.1. But Figure 7-6 (a) shows 0.4838, possibly a postprocessing error in the software. Nevertheless analysis can proceed. In the wakes of the vortex sheets the concentration of particles is larger by a very small amount. Moreover, the source term from Figure 7-6 (b) indicates that volume fraction of coarse particles increases but the rate is about one order of magnitude smaller than the rate at which the fraction of the smallest particles decreases. This indicates that the agglomeration process is effective in removing the smallest particles to produce intermediate size particles. This is possible, but depends on several factors: whether agglomeration kernel is acting unequally strong for small and large particles, where there is sufficient time for particles to make several agglomeration steps. The accurate prediction can also depend on the numerical accuracy of the discretization of the PBE. How many size classes are used; how is agglomeration handled of two size classes that combine to a value that is not exactly one of the size classes that is considered in the numerical discretization. The last issue is not documented in the available ANSYS Fluent manual. In the next section we present further analysis looking at the agglomeration kernel.

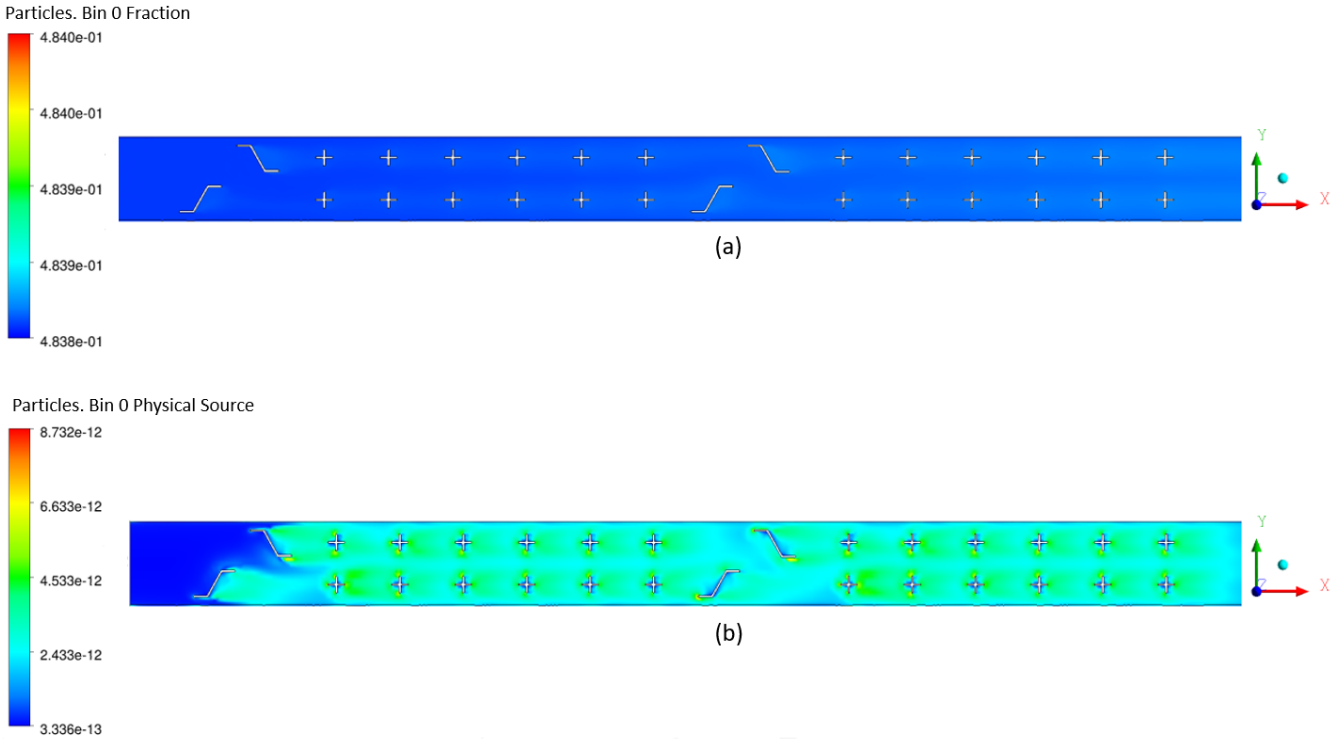

Figure 7-6: (a) Bin-0 fraction of the particle phase; (b) Bin-0 physical source term of the particle phase

7.4 Combined aggregation kernel

In order to describe the particle aggregation phenomena in our simulation, a combination of the Turbulent (4.5.2) and the Free Molecular (4.5.1) aggregation kernels has been used, given by:

$$a_{comb}(L_i, L_j) = \sqrt{a_T^2 + a_F^2} \tag{7-3}$$

Where a_T and a_F are the turbulent and free molecular aggregation kernels.

Before analyzing the removal efficiency it is important to see which aggregation kernel has a bigger influence on the particle agglomeration. This issue has been addressed by Rigopoulos et al. [44] by providing the graph shown in Figure 7-7. Each region in the graph characterizes the agglomeration mechanism used. Aglomeration due to Brownian motion of particles corresponds to our Free molecular kernel, while the Turbulent shear region indicated the Turbulent aggregation region.

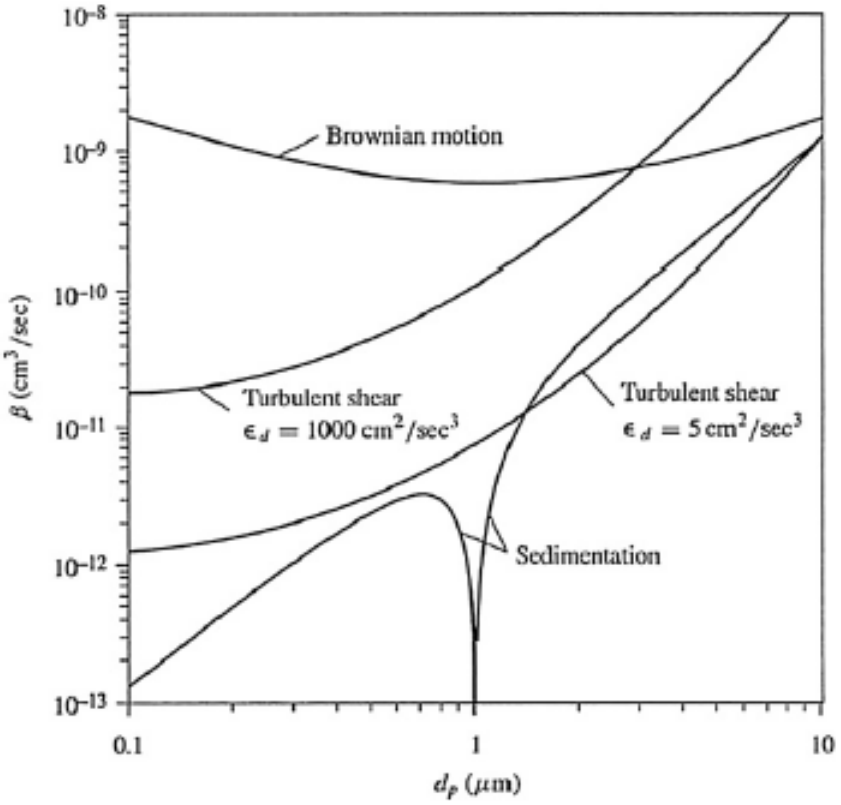

Figure 7-7: Comparison of coagulation kernels for 1 μm particles interacting with 0.1–10 μm particles. [44]

In order to determine where in the Figure 7-7 is the turbulent agglomerator situated, the combined agglomeration kernel, eq.(7-3), was computed and represented in Figure 7-8 (Here we use linear scale instead of the logarithmic scale used in 7-7). For the calculation of the turbulent kernel the average dissipation rate from the wake region was used. Also,the temperature of the whole flow domain is 405 K, as the walls are assumed to be adiabatic. It is found that the Kolmogorov length scale is bigger than the largest particles considered in the PSD, thus only the viscous sub-range of the turbulent aggregation kernel was considered.

From the results shown in Figure 7-8 it can be noticed that both aggregation kernels are equal for particle size of 1.3 μm. However, as the size increases the slope of the turbulent aggregation kernel becomes more steeper, while the Free molecular shows a small increase. Therefore, for particles outside the sub-micron range turbulent aggregation mechanism is dominant. On the other hand, for particles smaller than 1.3 μm, the free molecular kernel is much larger than the turbulent. Therefore, this confirms the observation also made in [4], that particles in the sub-micron range will agglomerate mostly due to the Brownian motion, while larger ones will due to the turbulence effects of the flow field.

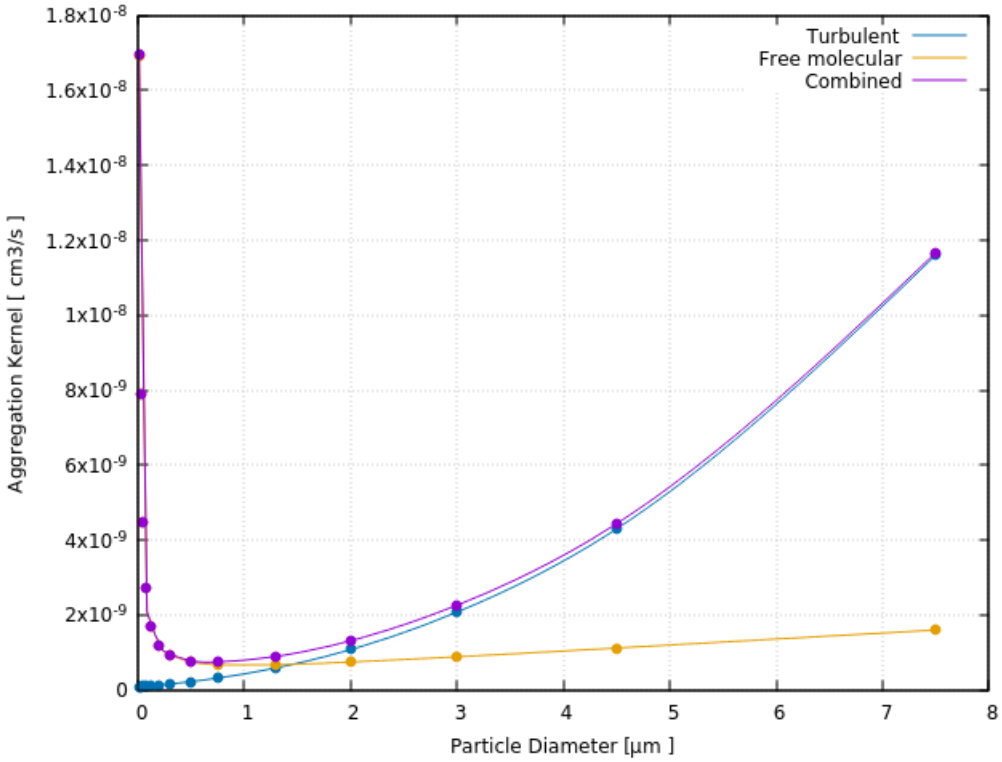

Figure 7-8: The combined aggregation kernel for 1 μm particles interacting with 0.01–7.5 μm particles.

7.5 Removal Efficiency

The removal efficiency of the turbulent agglomerator represents the particle number reduction at the outlet due to the agglomeration process. Furthermore, the formula from Sun et al. [57] was used:

$$\eta = \frac{N_{in} - N_{out}}{N_{in}} \times 100 \tag{7-4}$$

Here $N_{in,i}$ and $N_{out,i}$ are the number of particles of size i at the inlet and outlet of the turbulent agglomerator.

Under the cookstove operating conditions where the inlet velocity speed is 0.9 ms^{-1}, the agglomeration efficiency for ultrafine particles is below 1 %, while for larger ones is 0 %. Hence, the agglomeration effect is quite weak within the agglomerator for the specified operating conditions.

However, after sensitivity analysis it was found that if the volume fraction of the particulate phase is increased by a factor of 100, the removal efficiency would increase as well. Furthermore, the result for all size classes is presented in Figure 7-9. Thus, in this case the removal efficiency of ultrafine particles is very good and correspondingly the number of particle size of 0.3 μm size has increased. Therefore, in case of (unwanted) high volume fraction particulate phase more collisions within the flow domain will happen, resulting in an increased agglomeration and stronger removal effect. But more importantly Figure 7-9 acts as a reminder

that looking at number of particles per size class it is clear that elimination of the smallest particles goes together with growth of intermediate size particles and the whole range of size classes should be taken into account in a full analysis.

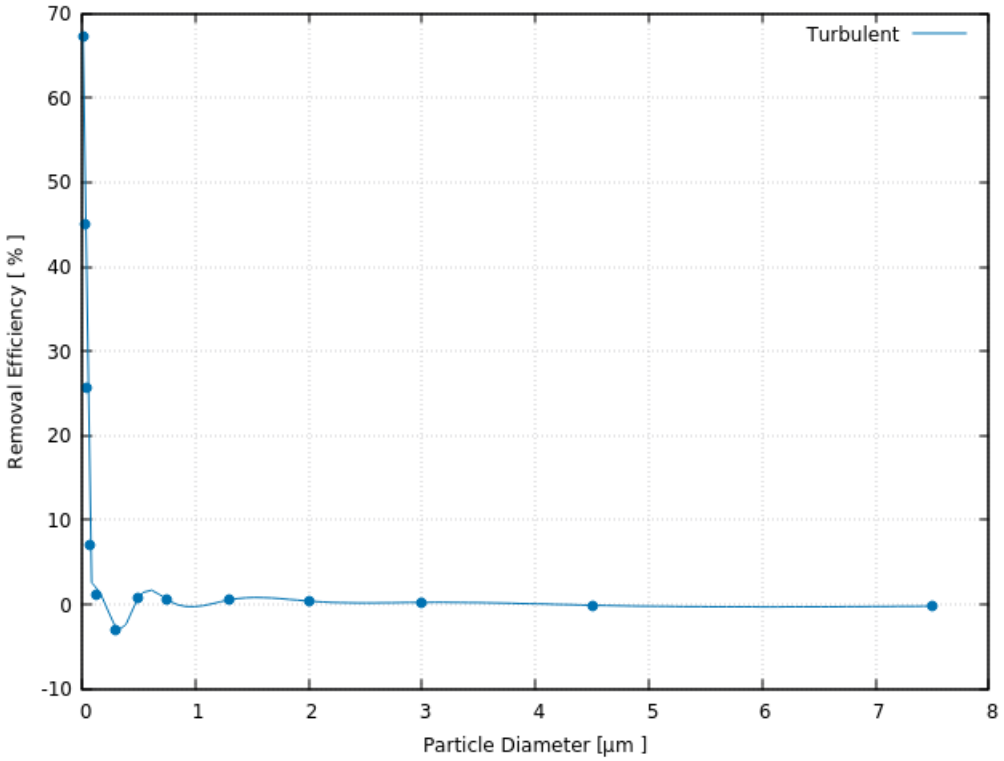

Figure 7-9: The removal efficiency for a more concentrated flue gas.

7.6 Conclusions

From the previous observations the following conclusions can be made:

1. The flow pattern in the turbulent agglomerator is similar to the one researched in subsection 2.4.3, where a high removal efficiency was observed. However, the possibility of achieving the same results under cookstove operating conditions also depend on the turbulence level.

2. The Z-type and cross type vortex sheets configuration creates different scale vortices, that retain particles for a longer time in wakes and in this way promotes particle agglomeration.

3. The behaviour of the smallest and largest particle sizes, 0.01 μm and 7.5 μm respectively, was investigated by analyzing their concentration and source terms. As a result, it was found that the removal of ultrafine particles is stronger in the wakes of the vortex sheets, and weaker in the main-flow region and in the vicinity of the wall. Furthermore, the source term of coarse particle volume fraction is found three order of magnitudes smaller than that of smallest particle volume fraction.

4. The Kolmogorov length scale is larger than all the particles from the size distribution, therefore viscous sub-range of the Turbulent aggregation kernel is only used.

5. The Free molecular aggregation kernel dominates for submicron particles, while turbulent aggregation kernel has a stronger influence for bigger ones.

6. The removal efficiency for the turbulent agglomerator under cookstove operating conditions is under 1 %, thus indicating a weak agglomeration effect within the flow domain. However, the removal efficiency increases for a case with a larger particle volume fraction.

Chapter 8

Conclusions and Recommendations

In this master thesis the possibility to lower ultrafine particle emissions from wood fired cookstove was investigated. The following conclusions have been reached:

1. From the literature review of the state of the art particle removal technology the turbulent agglomerator was found to be a promising solution for wood fired cookstoves. The dimensions of the agglomerator studied in the literature are comparable to a cookstove chimney, and using an existing design seems possible. Furthermore, except for the construction cost, the agglomerator benefit comes for free. It does not need a power source to function, therefore it is economical.

2. The configuration of turbulent agglomerator 3, from the work of Sun et al (2019) [57], was chosen for further investigation, because it showed best performance among a set of studied cases. In experiments the turbulent agglomerator 3 has been found to give the highest agglomeration efficiency: 37.8 % for particles in the ultrafine range, for the case of inlet velocity of 10 ms^{-1}. An explanation has been provided in the literature: the combination of z-type and cross-type vortex sheets in this agglomerator produces a turbulent flow with a range of vortex sizes. The wakes behind the obstacles provide regions of high residence time of fine and ultrafine particles. They shear layers provide high spatial dispersion of coarse particles in direction transverse to the main flow (Y-direction fluctuations) also beneficial for agglomeration.

3. The representative values of velocity and the inlet temperature of the chimney have been determined by a very simple analytical model for flow and heat transfer in the cookstove and chimney. These boundary conditions have been used in the CFD simulation of the 3D turbulent agglomerator with both EL and EE methods. For the application to the cookstove chimney operation at lower velocity and lower turbulence level has to be considered and the achievable efficiency cannot be simply taken from the literature.

4. In a preliminary investigation a case with agglomerator combined with air jet injection was studied in a 2D CFD domain. Based on the source term of smallest particle size,

it was found that the jet air injection has a stronger influence in particle removal than the vortex sheets of the agglomerator.

5. In this case with air injection, the removal efficiency was carefully calculated taking into account a scaling factor, to account for the dilution effect of the injected air.

6. The removal efficiency at the reference speed of 22 ms^1 agrees well with experiments for particles above 6m, while for smaller particles a large error is obtained. Therefore, the numerical model is unable to accurately simulate the removal of particles in the sub-micron range. It is not clear to what extend this is due to the simplified setup and to the model performance.

7. 3D CFD simlations were made of the turbulent agglomerator 3, first using the EL approach. The mean flow field obtained and under cookstove inlet conditions, shows similar mean flow field pattern as in the article of Sun et al [54]. Thus, large scale and small scale vortices are formed due to the vortex sheets, that can promote particle agglomeration. Furthermore, fine and ultrafine particles cluster in the wake region where they collide and agglomerate, while coarse particles remain in the fluctuating main-flow region from where they remove smaller articles. Therefore, based on only the type of flow field and particle tracks, the configuration of Z-type and cross type vortex sheets seem adequate for the cookstove, with the potential of achieving similar removal results as in section 2.4.4. However, the turbulence level is lower than the reference case will also have to be taken into account.

8. Next the same case was simulated using the EE approach in combination with the combination of the Free molecular and turbulent aggregation kernels to simulate particle agglomeration via the PBE. The first kernel was found to dominate for particles below the submicron range, while the second is stronger for larger particles.

9. The behaviour of the smallest particle size, 0.01 μm, was investigated by analyzing the concentration and source terms. Consequently, it was found that the removal of ultrafine particles is stronger in the wakes of the vortex sheets, and weaker in the main-flow region and in the vicinity of the wall.

10. The simulations using the PBE provided quantitative results for the evolution of the volume fraction of different size classes of particles. It was found that for the considered chimney (lower velocity, hence lower turbulence level) the turbulent agglomeration effect is too weak to obtain a sufficient removal efficiency of submicron particles (under 1%). In case of higher particle load higher removal efficiency can be achieved.

Furthermore, the following is recommended for future research:

1. An extension for the algebraic model is needed to account for the influence of the turbulent agglomerator.

2. Other methods for solving the Population Balance Equation (PBE) should be explored to obtain more accurate results. Simple increase of the number of size classes considered in the discrete representation can already lead to better accuracy. The inhomogeneous solution method for solving the PBE, should be used if the different particle size classes

are expected to have different velocity. However, all these improvements lead to larger computational cost. Alternatively the Method of Moments provides, at lower cost, another way to represent the PBE shape and could be more effective.

3. Particle agglomeration could be added to the EL model. In this way the benefit of having particle trajectories can exploited in more detailed description of agglomeration, in comparison with using an agglomeration kernel. This method offers alternative methods to represent the physical processes of agglomeration.

Bibliography

[1] Bologa A., Paur H., and Woletz K. "International Journal of Plasma Environmental Science and Technology". In: *Journal of Electrostatics* 5 (Dec. 2011), pp. 168–173. ISSN: 18818692.

[2] Bologa A. et al. "Fine particle generation, evolution and control by small biomass combustion". In: *Management of Environmental Quality* (Oct. 2010). URL: www.emeraldinsight.com/1477-7835.htm.

[3] Valavanidis A., Flotakis K., and Vlachogianni T. "Airborne particulate matter and human health: Toxicological assessment and importance of size and composition of particles for oxidative damage and carcinogenic mechanisms". In: *Journal of Environmental Science and Health - Part C Environmental Carcinogenesis and Ecotoxicology Reviews* 26 (2008), pp. 339–362. URL: https://doi.org/10.1080/10590500802494538.

[4] *ANSYS Fluent Population Balance Module Manual 15.0*. ANSYS, Inc., 2013.

[5] *ANSYS Fluent Theory Guide 15.0*. ANSYS, Inc., 2013.

[6] Guo B., Yu A., and Guo J. "CFD modelling of flue gas particulates in a biomass fired stove with electrostatic precipitation". In: *Journal of Aerosol Science* 77 (Aug. 2014), pp. 102–115. URL: https://doi.org/10.1016/j.jaerosci.2014.07.009.

[7] A. Bologa, Paur H.R., and K. Woletz. "Development and Study of an Electrostatic Precipitator for Small Scale Wood Combustion". In: *International Journal of Plasma Environmental Science Technology* 5 (Sept. 2011). URL: https://www.researchgate.net/publication/230558063_Development_and_study_of_an_electrostatic_precipitator_for_small_scale_wood_combustion.

[8] Liam Cassidy. "Advancing Forced Draft Biomass Cookstove Technology with Computational Fluid Dynamics Modeling". In: *Master Thesis* (June 2020), p. 86. URL: https://ir.library.oregonstate.edu/concern/graduate_thesis_or_dissertations/1g05fj85j.

[9] Akan Cigdem. "Surface Mass Transfer in Large Eddy Simulation (LES) of Langmuir Turbulence." In: *Dcotoral Dissertaion* (May 2012), pp. 290–304. URL: https://www.researchgate.net/publication/254706435_Surface_Mass_Transfer_in_Large_Eddy_Simulation_LES_of_Langmuir_Turbulence.

[10] Liao D. et al. "The use of quadraturemethod ofmoments (QMOM) in studying the mechanisms of aerosol agglomeration and its practical use". In: *American Journal of Heat and Mass Transfer* 2 (2015), pp. 42–58. ISSN: 23745398. DOI: 10.7726/ajhmt.2015.1004.

[11] McDuffie E. et al. "Source sector and fuel contributions to ambient PM2.5 and attributable mortality across multiple spatial scales". In: *Nature Communications* 12 (June 2021). URL: https://www.nature.com/articles/s41467-021-23853-y.

[12] Mitchell E.J.S et al. "Pollutant Emissions from Improved Cookstoves of the Type Used in Sub-Saharan Africa". In: *Combustion Science and Technology* 192 (2020), pp. 1582–1602. URL: https://doi.org/10.1177/096032706072520.

[13] Guerrero F. et al. "Particulate matter emissions reduction from residential wood stove using inert porous material inside its combustion chamber." In: *Fuel* 289 (Dec. 2020), pp. 119–796. URL: https://doi.org/10.1016/j.fuel.2020.119756.

[14] Incropera F. P., A. S.. Lavine, and Dewit D. P. "Fundamentals of heat and mass transfer". In: (2011).

[15] Boccardo G., Sethi R., and Marchisio D.L. "Fine and ultrafine particle deposition in packed-bed catalytic reactors." In: *Chemical Engineering Science* 198 (Apr. 2019), pp. 290–304. URL: https://doi.org/10.1016/j.ces.2018.09.024.

[16] Yiquan G. et al. "Chemical agglomeration of fine particles in coal combustion flue gas: Experimental evaluation". In: *Fuel* 203 (May 2017), pp. 557–569. URL: http://dx.doi.org/10.1016/j.fuel.2017.05.008.

[17] Bin H. et al. "Experimental study on particles agglomeration by chemical and turbulent agglomeration before electrostatic precipitators". In: *Powder Technology* 335 (Apr. 208), pp. 186–194. URL: https://doi.org/10.1016/j.powtec.2018.04.016.

[18] Bin H. et al. "Experimental study on particles agglomeration by chemical and turbulent agglomeration before electrostatic precipitators". In: *Powder Technology* 335 (Apr. 2018), pp. 186–194. URL: https://doi.org/10.1016/j.powtec.2018.04.016.

[19] Liu H. et al. "Experimental and numerical investigation on the structure characteristics of vortex generators affecting particle agglomeration". In: *Powder Technology* 36 (2020), pp. 805–816. URL: https://doi.org/10.1016/j.powtec.2019.12.001.

[20] Liu H. et al. "Experimental and numerical investigation on the structure characteristics of vortex generators affecting particle agglomeration". In: *Powder Technology* 362 (2020), pp. 805–816. URL: https://doi.org/10.1016/j.powtec.2019.12.001.

[21] Wiinikka H. and Gebart R. "The influence of fuel type on particle emissions in combustion of biomass pellets". In: *Combustion Science and Technology* 177 (2005), pp. 741–763. URL: https://doi.org/10.1080/00102200590917257.

[22] Winika H. and Gebart. R. "The influence of air distribution rate on particle emissions in fixed bed combustion of biomass." In: *Combustion Science and Technology* 177 (May 2005), pp. 1747–1769. URL: https://doi.org/10.1080/00102200590959468.

[23] V. I. Hanby. "Combustion and pollution control in heating systems". In: (1994). URL: https://link.springer.com/book/10.1007/978-1-4471-2071-1j.

[24] Caubel J. et al. "Optimization of Secondary Air Injection in a Wood Burning Cook stove: An Experimental Study." In: *Environmental Science and Technology* 52 (May 2018), pp. 4449–4456. URL: https://doi.org/10.1021/acs.est.7b05277.

[25] Hautanen J. et al. "Electrical Agglomeration of Aerosol Particles in an Alternating Electric Field". In: *Aerosol Science and Technology* 22 (Apr. 1995), pp. 181–189. URL: https://doi.org/10.1080/02786829408959739.

[26] Li J., Chen Z., and Li Y. "PBM/LES Numerical Simulation of Vortex Structure and Fine Particles Agglomeration in Three-Dimensional Plate Jet". In: *CHEMICAL ENGINEERING TRANSACTIONS* 61 (2017). ISSN: 22839216.

[27] Zheng J. et al. "Investigation of Aggregation Kernel and Simulation of Ultrafine Particle Aggregation under Turbulence and Brownian Motion". In: *Journal of Chemical Engineering of Japan* 51 (May 2018), pp. 62–70. URL: https://ur.booksc.eu/book/70533970/6437e2.

[28] Zheng J. et al. "Modification of the agglomeration kernel and simulation of the flow pattern in acoustic field with fine partic". In: *Powder Technology* 356 (Sept. 2019), pp. 930–940. URL: https://doi.org/10.1016/j.powtec.2019.09.022.

[29] J.Abrahamson. "Collision rates of small particles in a vigorously turbulent fluid". In: *Chemical Engineering Science* 30 (Nov. 1975), pp. 1371–1379. URL: https://doi.org/10.1016/0009-2509(75)85067-6.

[30] Rico J.J. et al. "Particulate matter emissions reduction from residential wood stove using inert porous material inside its combustion chamber." In: *Fuel* 44 (July 2020), pp. 237–283. URL: https://doi.org/10.1016/j.fuel.2020.118496.

[31] Kumar M., Kumar S., and Tyagi S.K. "Design, development and technological advancement in the biomass cookstoves: A review". In: *Renewable and Sustainable Energy Review* 26 (Oct. 2013). URL: http://dx.doi.org/10.1016/j.rser.2013.05.010.

[32] M.AAlvin. "Characterization of ash and char formations in advanced high temperature particulate filtration systems." In: *Fuel Processing Technology* 44 (Sept. 1995), pp. 237–283. URL: https://doi.org/10.1016/0378-3820(95)00016-Z.

[33] M.AAlvin. "Impact of char and ash fines on porous ceramic filter life." In: *Fuel Processing Technology* 56 (July 1998), pp. 143–168. URL: https://doi.org/10.1016/S0378-3820(97)00088-X.

[34] Kshirsagar M.P. and Kalamkar V.R. "A mathematical tool for predicting thermal performance of natural draft biomass cookstoves and identification of a new operational parameter". In: *Energy* 5 (Aug. 2015). URL: http://dx.doi.org/10.1016/j.energy.2015.09.015.

[35] Sippula O. "Fine particle formation and emissions in biomass combustion". In: *Report Series in Aerosol Science* 108 (2010), p. 68.

[36] Uski O. et al. "Acute systemic and lung inflammation in C57Bl/6J mice after intratracheal aspiration of particulate matter from small-scale biomass combustion appliances based on old and modern technologies." In: *Inhalation Toxicology* 24 (2012), pp. 952–965. URL: https://doi.org/10.1080/10590500802494538.

[37] Schwarze P. et al. "Particulate matter properties and health effects: Consistency of epidemiological and toxicological studies". In: *Human and Experimental Toxicology* 25 (2006), pp. 559–579. URL: https://doi.org/10.1177/096032706072520.

[38] Yan P. et al. "Simulation of Particle Agglomeration in Turbulent Flow." In: *Journal of Materials Science and Chemical Engineering* 6 (2018), pp. 39–46. URL: http://www.scirp.org/journal/msce.

[39] Saffman P. G. and Turner J. S. "On the collision of drops in turbulent clouds". In: *Journal of Fluid Mechanics* 1 (May 1956), pp. 16–30. URL: https://doi.org/10.1017/S0022112056000020.

[40] Swamee P. K. and Jain A. K. "Explicit equations for pipe-flow problems". In: *Journal of the hydraulics division* 102 (Feb. 1976). URL: https://www.researchgate.net/publication/280018838_Explicit_eqations_for_pipe-flow_problems.

[41] J. Pra. "Toward the Understanding and Optimization of Chimneys for Buoyantly Driven Biomass Stoves." In: (2013). URL: https://mountainscholar.org/bitstream/handle/10217/80968/Prapas_colostate_0053A_12021.pdf;sequence=1.

[42] Diego Quan Reyes. "A novel biomass reactor addressing the people's need for renewable energy in the developing world". In: *Master Thesis* (Oct. 2020), p. 110.

[43] S. Rigopoulos. In: (June 2012).

[44] S.Rigopoulos. "Population balance modelling of polydispersed particles in reactive flows". In: *Progress in Energy and Combustion Science* 36 (Aug. 2010), pp. 412–443. URL: https://doi.org/10.1016/j.pecs.2009.12.001.

[45] Komarov S.V. et al. "Acoustically Controlled Behavior of Dust Particles in High Temperature Gas Atmosphere". In: 44 (2004), pp. 275–284. URL: https://doi.org/10.2355/isijinternational.44.275.

[46] E. Toolbox. "Air-absolute and kinematic viscosity". In: (). URL: https://www.engineeringtoolbox.com/.

[47] Rapp V. et al. "Reducing Ultrafine Particle Emissions Using Air Injection in Wood-Burning Cookstoves." In: *Environmental Science and Technology* 50 (June 2016), pp. 8368–8374. URL: https://doi.org/10.1021/acs.est.6b01333.

[48] Xu X. et al. "Particle migration and collection in a high-temperature electrostatic Precipitator." In: *Separation and Purification Technology* 143 (Dec. 2012), pp. 184–191. URL: https://doi.org/10.1016/j.seppur.2015.01.016.

[49] Li Y. et al. "A Novel Turbulent Aggregation Device for Flue Gas". In: *Advanced Materials Research* (June 2014), pp. 2425–2429. URL: doi:10.4028/www.scientific.net/AMR.955-959.2425.

[50] Wanga Y. et al. "Enhanced particle precipitation from flue gas containing ultrafine particles through precharging". In: *Process Safety and Environmental Protection* 144 (Apr. 2020), pp. 102–115. URL: https://doi.org/10.1016/j.psep.2020.07.005.

[51] Cengel Y.A., Boles M.A., and Kanoglu M. "Thermodynamics: an engineering approach". In: 5 (June 2004).

[52] Li YW. et al. "Aggregation mechanism of fine fly ash particles in uniform magnetic field". In: *Korean Journal of Chemical Engineering volume* 24 (May 2007), pp. 319–327. URL: https://doi.org/10.1007/s11814-007-5053-9.

[53] Haibo Z., Chuguang Z., and Minghou X. "Multi-Monte Carlo approach for general dynamic equation considering simultaneous particle coagulation and breakage". In: *Powder Technology* 154 (2005), pp. 164–178. URL: https://doi.org/10.1016/j.powtec.2005.04.042.

[54] Haibo Z., Chuguang Z., and Minghou X. "The log-normal size distribution theory of brownian aerosol coagulation for the entire particle size range: part II—analytical solution using Dahneke's coagulation kernel". In: *Journal of Aerosol Science* 30 (Jan. 1999), pp. 17–34. URL: https://doi.org/10.1016/S0021-8502(98)00038-X.

[55] Sun Z. et al. "Agglomeration and removal characteristics of fine particles from coal combustion under different turbulent flow fields". In: *journal of Environmental Sciences* 89 (Oct. 2019), pp. 158–168. URL: https://doi.org/10.1016/j.jes.2019.10.004.

[56] Sun Z. et al. "Effect of turbulent flow field properties on improving the removal of coal-fired fine particles in chemical-turbulent agglomeration". In: *Advanced Powder Technology* 31 (Oct. 2019), pp. 158–168. URL: https://doi.org/10.1016/j.apt.2019.10.007.

[57] Sun Z. et al. "Promoting the removal of fine particles by turbulent agglomeration with the coupling of different scale vortexes." In: *Powder Technology* 367 (2020), pp. 399–410. URL: https://doi.org/10.1016/j.powtec.2020.03.062.

Appendix A

Appendix A

A.1 Experimental results for Turbulent Agglomerator 4

The results from Figure A-1 represent the shift of the Particle Size Distribution (PSD) to lower values due to the influence of turbulent agglomerator 4. Furthermore, in Figure A-2 the removal efficiency of the Electrostatic Precipitator (ESP) coupled with the turbulent agglomerator 4 is shown. Moreover, other curves in both graphs symbolize the results from turbulent agglomerators which can be neglected.

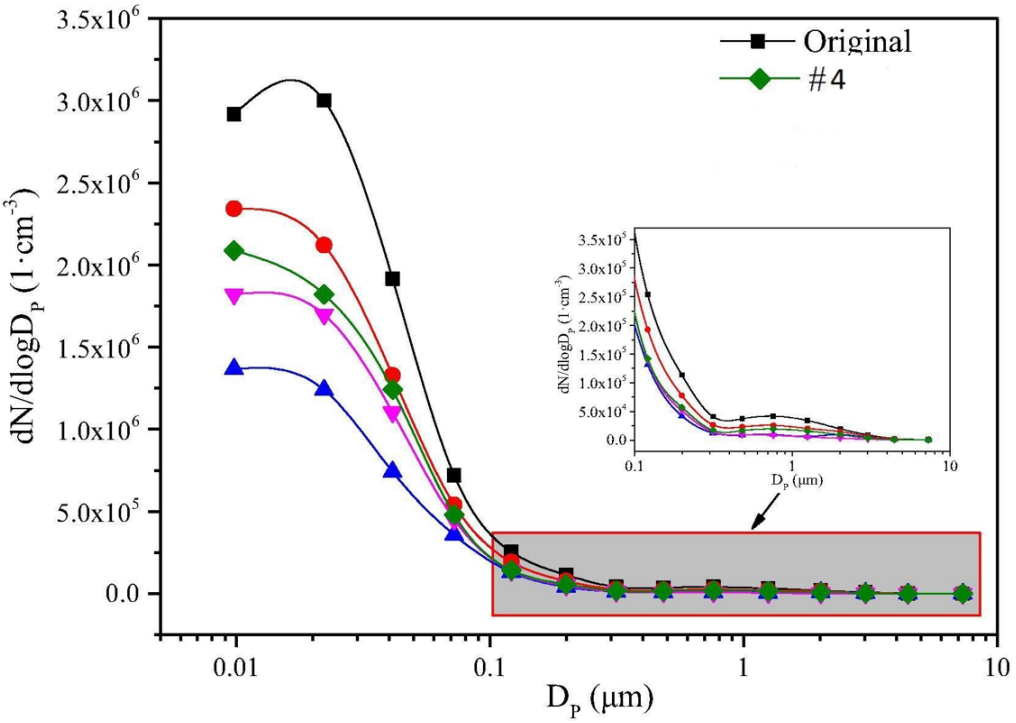

Figure A-1: Particle size distributions after different turbulent agglomerator 4 [56].

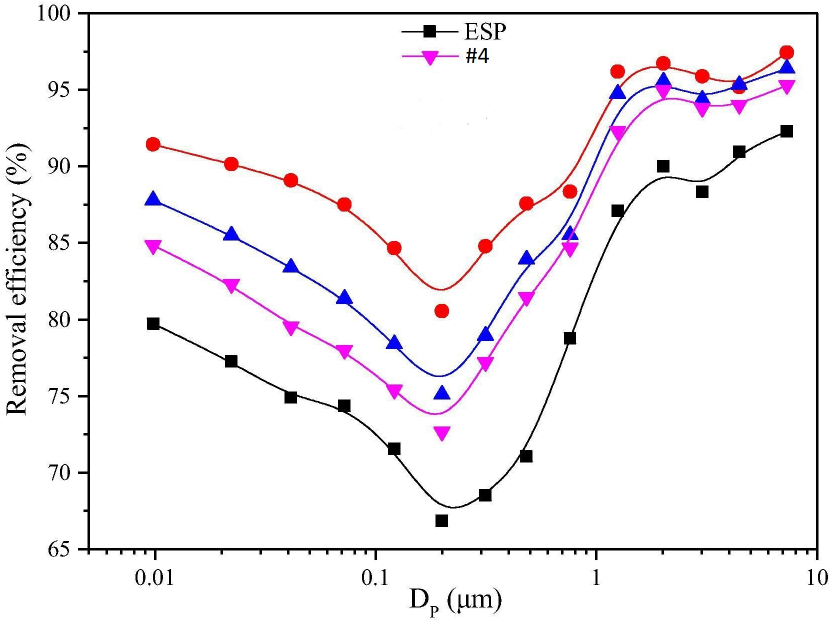

Figure A-2: Removal Efficiency of the ESP after turbulent agglomeration [56].

A.2 Non dimensional numbers

A.2.1 Peclet number

The dimensionless Peclet number (**Pe**) compares convection and diffusive contributions to mass transport. Furthermore, in the case for a flow through a porous base, the following formula applies:

$$P_e = \frac{D_g U}{D} \tag{A-1}$$

Where, D_g is the diamter of graines used for the construction of the porous medium, U is the velocity of the gas-particle flow through the porous media, and D is the molecular diffusivity coefficient.

A.2.2 Gravity number

The dimensionless Gravity number ($\mathbf{N_G}$) represent the theoretical sedimentation efficiency in a flow:

$$N_g = \frac{U_{sed}}{U} \tag{A-2}$$

Where, U_{sed} is the sedimentation velocity, which is equals to:

$$U_{sed} = \frac{\boldsymbol{g} d_p^2 \left(\rho_s - \rho_f\right)}{18\mu} \tag{A-3}$$

Where g is the gravitational acceleration and d_p is the particle diameter and μ is the dynamic viscosity of the flue gas. ρ_s and ρ_f are the densities of the particulate and fluid phase, respectively.

A.3 The overall frictional coefficient of the cookstove

The overall frictional coefficient the the stove and the chimney accounts for the fluid losses within the cookstove, and it is equal to:

$\mathrm{K}_{\text{overall}} = k_{st} + k_{ch} + k_{\text{minor losses}}$

Where the k_{st} and k_{ch} are the major frictional loss coefficients of the stove and chimney, the $k_{minorlosses}$ accounts for the minor losses due to the cookstove geometry. Moreover, the previously mentioned frictional coefficients are equal to:

$$k_{st} = \frac{F_{st} \cdot L_{st}}{Z_{st}} [43] \tag{A-4}$$

$$F_{\text{st}} = \frac{96}{Re_{\text{st}}} [40] \tag{A-5}$$

$$k_{ch} = \frac{F_{ch} \cdot L_{ch}}{Z_{ch}} [43] \tag{A-6}$$

$$F_{\text{ch}} = 0.79 \log \left(Re_{\text{ch}} - 1.64\right)^{-2} [14] \tag{A-7}$$

and

$$k_{\text{minor losses}} = k_{\text{in}} + n_{\text{elbow}} \cdot k_{\text{elbow}} + k_{\text{out}} [41] \tag{A-8}$$

where F_{ch} and F_{st} are the friction factors of the chimney and stove. Additionally, k_{in} and k_{out} are the loss coefficients at the inlet of the stove and the outlet of the chimney, respectively. Furthermore, k_{elbow} is the loss coefficients due to the elbow in the cookstove, while n_{elbow} is the number of elbows.

Glossary

List of Acronyms

CFD	Computational Fluid Dynamics
CMD	Count Median Diameter
DNS	Direct Numerical Simulation
ESP	Electrostatic Precipitator
LES	Large Eddy Simulation
PAH	Polycyclic aromatic hydrocarbons
PAM	Polyacrylamide
PBE	Population Balance Equation
PBM	Population Balance Model
PM	Particulate matter
PSD	Particle Size Distribution
RANS	Reynolds Averaged Navier-Stokes simulations
SA	Sodium alginate